UNIVERSITÀ DI PARMA

UNIVERSITA' DEGLI STUDI DI PARMA

DOTTORATO DI RICERCA IN
" Scienze Mediche e Chirurgiche Traslazionali"

CICLO XXXVII

Orthogonal proteogenomic analysis identifies the druggable PA2G4-MYC axis in 3q26 AML

Coordinatore:
Chiar.mo Prof. Nicola Sverzellati

Tutore:
Chiar.mo Prof. Giovanni Roti

Dottorando: Elisa Simoncini

Anni Accademici 2021/2022 – 2023/2024

Abstract

Despite advancements in next-generation technologies, progresses in treating subtypes of acute myeloid leukemia (AML) driven by aberrantly activated transcription factors (TFs) have been limited. However, the integration of orthogonal omics led to the identification of drugs for "undruggable" TFs. Here, we sought to discover modulators of the *EVI1*/*MECOM* gene, the most lethal oncogenic TF, hyper expressed in AML carrying chromosome 3q26 abnormalities.

To this end, we employed an integrative strategy that combines phenotypic, gene expression-based and proteomic high-throughput approaches to identify modulators of *EVI1*. We screened and scored 5294 compounds enriched for Food and Drug Administration (FDA) approved or bioactive drugs at 1 µM on their ability to suppress the proliferation of 3q26 AML models ($EVI1^{High}$). From $EVI1^{Null}$ transcriptional signatures, we defined an *EVI1* "*On*" and "*Off*" state and used Connectivity Map to identify inducers of an *EVI1* "*Off*" status. Histone deacetylase inhibitors (HDACis) emerged as the top class of compounds able to repress leukemia proliferation by suppressing *EVI1* signature. These molecules induced apoptosis and reduced EVI1 levels in AML cell lines and in primary $EVI1^{High}$ blast cells while the *EVI1* expression sensitizes cells to HDACis. We translated these results in an "N-of-1" clinical trial proposing entinostat in association with azacitidine to patients with relapsed/refractory 3q26 AML based on a compassionate use program for this regimen. Pharmacodynamic modulation of EVI1 was assessed at 6 hours (T6) after entinostat administration in patients and in matched patient-derived leukemia xenograft (PDLX). EVI1 expression decreased in blasts 6 hours after entinostat administration and EVI1 depletion paralleled clinical improvements. This effect was not observed in patients treated with cytarabine. To exclude a contribution of azacitidine in our trial, we completed an *in vivo* efficacy study and we demonstrated a reduction of AML blasts in mice treated with entinostat but not with azacitidine. In addition, longitudinal single-cell RNA sequencing analysis (scRNASeq) of bone marrow AML cells collected before and after azacitidine-entinostat patients' treatment cycle and revealed an inhibitory effect on *Myc* targets genes in the leukemic clone. This effect was also observed in cell lines treated with HADCis suggesting that multiple HDACis regulates the Evi1-Myc axis in

3q26 AML. HDACis-mediated or genetic silencing of *EVI1* led to a direct decrement of MYC.

To dissect the EVI1 co-transcriptional complex and explain the modulation of Myc signaling in EVI1^{High} AML, we performed a rapid immunoprecipitation mass spectrometry of endogenous proteins (RIME) assay. Eleven EVI1 interactors were targets of Myc signaling, including PA2G4, an RNA-binding protein modulated by HDACis. Importantly, *PA2G4* silencing or inhibition (WS6) depleted MYC at protein levels recapitulating the effect of HDACis. Chromatin immunoprecipitation assay (ChIP) showed a reduction of EVI1 and MYC occupancy at *PA2G4* promoter in 3q26 AML cells lines, after WS6 treatment suggesting that these genes are involved in *PA2G4* control in 3q26 leukemia. Consequently, WS6 reduced leukemic growth *in vivo* by suppressing an *EVI1-MYC* signature at single-cell level without inducing toxicities suggesting that PA2G4 is a druggable mediator of EVI1 complex. In contrast, *PA2G4* overexpression rescued EVI1^{High} AML cell lines from the effects of HDACis. These data support the evidence that PA2G4 is a mediator of the Evi1-Myc axis in AML.

In conclusion, we introduce a clinical treatment approach with HDACis to suppress EVI1 in 3q26-AML patients. Additionally, our findings highlight PA2G4 as a potential therapeutic target, urging the development of PA2G4-MYC-EVI1 complex disruptors in this AML subtype.

The information presented in this thesis has been previously published in the article: Marchesini M, Gherli A, **Simoncini E**, et al. Orthogonal proteogenomic analysis identifies the druggable PA2G4-MYC axis in 3q26 AML. Nat Commun. 2024;15(1):4739 [1].

SUMMARY

1. Introduction

1.1. Transcription factors

In 1961, Jacob and Monod postulated the existence of *trans*-acting factors that regulate gene transcription by binding DNA [2]. These *trans*-acting factors were later identified as transcription factors (TFs) [3, 4]. Dysregulated TFs activity is a hallmark of various human diseases including cancer, cardiovascular disease, inflammation, nervous system disorders and others. Due to their pivotal role in these pathologies, TFs are often described as potential targets for new therapy development [5, 6]. In cancer cells, genes encoding TFs are frequently altered with chromosomal rearrangements or point mutations, resulting in either gain or loss of function. Oncogenic signaling pathways can also modify TFs function, driving changes in gene expression that promote cancer cell development [7]. Notably, It has been estimated that 20% of oncogenes in cancer are TFs [8]. Most of TFs consist of distinct domains: a sequence-specific DNA-binding domain and a transcription activation/ repression domain, which interacts with co-repressors or co-activators. By binding to gene promoters or distal enhancers, TFs finely regulate gene transcription [9].

TFs can be classified into three groups: nuclear receptors (NRs), latent cytoplasmic factors (LCTFs) and resident nuclear factors (RNFs).

NR's superfamily consists of 48 members in the human genome [10] that regulate gene expression in response to molecular ligands such as vitamins or hormones. Ligand binding induces conformational changes in NRs, that modulate their interactions with cofactors and subsequently regulate gene transcription [11]. NRs share a similar modular domain structure made of, from N-terminus to C-terminus, the variable modulatory A/B domain, the DNA-binding domain (DBD), the hinge D-region, the ligand-binding domain (LBD), and an F-domain which is absent in some NRs. The DBD and LBD are the most highly conserved domains. The DBD includes two zinc fingers and is approximately 80 amino acids long, while the LBD contains a hydrophobic ligand-binding pocket, which varies among receptors based on their specific ligands [10]. In the past, medicinal chemistry studies were focused on the development of drugs able to interfere with the ligand binding domain or to modify receptor conformation [12]. Drugs that modulate selected NRs have been used in clinical for many years, for example, hormonal therapy with tamoxifen and bicalutamide in breast

and prostate cancers or glucocorticoids in lymphoid malignancies [13]. Several NRs do not have assigned ligand partners and are called "orphan receptors." Many NRs are involved in multiple human diseases, so significant research efforts are dedicated to identifying ligands of “orphan receptors” [14].

RNFs enter the nucleus after synthesis and bind DNA constitutively. The terminal step of the signaling cascade is the RNFs activation by serine/threonine phosphorylation [15]. This class includes hundreds of proteins, that alter transcription by associating with TFs or other co-factors. Several RNFs, as well as c-MYC, are deregulated in human cancer [16]. Unlike NRs, RNFs are often considered “undruggable” targets due to the absence of a binding domain in their conformation or intrinsic enzymatic activities. As a result, targeting the DNA-binding ability of these receptors or disrupting their protein-protein interactions could provide a promising strategy to inhibit their function. In this context, interactions involving intrinsically disordered (ID) proteins are increasingly recognized as viable targets for small molecules. The use of compounds that block disorder-to-order transitions during protein or DNA binding could inactivate specific proteins, including many TFs, providing a comprehensive strategy to target ID proteins [11, 17].

Nevertheless, several RNFs have been successfully targeted by small molecules, such as various direct inhibitors of c-MYC. One of the small molecules is the mimetic peptide IIA6B17, which blocks the formation of the c-MYC/Max heterodimer and c-MYC mediated transcription [18, 19]. An additional example involved small molecules that modulate CREB binding protein (CBP) and C/EBPalpha. These compounds include both transcription inhibitors and molecules that mimic the functions of transcriptional activation domains [11].

LCTFs are located in cytoplasm and translocate into the nucleus upon activation by extracellular signals, through the interaction with cell surface-ligand [15]. These factors can be activated through phosphorylation by serine or tyrosine kinase or through proteolytic regulation in combination with post-translational modifications or secondary messenger signaling combined with phosphorylation events. Once in the nucleus, LCTFs interact with other TFs and regulate gene transcription [11].

An example of LCTFs is *NOTCH1*, a member of the NOTCH receptors family. Activating mutations of *NOTCH1* are found in 50% of T-cell Acute Lymphoblastic Leukemia (T-ALL) [20], and are also reported in other hematopoietic malignancies,

such as chronic lymphocytic leukemia (CLL) [21] and mantle cell lymphoma (MCL) [22]. The active form of NOTCH1 receptor occurs from a series of proteolytic cleavages from a full-length protein that traffics from the endoplasmic reticulum to the surface of the cells, and finally back to the nucleus. The first cleavage is mediated by furin-like protease (S1) and is responsible for NOTCH-receptor maturation from the ER/Golgi to the cell membrane. Upon ligand binding, NOTCH1 triggers a maturation process involving other two-step proteolytic cleavage. The first one is performed by ADAM10 in the NOTCH1 extracellular domain and the second one by the protein complex of γ-secretase within the transmembrane domain. This cleavage generates the intracellular form of NOTCH1, called ICN, that is released in the cytoplasm and migrates into the nucleus to start its genetic regulation [23]. However, this path of protein maturation has been exploited as a therapeutic opportunity to inhibit *NOTCH1* and to interfere with his genetic regulation [23, 24]. For example, it has been demonstrated that γ-secretase inhibitors exhibit an anti-T-ALL activity *in vitro* [20] and *in vivo* [25, 26]. In addition, Roti et al. showed that sarco/endoplasmic reticulum Ca2+-ATPase (SERCA) inhibitors, such as thapsigargin, can induce defects in *NOTCH1* maturation, leading to the accumulation of unprocessed *NOTCH1* in the endoplasmic reticulum/Golgi compartment [24].

Chromosomal alterations that give rise to gene fusion, play an important role in oncogenesis [27]. These events occur with high frequency in specific subtypes of leukemia [more than 50% of acute myeloid leukemia (AML)] [28], as well as in lymphoma and sarcoma and are less common in cancers of epithelial origin. Evidence suggests that gene fusions may arise early in the development of many hematopoietic cancers and sarcomas, potentially acting as an initial trigger in oncogenesis. Oncogenic fusion typically involves genes from two main functional classes: kinases and transcriptional regulators [29]. A well-known example is the t(9;22) translocation, which fuses the tyrosine kinase domain of ABL to Breakpoint Cluster Region (BCR) resulting in BCR-ABL fusion protein. This fusion leads to the overexpression of a constitutively active kinase that drives uncontrolled cellular proliferation. This condition is detected in 95% of patients with chronic myelogenous leukemia (CML) [29].

A further chromosomal aberration involving TFs is the genetic translocation t(15;17) that fuses the promyelocytic leukemia protein (PML) and the retinoic acid receptor α (TF RAR-α) with the generation of the oncogene PML-RAR-α protein. This fusion is

the initiating event of the acute promyelocytic leukemia (APL). In this leukemia subtype, there is a block in granulocytic differentiation and accumulation of abnormal promyelocytes in the bone marrow [29]. A retinoic acid-based treatment has proven highly effective in inducing differentiation of APL blasts, probably due to the degradation of the fusion protein and the inhibition of the leukemic process. Resistance to retinoic acid can be overcome by using histone deacetylase inhibitors (HDACis) [28]. Additional remarkable translocations include t(8;21), t(16;16)/inv(16) and those involving the 11q23 region, which cause respectively the fusion proteins acute myeloid leukemia 1–eight twenty-one (AML1-ETO), core binding factor beta–myosin heavy chain 11 (CBFbeta-MYH9) and mixed lineage leukemia (MLL), impair myeloid differentiation through transcriptional repression. The resulting fusion proteins contain a DNA binding domain while the other often interacts with corepressors complexes [28].

In Burkitt lymphoma, a B-cell neoplasm, chromosomal translocations involve the well-known oncogene *c-MYC*. Here, the *c-MYC* gene is translocated to immunoglobulin loci, leading to overexpression of *c-MYC* and initiation of its oncogenic cell program [28].

Fusion proteins derived by transcription factor translocations (TFTs), such as those in RNFs and LCTs, are considered very difficult to inhibit using targeted therapies [11]. However, because TFs regulate genes essential for tumor growth and metastasis, they are promising therapeutic targets for cancer treatment. Currently, an increasing effort is being made to develop small-molecule drugs that target specific TFs with the possibility of developing new effective therapies with fewer side effects [9].

1.1.1. Targeting the undruggable TFs

TFs have historically been considered undruggable targets [30]. This is because the surfaces of protein-protein interactions are typically flatter and lack the characteristic deep pockets of enzyme active sites [31]. However, it has been recognized that there are a small number of key hotspot residues. These residues, typically clustered together and responsible for the greatest of the interaction energy, make the development of inhibitors targeting protein-protein interactions in TFs feasible.

Moreover, the discovery of allosteric modulation has introduced a promising strategy for influencing these interactions [32, 33].

Several strategies to inhibit TFs are currently under investigation. These include modulating TF expression, targeting nuclear hormone receptor ligand binding domains, targeting protein-protein interactions, modulating proteasomal degradation of TFs, degrading TFs using proteolysis targeting chimera (PROTACs), and disrupting TF-DNA binding with DNA binding compounds [30].

Notably, recent achievements have been obtained in targeting protein-protein interactions, such as the interaction between p53 and MDM2, which leads to the proteasomal degradation of p53. Inhibitors of this interaction are now in clinical trials for solid tumors and hematological malignancies [34].

Another promising approach involves altering the gene expression program to target TFs [30]. For example, inhibitors of the histone H3 lysine 27 (H3K27) methyltransferase enhancer of zeste homologue 2 (EZH2) [35] or inhibitors of Bromodomain (BDs) [36, 37]. BDs are structural models of about 110 amino acids identified in 46 different human proteins, including TFs. One of the first compounds studied for this purpose is the probe (+)-JQ-1, that inhibits BRD4 [38].

Moreover, modern drug discovery processes aimed at targeting undruggable TFs can be divided into two major strategies: a target-based and a phenotypic-based strategy. The first strategy has an increased specificity of target tumor cells with concomitant decreased toxicities toward normal cells. However, there are limitations because target-based screening being mainly cell-free biochemical assays may not recapitulate cellular complexity and the physiology of the disease. Additionally, target-based strategies are less suitable for unknown or intractable targets, such as TF abnormalities or state switches like cellular differentiation. To overcome this challenge, phenotypic-based screening is now under development and is used for imaging-based assay in response to small-molecules perturbation, for cell death assay and gene expression signature as a surrogate of biological state [39]. Phenotypic-based screening can be exploited at three molecular levels: genomic, genetic and proteomic. A genomic approach to phenotypic screening uses gene expression signatures to represent different biological states. This approach is gene expression high throughput sequencing (GE-HTS) [40] that represents a chemical genomic strategy used to define a set of genes distinguishing two different cellular states. Cellular states can be

characterized by gene expression profiles observed after perturbations, such as genetic knocked out. Once the two different states are defined, it becomes possible to identify molecules able to reproduce gene expression shift within the same cellular system and thus to mimic the founder perturbation for example, at gene expression levels. Genetic signatures can be defined by different techniques such as a Luminex-based technology that can include up to 500 different regulated genes, which can be monitored in 384 well plates and detected by ligation-mediated amplification and fluorescent bead-based technology [41]. It is applied for example to screen molecules that induce a shift of cells from the “state A” towards a different “state B” [39]. GE-HTS has been used for identifying small molecules that modulate transcriptional signatures produced by aberrantly activated TFs, a recurrent condition in several human diseases. For example, it has been used for the identification of compounds able to induce differentiation of AML cells [40]. One way to address this issue is to design multiple, integrated cell-based screening and then focus on common emerging hits [24, 39], as performed by Hughes et al. In fact, they generated a “compendium” of expression profiles corresponding to 300 diverse mutations and chemical treatment in *S. cerevisiae*. Through this strategy, they suggested that this compendium could be used to characterize pharmacological perturbations by using gene expression pattern-recognition algorithms [42].

Stegmaier et al. exploited GE-HTS to identify molecules able to induce differentiation in AML cells. The initial step required establishing the gene expression signatures of the biological states of interest through DNA microarrays. For this purpose, they analyzed bone marrow cells from AML patients and normal mature neutrophils/monocytes obtained from healthy donors. Then they selected few marker genes extended through RT-PCR assay. RT-PCR amplicons were then quantified by MALDI-TOF mass spectrometry after a single base extension (SBE) reaction. Next, they screened over than 1700 chemical compounds, in 384 wells format. They carried out RT-PCR and mass spectrometry. The expression levels of the signature genes were quantified to establish a composite differentiation score, which was then used to identify potential hits. Subsequently, the genes regulated by each compound were analyzed and compared to the gene expression differences between the original blasts and the neutrophil/monocyte states. At the end of the process, they selected 8 molecules able to induce myeloid differentiation [40]. Later, they identified Gefinitib as

a drug able to induce myeloid differentiation in AML [43]. Through proteomic and genetic (RNAi-based) strategies, they identify Syk as a therapeutic target [44]. Furthermore, by integrating data from two independent small molecule library screens and a short harping RNA (shRNA) screen for perturbations, they identify glycogen synthase kinase 3a (GSK-3a) as a key associated with the myeloid maturation expression signature in AML cells [45]. The GE-HTS approach was also employed to identify inhibitors of the platelet-derived growth factor (PDGFR) pathway, screening 1,739 compounds and successfully identifying inhibitors of the PDGFR/ERK signaling pathway [46].

Using a similar approach, Roti et al. [24] investigated *NOTCH1* signaling in T-cell acute lymphoblastic leukemia (T-ALL), starting from a gene expression signature of *NOTCH1-on* and *NOTCH1-off* states. They screened 3801 small molecules and identified thapsigargin as the compound able to turn off the *NOTCH1* signature. This finding was integrated with results from a cDNA library screen aimed at identifying factors that enhance the leukemogenic activity of the *NOTCH1* allele. They demonstrated that the regulation of intracellular Ca2+ through the SERCA is a critical vulnerability for *NOTCH1*-mutated T-ALL. Its modulation, with the natural compound thapsigargin, can suppress the maturation process of *NOTCH1* [24].

Applications of GE-HTS exist also for translocations of TFs, that are difficult to treat as biological targets. For example, Corsello et al. generated a genomic expression signature distinguishing AML with the AML1-ETO translocation from cases without the translocation, employing RNAi-mediated knockdown. They demonstrated that inhibitors of dihydrofolate reductase (DHFR) and corticosteroids could induce differentiation and reduce cell viability in AML1-ETO-expressing cells [47].

Among GE-HTS applications, several *in silico* genomic platforms are nowadays available and recognized in the field of drug discovery and oncology research. Connectivity Map (C-Map) is among the more significant. C-Map includes a large public dataset of genomic signatures, of human cancer cells, generated by drugs and genes that describe different biological states. C-Map allows to development of pattern-matching tools to detect similarities among these signatures. This helps researcher to investigate a drug, a gene, or a disease state in a database to discover unexpected connections [48, 49]. It is an *in silico* tool for discovering small molecules and signature-based targets [39]. The C-Map is profiled on Affymetrix (Santa Clara, CA, USA) high

throughput array platform. In its first public release (Build 01), the C-Map profiled 164 bioactive small molecules at a concentration of 10 microM for 6 hours. The 22.000 genes differentially expressed relative to their batch control were collected and ordered by means of Affimetrix GeneChip microarray. The users of C-Map define a “query signature”: a list of genes whose expression is correlated with biological state. Upregulates genes appear near the top of the list (negative connection), downregulate near the bottom (positive connection). The connective score is between -1 and +1 [48]. The second build of the C-Map (Build 02) included the profiling of 1309 discrete small molecules and later a number of genetic perturbations [shRNA and open reading frames (ORFs)] are included [39, 48, 49]. This approach has been successfully applied in real-word cancer research.

An example of this genomic application is related to the study of ALL refractories to Glucocorticoid (GC) treatment. Gene-expression signature of glucocorticoid sensitivity was performed by comparing primary leukemia cells from patients, either sensible or resistant to glucocorticoid. Using C-Map, Wei et al. have discovered an active compound, named Rapamycin, an inhibitor of mTOR, connected with the sensitive versus resistance signature and suggested the hypothesis that this small molecule could induce GC sensitivity in glucocorticoid-resistant ALL cells [50]. They showed that this compound is also a modulator of the antiapoptotic MCL-1 and that Rapamycin sensitized to GC-induced apoptosis by the same pathway. Then, the treatment of this subgroup of ALL with this compound reversed the glucocorticoid resistance signature in lymphoid cells and downregulated antiapoptotic pathways in lymphoid malignancy cells [50].

1.2. Acute Myeloid Leukemia carrying 3q26 chromosomal alterations

Acute myeloid leukemia is characterized by the accumulation of undifferentiated myeloid precursor cells in the bone marrow, blood and other tissues. These leukemic cells are proliferative, clonal, abnormally differentiated and occasionally poorly differentiated. This leads to impaired hematopoiesis and bone marrow failure. While many patients with AML initially respond to induction chemotherapy, refractory disease is frequent, and relapse is the primary cause of treatment failure [51, 52]. Cancer arises

from somatically acquired driver mutations, which contribute to a wide range of biological and clinical complexities in the disease. A classification of cancers based on causality is likely to be clinically relevant. This approach has already been applied to AML, where the focus has shifted from a morphologic-based classification to one driven by genomic changes [52]. AML is an heterogenous, complex and dynamic disease, in which various genes can be mutated, often with multiple driver mutations present within a single case [52]. The classification based on mutational profiling allows us to identify biologically distinct subsets of AML and could be used for developing clinical approaches based on risk stratification of patients [53, 54].

An aggressive subtype of AML is characterized by genetic alterations that involve chromosome 3, such as inv(3)(q21q26), t(3;3)(q21;q26), ins(3;3)(q26;q21q26), t(3;8)(q26;q24) and t(3;21)(q26;q22) [55, 56]. The disease is characterized by the overexpression of the transcription factor Ecotropic viral integration site 1 (*EVI1*), which occurs in approximately 8% of AML patients [57]. Among the genetic alterations, the most frequent are inv(3)(q21q26) and t(3;3)(q21;q26). The breakpoint of the t(3;3) has been mapped 5' of *EVI1*, whereas the breakpoint of inv(3) has been mapped 3' of the gene [58]. A further genetic event is t(3;21)(q26;q22) that results in the *RUNX1/MDS1/EVI1* (*AME*) chimeric gene. AME is a transcription factor fusion protein that transforms Rat1 fibroblasts, upregulates cell cycle and blocks myeloid and granulocyte differentiation [58].

The World Health Organization (WHO) classifies AML with inv(3)(q21q26.2) or t(3;3)(q21;q26.2) as a separate group of AML with poor prognosis [59]. The inv(3) or t(3,3) have also been described in other myeloid malignancies, such as myelodysplastic syndromes (MDS). They account for 1-2% of AML and 1% of MDS cases. More rarely, they have been reported in chronic myelomonocytic leukemia or chronic myeloproliferative neoplasm [60]. Despite different diseases, they have similar molecular and pathological features and poor prognosis [56, 61-63]. The clinical feature is frequently hyperplasia with dysplasia of megakaryocytes [58]. Platelet count is usually normal or high and thrombocytosis can be detected in 7%-22% of cases [60]. It occurs without sex predilection, and patients aged 60 or younger present more frequently 3q26 abnormalities [56]. These patients have a poor prognosis, a highly unfavorable 5-year survival rate, due to resistance to standard chemotherapy, and a short overall survival [56, 61]. The overexpression of *EVI1* is often associated with

other molecular alterations such as monosomy of chromosome 7 and mutations in the RAS pathway, but also deletion of the long term of chromosome 7 or deletion of chromosome 5. In AML, other TFs are mutated, such as *RUNX1* and *IKZF1.* These mutated TFs have been identified in inv(3) and t(3;3) patients [56, 64, 65]. *EVI1* overexpression is also accompanied by *GATA2* haploinsufficiency due to the re-allocation of the *GATA2* distal hematopoietic enhancer (*G2DHE*) [38]. Flow cytometry analysis has shown the expression of CD33, CD34, CD13, CD117 and HLA-DR (noted in >80%of patients) on the cell surface of 3q26 AML blasts and less frequently CD38, CD7 and CD61 [66]. Importantly, overexpression of *EVI1* has also been demonstrated in AML without chromosomal rearrangements at the 3q26 band. For example, high expression of *EVI1* has been observed in a subset of AML patients with translocations involving chromosome band 11q23, which disrupts the *MLL* gene. In this context, overexpression of *EVI1* identifies a critical high-risk group of 11q23 AML patients, that generally present poor prognosis [67, 68].

Moreover, *EVI1* overexpression has been linked to unfavorable prognosis in various solid tumors, including glioblastoma, squamous cell lung cancer, ovarian cancer, prostate cancer and breast cancer. For example, Hou et al. showed that *MECOM* is highly expressed in 41.9% of glioblastoma multiforme, while Xu et al. showed that 32.32% of squamous cell lung cancer exhibited elevated levels of *EVI1* [69, 70]. Additionally, *EVI1* is also redistributed in different types of cancer, such as ovarian tumors in which it shifts from a cytoplasmic distribution in normal oocytes to an increased nuclear localization and a diffuse cytoplasmic presence [71]. Overall, *EVI1* overexpression is consistently associated with poor prognosis and lower survival rates across these solid tumors [72].

1.2.1. Mechanism of *EVI1* overexpression due to enhancer reallocation

The exact mechanism driving *EVI1* hyperexpression was clarified in 2014 by two parallel studies [38, 73]. These studies demonstrated that the chromosomal rearrangements inv(3)(q21;q26) and t(3;3)(q21;q26) lead to the repositioning of the *G2DHE*. This reallocation causes *EVI1* hyperexpression and *GATA2* haploinsufficiency at the same time. It is important to underline that these two events arise from the

repositioning of a single enhancer. This highlights the vulnerability of genomic organization within long-range regulatory interaction domains in case of a chromosomal break [38]. Delwel group used an integrated and functional genomics and genome-engineering approach to define the enhancer that relocates near *EVI1*. In particular, target Next Generation Sequence (NGS) on the long arm of chromosome 3 in 3qs26 AML cell lines identified a 18kb noncoding region between *GATA2* and *RPN1* (in the 3q21 band) that translocate near *EVI1*. Chromatin conformation capture circular sequencing (4C-seq) experiments, identified a region of 9 kb within this 18kb that physically interacts with the *EVI1* promoter. They also defined the essential element in this 18 kb region that shows enhancer activity on *EVI1*. Deletion of this region causes *EVI1* silencing, growth inhibition and maturation block in inv(3) AML cells. Furthermore, they observed that this enhancer is originally a *GATA2* enhancer and its repositioning leads to *GATA2* haploinsufficiency [38]. In the same years, Yamazaki et al. also investigated the mechanistic basis underlying the pathogenesis of this subset of leukemia. They identified *G2DHE*, which is brought into proximity to *EVI1*. They developed a bacteria artificial chromosome (BAC) transgenic clone that recapitulated the inv(3) (q21;q26) allele and they examined the contribution of *G2DHE* to leukemogenesis. They generated transgenic mice harboring 3q21q26 sequences, including *GATA2* distal hematopoietic enhancer or not. The 3q21q26 mice with BAC revealed high white blood cell count, splenomegaly and lower survival compared to mice without *G2DHE*. Thus, these experiments demonstrated that *G2DHE* is essential for *EVI1*-dependent leukemogenesis [73]. Recently, Ottema et al. [74] described the mechanism that causes *EVI1* hyperexpression in 3q26 AML patients harboring t(3;8)(q26;q24). They performed targeted NGS of the long arm of chromosome 3 in AML with t(3;8)(q26;q24) and then used CRISPR-Cas9 technologies to demonstrate that the overexpression of *EVI1* is caused by the hijacked of the *MYC* super-enhancer (*MYC SE*). *MYC SE* harbors approximately 150 kb of open chromatin and is located 1.7 Mb downstream of the *MYC* gene. It plays a crucial role in the transcriptional regulation of *MYC* expression during normal hemopoiesis [75]. They demonstrated that *MYC SE* specifically interacts with the *EVI1* promoter, leading to hyperactivation of the *EVI1* promoter. *MYC SE* is a cluster of multiple enhancer modules that may recruit different sets of TFs. They found that *EVI1* overexpression is triggered by a single enhancer module. This suggests that in AML with this translocation, the aberrant

expression of *EVI1* relies on a single enhancer within the *MYC SE*, which recruits essential hematopoietic TFs and promotes promoter-enhancer looping. In summary, these data uncovered mechanistic similarities among several enhancer-driven EVI1 overexpressing leukemias, indicating that treatments effective for one subtype could potentially be applied across all these AML variants [74].

1.3. Overview of the transcription factor EVI1

1.3.1. *EVI1* gene and protein structure

EVI1 was identified in 1988 by Mucenski and colleagues as a frequent retroviral insertion site in murine myeloid leukemias [76]. *EVI1* is located on the long arm of chromosome 3 at q26.2 (3q26.2) [77] and it is encoded from the *MDS1* and *EVI1* complex locus (*MECOM)* that results in multiple transcripts [78]. *MECOM* locus is approximately 580kb large and harbors two different transcription start sites (TSS): the downstream *EVI1* and the upstream *MDS1* [79]. *MDS1* is encoded by 4 exons in a region of 500 kb upstream *EVI1*. *MDS1/EVI1* results from alternative splicing of the third exon of *MDS1* and the second of *EVI1*. *EVI1* gene is 65 kb and is made of 16 exons, 14 exon coding, and it generates different splicing isoforms: *EVI1A*, *EVI1B*, *EVI1C*, *EVI1D*; *EVI13L* [79]. The protein isoforms generated by *MECOM* are i) MDS/EVI1, ii) EVI1, iii) EVI1 Δ324; iv) EVI1 Δ9AA. EVI1 is a 145 kDa protein with 1051 amino acids and binds DNA through its two zinc finger (ZF) domains (ZF1 and ZF2). EVI1 contains 7 ZF at the N-terminal ZN domain (ZF1), a central proline-rich repression domain and 3 ZF at the C-terminal ZF domain (ZF2). At C-terminal domain contains also an acidic domain [79, 80]. The proximal zinc finger recognizes a consensus sequence of 15 nucleotides, GA(C/T)AAGA(T/C)AAGATAA [81], while the distal set of zinc finger binds to the consensus sequence GAAGATGAG [82]. EVI1 Δ324, 103 kDa, lacks 324 amino acid sequence from EVI1, including the sixth and seventh zinc finger of the ZF2 domain [83]. EVI1 Δ9AA lacks 9 amino acids from the full-length isoform in the repressor domain; however, this deletion does not interfere with DNA binding [84]. MDS1-EVI1 protein, also called PRDM3, contains a positive regulatory region (PR) that lacks in EVI1 because it is encoded by the *MDS1* part [78]. This PR domain contains a Su(var)3-9 and an 'Enhancer of zeste' (SET) domain, important for its methyltransferase activity [85, 86].

1.3.2. EVI1 biological functions

Evi1 is expressed in embryonic and adult mouse tissues such as the lung, heart, urinary system and Mullerian ducts. It is detectable also in red blood cells, developing limbs and developing oocytes in the ovary [87]. To investigate the biological function of *Evi1,* Hoyt et al. disrupted *Evi1* transcript with target mutagenesis and saw that homozygous mutant mice died at approximately embryonic day 10.5 due to massive hemorrhaging and heart failure. Additionally, these mice exhibited defects in heart and central nervous system development [88]. Adult mice express *Evi1* at variable levels in different tissues, then, *Evi1* plays an important role in mouse tissue development [72]. This pattern of expression in mice tissue agrees also with human adult tissue. Indeed, *EVI1* was not found in human skeletal muscle and bone marrow, but it is expressed at low levels in the small intestine, colon, thymus, spleen, heart, brain, testis, and placenta, and at moderate to high levels in the lung, kidney, uterus, prostate, and stomach [89, 90]. *EVI1* is crucial for the differentiation of hemopoietic stem cells (HSC) [91], by influencing the expression of *GATA2*. It has been reported [92] that the HSC of mice with *Evi1*-deletion exhibit impaired proliferation and repopulation abilities, along with decreasing level of *GATA2*, which is essential for the proliferation and differentiation of these cells. Restoring *Evi1* expression can rescue the ability of proliferation and differentiation of these cells by upregulating *GATA2* expression. This highlights that *EVI1* has a key role in the above-mentioned processes [93].

Moreover, *EVI1* affects erythropoiesis, granulopoiesis and megakaryocytopoiesis [93]. One of the EVI1 interactors is GATA1, an erythroid transcriptional regulatory factor. This interaction blocks the recognition or binding of GATA1 to DNA and induces failure in erythroid differentiation [94, 95]. Furthermore, EVI1 blocks the granulocytic differentiation of the 32Dcl.3 cells in response to granulocyte colony-stimulating factor (G-CSF) [96], by interaction with RUNX1 [97].

Additionally, the interaction between EVI1 and PU.1 blocks the association of PU.1 with coactivating partners, such as c-Jun, rather than by displacing PU.1 from the DNA. This results in impaired myeloid differentiation [98]. The interactions help to explain how EVI1 preserves an immature phenotype with self-renewal capacity [99]. In contrast, EVI1 accelerates growth rates and induces differentiation along megakaryocytes [93].

EVI1 is a TF, localized in the nucleus, that interacts with several coactivators, corepressors and epigenetic regulators such as C terminal binding protein (CtBP), HDAC, with p300/CBP associated factor (CAF), DNA methyl transferase [99, 100]. In particular, EVI1 interferes with the TGF-β signaling pathway through the repression of Smad3 and the recruitment of C terminal binding protein (CtBP) corepressor. *Evi1* represses TGF-β signaling, that acts as a negative regulator of the cell cycle in many cell types [101]. Thus, EVI1 plays a role in regulating cell cycle progression.

Furthermore, EVI1 is a transcriptional regulator. It upregulates the expression of several genes involved in HSC proliferation, including *GATA2*, *ANGPT1*, *MPL*, *JAG2*, *PBX1*, *SETBP1* and *PI3K-AKT-mTOR* signaling [91, 92, 102, 103]. *EVI1* downregulates the *PTEN* tumor suppressor gene [104] and *Cyclin genes* and upregulates inhibitory *CdKns* suggesting its role in leukemogenesis and progression of the cell cycle. In particular, it downregulates *cyclin-dependent kinase inhibitor p57* which is essential for quiescence of HSC [104-106]. EVI1 has a role also in apoptosis [89] by interacting with and inhibiting c-Jun N-terminal kinase (JNK), thereby protecting cells from cell stress-induced death [107]. Additionally, EVI1 inhibits apoptosis by binding to and activating the BCL-XL promoter in the colon carcinoma that overexpresses *EVI1* [108]. Furthermore, it has been shown that EVI1 downregulates the transcription of *P2RX7* in AML. *P2RX7* is an ATP-receptor on the cell surface that mediates apoptosis ATP-dependent in macrophages and neutrophils [72, 102].

Moreover, EVI1 acts as a regulator of its own transcription. EVI1 interacts functionally with its promoter; different EVI1 isoforms regulate its transcription through distinct promoter regions. In particular, EVI1 145 kDa acts as an activator of *EVI1* transcription, instead EVI1 Δ324 and MDS1/EVI1 act as repressors [109]. *EVI1* transcription is also regulated by RUNX and ELK1, two essential proteins involved in hematopoiesis. Maicas et al. have shown that one of the mechanisms by which RUNX1 exerts its role in megakaryocytic differentiation is through *EVI1* regulation [109].

1.3.3. Possible therapeutic strategy against *EVI1*-overexpressing malignancies

Three potential approaches to treat *EVI1*-overexpressing cancer include (i) prevent or revert the aberrant *EVI1* overexpression at the transcriptional level; (ii) prevent the association of the EVI1 protein with its protein interaction partners; (iii) modulate downstream effects of EVI1 [110].

A promising therapeutic strategy aims to inhibit the super-enhancers that aberrantly activate the *EVI1* promoter. One proposed target for this strategy is BRD4, a member of the bromodomain and extra-terminal (BET) subfamily of human bromodomain proteins. BRD4 plays a key role in transcription activation, by maintaining the activity of super-enhancers, such as those of *MYC*, *CDK4/6* and *BCL2/Bcl-xl* [111, 112]. BET inhibitors inhibit *GATA2* super-enhancer, thereby repressing *EVI1* and reversing *EVI1*-dependent transcriptional programs by enhancers and super-enhancers inactivation of key oncogenes. Delwel et al. demonstrated that the BRD4 inhibitor, JQ-1, strongly inhibits proliferation and induces apoptosis of AML overexpressing *EVI1*. JQ-1 interferes with DNA regions and super-enhancer. Several BET inhibitors are currently undergoing clinical evaluation [38, 111, 113].

In this context, the use of CBP/p300 inhibitors is significant, as they block the acetylation of various transcriptional regulators, including *EVI1*, the *GATA2* enhancer, and RUNX1, which interacts with EVI1 [113]. The GATA2 enhancer is altered by breakpoints that cause its repositioning, leading to increased production of enhancer RNAs (eRNAs). These eRNAs are critical regulators of gene expression. The CBP/p300 inhibitor GNE-049 has been shown to block the production of these eRNAs, suggesting a potential therapeutic strategy [114]. It can be assumed that a targeted combination therapy using this histone acetyltransferase inhibitor could simultaneously deacetylate key TFs, thus reducing their activity, and impair super-enhancers, which would effectively silence *EVI1*'s transcriptional program [113].

Other studies have examined the interactions of key myeloid TFs, such as CEBPA and RUNX1, with the *GATA2* distal hematopoietic enhancer. PARP1 and IKZF1 proteins colocalize at this site, highlighting potential therapeutic targets for disrupting the oncogenic super-enhancer. Inhibiting PARP1 pharmacologically, using olaparib or talazoparib, or via shRNA, diminish the interaction between the super-enhancer and

the *EVI1* promoter, resulting in reduced *EVI1* expression and promoting differentiation and apoptosis in 3q26 AML cell lines [115].

The second potential strategy is preventing the interaction of EVI1 and its interactors. EVI1 interacts with different proteins that affect target gene expression, including histone methyltransferases (HMTs) and HDACs. HDACis, such as trichostatin A, have been proven *in vitro* to revert *EVI1*-mediated transcriptional repression of *TGFβ* signaling [101]. Therefore, selective inhibition of the enzymatic activity of EVI1-associated coregulators may represent a good targeted strategy for the treatment of *EVI1*-overexpressing malignancies [110].

The third approach consists in modulating downstream effectors of EVI1.

A proposed target is anti-apoptotic proteins. EVI1 binds the promoter of the anti-apoptotic Bcl-xL and upregulates its transcriptional activity [108]. This suggests the use of BH3-mimetic inhibitor targeting Bcl-xL alone or in combinations against *EVI1*-expressing disease [113]. Moreover, Saha et al., demonstrated that the small compound pyrrole-imidazole polyamide, which inhibits the EVI1-binding site in the *GRP56* promoter, inhibits *GPR56* expression and suppresses cell growth with concomitant induction of *p53*-dependent apoptosis [116]. GRP56 was previously demonstrated to exhibit an essential role in *EVI1*-mediated resistance to apoptosis [117]. A target that is still under investigation is the use of all-trans-retinoic acids (ATRA) in AML overexpressing *EVI1*. The translocation t(3;21)(q26;q11) causes the *EVI1* gene to be regulated by elements of the retinoic acid-responsive gene *NRIP1* [118]. In EVI1^{High} AML, *NRIP1* is upregulated, probably due to EVI1 binding to an *NRIP1* enhancer. Knockdown of *NRIP1* reduced the proliferation and viability of EVI1^{High} AML cells and increased their sensitivity to ATRA. So, NRIP1 is recognized as a potential therapeutic target in *EVI1*-overexpressing malignancies [118].

Additional strategies that require further investigation are the inhibition of mitochondrial creatine kinase (CKMT1) and Erythroblast transformation-specific (ETS)-related gene (ERG). EVI1 inhibits RUNX1, leading to increased CKMT1 levels, a metabolic vulnerability in AML cells with *EVI1* overexpression (EVI1^{High} AML). shRNA-mediated knockout of *CKMT1*, or inhibition with cyclocreatine, decreases EVI1^{High} AML cell growth, causing cell cycle arrest and apoptosis. Cyclocreatine treatment disrupts mitochondrial respiration and ATP production, affecting WNT and GSK3 signaling, that has an important role in normal HSCs [119, 120].

Moreover, EVI1^{High} AML are therapeutically vulnerable to the inhibition of the ERG pathway. ERG knockdown in these cells reduces proliferation, increases apoptosis, and promotes differentiation [121, 122]. So, developing effective pharmacological inhibitors for ERG may provide a possible approach.

Despite these approaches are promising, efforts to optimize EVI1 suppression for clinical translation are still underway.

In this study, we aim to identify regulators of the *EVI1/MECOM* gene, which is the most lethal oncogenic TF and is highly expressed in AML with chromosome 3q26 abnormalities. To this end, we employed *in silico* small molecule phenotypic and genomic screening approaches and proteomic analysis of the EVI1 chromatin complex in 3q26 leukemia preclinical models and patients.

2. Methods

2.1. Cell lines

The human cell lines MOLM1 (#ACC 720), UCSD/AML1 (#ACC 691), HNT34 (#ACC 600), TF1 (#ACC 334), MUTZ-3 (#ACC 295), 293T (#ACC 635), OCI/AML3 (#ACC 582), MOLM13 (#ACC 554), NOMO1 (#ACC 542), OCI/AML2 (#ACC 99), GDM1 (#ACC 87), HL-60 (#ACC 3), SKM1 (#ACC 547) and 5637 (#ACC 35) were purchased from the Leibniz-Institut DSMZ-German collection of microorganisms and cell cultures (Germany). IMS-M2 were previously reported in [123]. U937T and U937T_E10 were a kind gift from the Rotraud Wieser laboratory (University of Vienna, Clinic of Medicine I, Waehringer Guertel 18-20, 1090 Vienna, Austria). Cells were cultured in RPMI 1640 (Thermo Fisher Scientific, Waltham, MA, USA, #31870074) with 10% or 20% fetal bovine serum (FBS) (Thermo Fisher Scientific, #10270106) and 1% penicillin-streptomycin (EuroClone, Pero-Milan, Italy, #ECB3001D). UCSD/AML1 medium was supplemented with 10 ng/mL rhGM-CSF (ProteinTech Group, Rosemont, IL, USA, #HZ-1002). MUTZ-3 cells were maintained in DMEM (Thermo Fisher Scientific, #11965118) with 20% FBS, 20% 5637 conditioned medium, and 2 mmol/L L-glutamine (Thermo Fisher Scientific, #25030-024). The tetracycline-repressible U937T and U937T_E10 were cultured in RPMI 1640 containing 10% tetracycline-free FBS (Takara Bio Europe SAS, Saint-Germain-en-Laye, France, #631367). 293T cells were cultured in DMEM, 10% FBS, and 1% penicillin-streptomycin. Cell lines were grown in a humidified incubator at 37 °C and 5% CO_2, routinely identified by short tandem repeat profiling, and monitored for mycoplasma contamination.

2.2. Clinical AML samples and patients

Leukemia cells derived from the peripheral blood and bone marrow of patients with 3q26 AML were obtained under approved protocols at the Department of Medicine and Surgery at Parma University Hospital (n. 18249/18/05/2017, and n. 29785/13/07/2021), according to the Declaration of Helsinki guidelines for the protection of human rights. Mononuclear cells were isolated by density gradient centrifugation using an LSM-lymphocyte separation medium (Cappel™ MP Biomedicals, Solon, OH, USA, #50494). We collected a total of 39 samples (Male=18;

Female=21; mean age=64.4 -25-87-). Bone marrow biopsies were collected according to the protocol n. 265/2019, granted by the same Institution. All biological samples were collected after the release of a written informed consent. Three patients (PR#001, PR#002, and PR#003) were enrolled in a compassionate use program (the treatment schedule was described in the NCT00101179 clinical trial), they have provided written consent, and they did not receive compensation. Individuals agreed to participate in our study and having their data reported for scientific purposes. No sex and/or gender was considered in the design of this study.

2.3. Karyotype analysis and fluorescence in situ hybridization

Primary leukemic blasts were isolated as described in the previous section and cultured for 48 hr in RPMI 1640 in a humidified incubator at 37 °C and 5% CO_2. Cell media was supplemented with 0.1 µg/mL of colcemid (Thermo Fisher Scientific, #15212012) for 2 hr, followed by incubation in a hypotonic solution (0.075M KCl). Cells were fixed in a 3:1 methanol (Sigma-Aldrich, St. Louis, MO, USA, #322415) and acetic acid glacial fixative solution (Sigma-Aldrich, #A6283) and spread on top of Superfrost Plus microscope slides (Thermo Fisher Scientific, #10149870). For the karyotype analysis, chromosome banding was performed by quinacrine (Q-banding) or Giemsa (G-banding) staining. A minimum of 20 metaphases per sample were acquired using a Nikon Eclipse 80i microscope (Nikon Instruments, Inc., Melville, NY, USA) and analyzed using NIS element software (Nikon Instruments, Inc.). For the fluorescence in situ hybridization (FISH) analysis, 10 µL of *MECOM*/*RUNX1* t(3;21) fusion (Kreatech Biotechnology B.V., Amsterdam, The Netherlands, # KBI-10310) or *MECOM* t(3;3); inv(3)(3q26) break-apart translocation probes (Kreatech Biotechnology B.V., # KBI-10204) were incubated at 37 °C for 12-16 hr after a phase of DNA dehydration with ethanol-scale incubation (75%-85%-100%) and DNA denaturation [75±1 °C 5 minutes (min)]. Slides were washed once with 0.4x saline sodium-citrate/0.3% NP40 buffer at 73±1 °C, followed by 4 x SSC/0,1% NP-40 at ambient temperature. DNA was counterstained with 4′,6-diamidino-2-phenylindole (DAPI, Sigma-Aldrich, #10236276001) before microscope analysis (Eclipse 80i microscope, Nikon Instruments, Inc.). Two-hundred interphase nuclei and at least 6 metaphases were

analyzed for each patient and DNA rearrangements were defined starting from a 5% cutoff for each probe.

2.4. Small molecule screening assay

We screened 5349 compounds in duplicates, including i) the Spectrum Collection library (MicroSource Discovery System, Inc., Gaylordsville, CT, USA) containing 1200 FDA/EMA-approved drugs, 500 natural products, and 300 molecules in preclinical stages for a total of 2000 compounds; ii) the anti-cancer compound library (Selleck Chemicals, Houston, TX, USA), containing 349 bioactive compounds with known anti-cancer activity; and iii) the NDL-3000 library (TimTec, Tampa, FL, USA) containing 3000 natural derivative compounds. MOLM1 and UCSD/AML1 cells (1.5×10^3 per well) were plated in 384-well tissue culture plates in 45 µL of medium using the BioTeck EL460 automated cell dispenser (BioTeck) and incubated for 72 hr. Small molecules were screened at the final concentration of 1 µM dissolved in (dimethyl sulfoxide) DMSO added by a Tecan Evo200 (Tecan, Switzerland). DMSO and etoposide (5 µM) treated cells were used as negative (vehicle) and positive controls, respectively.

The effect on cellular viability was quantified using an ATP-based Cell Titer-Glo assay (Promega Corporation, Madison, WI, USA, #G7573), and presented as a percentage of viable cells over control (POC). We also defined the normalized percentage of cell death (∆POC) on the basis of the average of duplicates (POC_molecules) using the following formula: [negative controls luminescence (DMSO) – sample luminescence]/[negative controls luminescence (DMSO)] x 100. POC_molecule values for each compound have been compared to the DMSO control values (n = 24) using an ANOVA test applied to a linear regression model. The resulting p-values were adjusted for the multiple comparisons using the Benjamini & Hochberg (BH or FDR) method included in the p.adjust function implemented in the stats R package. We prioritized hits on the basis of the 95th percentile limit of the highest statistically significant ∆POC [Benjamini-Hochberg $P \leq 0.05$]. We then calculated all pairwise distances between the given fingerprints of the top candidates and fit a beta distribution to the resulting Tanimoto scores, conditioned on the number of set bits in each fingerprint (ChemmineR package). The resulting matrix was clustered using the hclust

function in the stats package with Euclidean distance and the average agglomeration method.

Forty compounds were counter-screened in additional cell lines (HNT34, NOMO1, and THP1) in a six-log [concentrations] dilution ranging from 10 µM to 30 nM. The tertiary screen in TF1 assayed 4942 small molecules from the annotated libraries derived from the Selleck and Sigma-Aldrich collection available at the screening unit of the Leibniz-Forschungsinstitut of Molecular Pharmacology (FMP). BRAID analysis of combined drug action was calculated according to [124].

2.5. High-throughput *in silico* screening

Marker genes for the *EVI1 "On"* vs. "*Off"* signature were chosen using publicly available Affymetrix microarray expression profiling data on TF1 cells transduced with shRNAs targeting *EVI1* (E-GEOD 16238) or from mRNA quantification in AML cell lines harboring 3q26 aberration (E-MTAB-2225) [38]. For the TF1 study, we then inferred marker genes to the CMap [48, 125] database (https://clue.io/lincs), while for the cross-validation set in *EVI1* repressed HNT34 or AML^{High} vs. AML^{Low} with the The Library of Integrated Network-Based Cellular Signatures (LINCS) [126]. We used the parametric bootstrap method on sets of molecules to calculate the enrichment of compound classes [127]. CMap and LINCS/L1000FWD are accessible at https://clue.io/lincs and https://lincsproject.org, respectively.

2.6. Cell treatment and viability assay

AR-42 (#S2244), belinostat (PXD101, #S1085), entinostat (MS-275, #S1053), cytarabine (ara-C, #S1648), vincristine sulfate (#S1241), daunorubicin HCl (#S3035), methotrexate (#S1220), WS6 (#S7442), (+)-JQ-1 (#S7110) and MG132 (#S2619) were obtained from Selleck Chemicals. Cell solution (50 µL/well of 0.02 x 10^6/mL) was dispensed in 384-well plates (Corning Life Sciences Plastic, Bedford, MA, USA, #3570) using Multidrop™ Combi (Thermo Fisher Scientific, #5840300). According to the manufacturer's protocol, small molecules were dissolved in DMSO or ddH_2O and added with a nanometric Tecan D300e dispenser (Tecan Trading AG, Switzerland) at the concentration indicated in the figures. Cell viability was assessed after 72 hr of drug

treatment using a CellTiter-Glo ATP assay (Promega Corporation, #G7573). Values for IC_{50} and the area under the curve (AUC) were calculated using GraphPad Prism 8 software (La Jolla, CA, USA).

2.7. Apoptosis and DNA content assays

Apoptosis was measured by annexin V (annexin V, FITC conjugate, Thermo Fisher Scientific, #A13199) and propidium iodide (Thermo Fisher Scientific, #BMS500PI) staining. Cells were analyzed by flow cytometry with a FACScan (Beckman Coulter-Cytomics FC 500, Brea, CA, USA) or Attune NxT (Thermo Fisher Scientific) flow cytometry, and data were processed by FlowJo V10 (Tree Star, LLC, Ashland, OR, USA) analytical software. Cellular DNA content was assessed by staining with propidium iodide (50 µg/mL). At least 20,000 events were acquired, and all of the determinations were replicated at least twice.

2.8. Methylcellulose assay

Clonogenic assays were performed using the MethoCult™ colony-formation assay (STEMCELL Technologies, Vancouver, BC, Canada, #GFH84444). In brief, a 10x concentrated AML cell suspension was prepared and mixed with thawed MethoCult™ in a 1:10 v/v ratio of cells: MethoCult™. Samples were vortexed thoroughly and left to stand for at least 5 min to allow bubbles to rise to the top before dispensing; they were then incubated at 37 °C, in 5% CO_2, with 95% humidity for 15-20 days. Colony identification and counting were performed using an EVOS FL inverted microscope (Thermo Fisher Scientific) equipped with 4x and 10x objectives.

2.9. Immunodetection and antibodies

Whole protein lysate was extracted using 1x cell lysis buffer (Cell Signaling Technology, Danvers, MA, USA, #9803S) supplemented with phospho-stop phosphatase inhibitor (Sigma-Aldrich, #04906837001) or protease/phosphatase inhibitor cocktail 100x (Cell Signaling Technology, Danvers MA, USA, #58725) and Complete Mini, EDTA-free protease inhibitor (Sigma-Aldrich, #11836170001). Cells were lysed on ice for 10 min

with gentle stirring and centrifuged at 21,130x *g* for 10 min at 4 °C. Protein assay dye reagent (Biorad Laboratories, Hercules, CA, USA, #5000006) was used for protein quantification and 40 µg of total lysate/sample was loaded for SDS-PAGE analysis. The following specific antibodies were purchased from Cell Signaling Technology: anti-EVI1 (C50E12, #2593), β-actin (8H10D10, #3700), cleaved caspase 3 (Asp175, #9661), and MYC (#9402). Anti-PA2G4 antibodies were purchased from Sigma-Aldrich (#HPA016484, #SAB1402863), Abcam (Cambridge, United Kingdom, #ab180602) and Proteintech (Rosemont, IL, USA #66055-1-Ig, #15348-1-Ap). Anti-histone H3 (acetyl K27) was purchased from Abcam (#ab4729). Anti-acetylated α-Tubulin (#sc-23950) and HSP90 (#sc-69703) were purchased from Santa Cruz Biotechnology (Dallas, TX, USA). All primary antibodies were used at a dilution factor of 1:1000. IRDye 680LT goat anti-mouse IgG (#925-68020), IRDye 800CW goat anti-rabbit IgG (#925-32211), and IRDye 680RD goat anti-rabbit IgG (#925-68071) from LI-COR Biotechnology (Lincoln, NE, USA) were used as secondary species–specific antibodies at a dilution factor of 1:10000. Signals were detected using the LI-COR Odyssey imaging system (LI-COR Biotechnology).

2.10. RNA processing and quantification

RNA was extracted using the RNeasy mini kit (Qiagen, Hilden, Germany, #74106). According to the manufacturer's protocol, cDNA was synthesized using the high-capacity cDNA reverse transcription kit (Thermo Fisher Scientific, #4368814), using 1 µg of RNA as starting material. A quantitative real-time polymerase chain reaction (qPCR) was performed using TaqMan gene expression assays for *MECOM* (Thermo Fisher Scientific, #Hs00602795_m1), *MYC* (Thermo Fisher Scientific, #Hs00153408_m), *PA2G4* (Thermo Fisher Scientific, #Hs00854538_g1), and TaqMan™ Universal PCR master mix (Thermo Fisher Scientific, #4364338) in an Applied Biosystems™ StepOne™ real-time PCR system (Thermo Fisher Scientific, #4376357). Each condition was run in triplicate. The expression levels of the target genes were normalized to those of *RPL13A* or *ACTB* (Thermo Fisher Scientific, #Hs04194366_g1, #Hs99999903_m1). Data were analyzed using the ΔΔ cycle threshold (CT) method and plotted as a percentage relative to control.

2.11. Immunofluorescence

Cells (50 x 10^3) were washed in PBS and spotted on Superfrost Plus microscope slides (Thermo Fisher Scientific, #10149870) using a cytospin centrifuge (CR2000 Small Prime Centrifuge, Centurion). Fixation was carried out for 10 min in PBS, 4% paraformaldehyde (Thermo Fisher Scientific, #28908) at 4 °C. For nuclear protein staining, cells were permeabilized for 10 min in PBS and 0.4% Triton X-100 (Sigma-Aldrich, #T-9284) at ambient temperature. We applied a blocking solution for 1 hr at ambient temperature composed of 5% bovine serum albumin, 0.1% Triton X-100, and 1% goat serum (Abcam, #ab138478) diluted in PBS. Cells were then incubated for 1 hr at ambient temperature with the antibody targeting EVI1 (Cell Signaling Technology, #2593, 1:1000 dilution) or PA2G4 (Sigma-Aldrich, #HPA016484, #SAB1402863 both diluted 1:1000) and subsequently revealed by secondary antibodies (Invitrogen, Carlsbad, CA, USA, #A11029, #A11036, both diluted 1:400) and diluted in blocking solution. Nuclei were stained with DAPI (Sigma-Aldrich, #D9542). Prolong Gold Antifade reagent (Thermo Fisher Scientific, #P36934) was used as a mounting solution. Images were captured using an EVOS™ M5000 microscope (Thermo Fisher Scientific) or a Leica Stellaris 5 confocal microscope. ImageJ (http://rsbweb.nih.gov/ij/) and Leica Image Compass were used for the analysis.

2.12. Immunohistochemistry

Informed consent was obtained from patients undergoing trephine bone marrow biopsy from the iliac crest for diagnostic procedures according to the ethical guidelines and the protocol 265/2019/TESS/UNIPR, approved by the University of Parma. Following decalcification, 4-µm-thick sections obtained from formalin-fixed, paraffin-embedded bone marrow biopsies were processed for immunohistochemical staining. Bone marrow samples were deparaffinized and rehydrated in decreasing alcohol scale; enzymatic epitope retrieval was performed by water bath at 95°C, 40 min, in ULTRA Cell Conditioning Solution (Ventana; 950-224); endogenous peroxidase was blocked with 3% H_2O_2. After incubation with rabbit anti–EVI1 (Cell Signaling Technology, #2593; 1:400 dilution; overnight; 4°C), rabbit anti-MYC (Cell Marque™; 395R-18; ready to use; 40 min; 37°C), or mouse anti-Ki67 (Agilent, Santa Clara, CA, USA, #IR626; ready to use; 30 min; 37°C) antibodies, all sections were revealed by IHC Detection Kit-

Micropolymer (Abcam #ab236466) according to manufacturer's recommendations. The nuclei were counterstained by light hematoxylin. All staining steps were performed at ambient temperature. 3D type I collagen scaffolds and xenografted tumors were fixed in formalin, included in paraffin and processed as indicated above. Images were acquired with a MoticEasyScan One (Motic, Hong Kong) microscope and quantified using QuPath software v.0.3.2 (https://qupath.github.io/) [128].

2.13. Chromatin immunoprecipitation and ChIP Sequencing

Chromatin was collected from HNT34 cells (20 x 10^6 cells each condition) using ActiveMotif ChIP-IT® Express (ActiveMotif, Carlsbad, CA, USA, #53008) according to the manufacturer's instructions and sheared in 12 sets of 10-second sonication using a Branson Digital Sonifier (Thermo Fisher Scientific). Chromatin was incubated overnight at 4 °C with 10 µg of the following antibodies: EVI1 (Cell Signaling Technology, #2593S), MYC (Cell Signaling Technology, #9402S), histone 3 at lysine 27 (H3K27Ac, Abcam, #ab4729), and rabbit IgG (Merck, #12-370). DNA was purified with AMPureXP beads (Beckman Coulter, #A63881) following the manufacturer's protocol. Real-time PCR was performed with SYBR-Green Reagents (Thermo Fisher, #4309155) on a CFX96 Real-Time PCR System (Biorad) with primers targeting the E-Box DNA binding sites in the *PA2G4* gene promoter, 500 bp upstream of the transcription starting site region (forward: CCTCCCCGACCTAGGTGTA; reverse: GCTGAGCGAGAGCCAGTAAC) and *MYC* gene promoter (forward: AGGGTGAGGTCAAGCATTTG; reverse: TGGCCTTGAACCCATACTTC). Fold enrichment was calculated by dividing the input-normalized CT by the negative IgG control CT.

For Chromatin Immunoprecipitation Sequencing (ChIP-Seq), purified DNA was processed using the NEBNext® Ultra™ II DNA Library Prep Kit (#E7645, New England Biolabs, Ipswich, MA). The final libraries were paired-end sequenced using a 150-cycle kit on NovaSeq 600 (Illumina) with a sequencing depth of 50 million reads per sample. Sequencing data were analyzed using the nf-core ChIP pipeline (version 2.0.0) [129] that utilizes MACS2 for peak calling [130] and HOMER for annotation of peaks [131]. Normalized BigWig files were scaled to 1 million mapped reads to be able to compare coverage across multiple samples. Tracks illustrating read coverage and

representative peaks were visualized using the IGV genome browser with Human (GRCh37/hg19) genome [132]. A range of ± 2 kb of the transcriptional start site (TSS) was retained to define promoter-specific peaks.

2.14. Co-Immunoprecipitation

For the endogenous co-immunoprecipitation, HNT34 cells were lysed in modified Cell Lysis Buffer II (Invitrogen #FNN0021) supplemented with Protease and Phosphatase Inhibitors (Sigma #11836153001 and #04-906-837-001) for 30 min on ice and centrifuged at 14,000 RPM for 10 min at 4°C. The protein lysates were then incubated overnight with the following antibodies: EVI1 (Cell Signaling Technology, C50E12 #2593), PA2G4 (Proteintech 15348-1-AP), or Normal Rabbit IgG (Merck, #12-370), at a concentration of 1 µg/mg of IP reaction. Dynabeads protein G magnetic beads (Thermo Fisher, #10003D) were added for 2 hr at 4°C the next day, and then the purified proteins were eluted in 40 µl of 1X L.B. For the overexpression in 293T cells, cells were transfected with Lenti-hEFI1a-ORF-P2A-eGFP-IRES-Puro expressing *MECOM* or *PA2G4* ORF. 48 hr after transfection, the cells were processed similarly Co-IP experiment described above.

2.15. Scaffold-based 3D AML culture

To synthesize collagen scaffolds, an acid suspension of type I collagen was precipitated at pH 5.5 and cross-linked with 1,4-butanediol diglycidyl ether. The scaffold's porosity was generated by a freezing and heating ramp to ensure desired pore size, interconnectivity, and orientation. The materials were sterilized in 70% ethanol for 1 hr and washed in sterile Dulbecco phosphate-buffered saline (Life Technologies, Carlsbad, CA, USA). Scanning electron microscopy was used to characterize the scaffold macrostructure and microstructure. In brief, scaffolds were fixed in 2.5% glutaraldehyde 0.1 M sodium cacodylate buffer for 2 hr at 4 °C, dehydrated in a series of ethanol, dried in a desiccator overnight, and sputter-coated with platinum. Images were acquired with a Nova NanoSEM 230 (FEI, Hillsboro, OR, USA). The human AML cell lines HNT34 and MOLM1 were seeded in 2 x 9-mm scaffolds at concentrations of 0.25 x 10^6, 0.5 x 10^6, and 1 x 10^6 cells. Seeding was

reached by soaking 50 µL of cell suspension in dry scaffolds placed in a multi-well plate. Cells were allowed to adhere for 1 hr at 37 °C before adding the culture medium. After 24 hr, the scaffolds were gently moved onto a new multi-well plate. The medium was replaced every 2-3 days. Cell growth was monitored after 1, 3, and 7 days by MTT assay. Scaffolds were then incubated with 1 mg/mL of MTT solution (Sigma-Aldrich) in culture medium for 2 hr at 37 °C. Cell viability was determined by reading the absorbance at 550 nm. The scaffolds were fixed in neutral buffered formalin, dehydrated in scaling ethanol solutions, and embedded in paraffin to assess cell morphology and distribution. Hematoxylin-and-eosin staining was performed in 5-µm-thick scaffold sections mounted onto Superfrost Plus microslides (Thermo Fisher Scientific, #10149870). Drug treatment was performed after 72 hr from seeding. Drug efficacy was evaluated by MTT assay, as described above. Results were presented as a percentage of cells alive relative to vehicle-treated cells. The drug concentrations that reduced cell viability to 50% of vehicle controls (IC_{50}) were calculated using GraphPad Prism 8 software (La Jolla, CA, USA).

2.16. Virus production and transduction of AML cell lines

For virus production, 3 x 10^6 293T were transfected with 2 µg of pCMV-VSV-G and pCMV-deltaR8.91 vectors (kind gift from Kymberly Stegmaier laboratory, Dana Farber Cancer Institute, Boston, MA, USA). pZIP-hEF1a-RFP-Puro vector (Transomic, Huntsville, AL, USA, #TLHSU1444) harboring the shRNA sequences listed in **Table 1** was used for genetic downregulation experiments.

Table 1. Short hairpin RNA sequences for genetic knock down of *EVI1* (shRNA#16, shRNA#87and shRNA#88), *PA2G4* (shRNA#65, shRNA#66 and shRNA#68) and Not Targeting control.

Gene	ID	Sequence
EVI1	shRNA#16	3’ TAAATTTCTCTTTATCACTTTC 5’ AAAAGTGATAAAGAGAAATTTA Loop: TAGTGAAGCCACAGATG
EVI1	shRNA#87	3’ TATATCATTGTCTTCATCCTCC 5’ AGAGGATGAAGACAATGATATA

		Loop: TAGTGAAGCCACAGATGTA
EVI1	shRNA#88	3' TTCTTCAACTTCTTCATCATCC 5' AGATGATGAAGAAGTTGAAGAA Loop: TAGTGAAGCCACAGATGTA
PA2G4	shRNA#65	3' TAGTGGTTCTCTGTCCTGCATC 5' AATGCAGGACAGAGAACCACTA Loop: TAGTGAAGCCACAGATGTA
PA2G4	shRNA#66	3' TTCATGGTCCTTCTTCTGCTGG 5' ACAGCAGAAGAAGGACCATGAA Loop: TAGTGAAGCCACAGATGTA
PA2G4	shRNA#68	3' TAATTCAGCTTTTTCATGGTCC 5' AGACCATGAAAAAGCTGAATTA Loop: TAGTGAAGCCACAGATGTA
Not Targeting		3' ATGCTTTGCATACTTCTGCCTG 5' AAGGCAGAAGTATGCAAAGCAT Loop: TAGTGAAGCCACAGATGTA

The Lenti-hEF1a-ORF-P2A-eGFP-IRES-Puro (Transomic, Huntsville, AL, USA, #TLO2015.1) vectors containing the *MECOM* (NM_005241.1), *PA2G4* (Gene BankBC001951.1) and *MYC* (NM_002467.6) open reading frame (ORF) sequences were used for genetic overexpression experiments. Cells were transfected using the FUGENE6 protocol (Promega Corporation, #E2691), and viral supernatant was harvested and filtered (0.4 μm) after 72 hr. AML cells were resuspended at a concentration of 4 x 10^6 cells per 1 mL of serum-free RPMI and spin-infected for 1 hr at ambient temperature with 100 μL of lentivirus particles and 8 μg/mL polybrene (Sigma-Aldrich). Puromycin (1 μg/mL) was added for selection (Thermo Fisher Scientific, #A1113803).

2.17. Rapid immunoprecipitation mass spectrometry of endogenous proteins (RIME)

For chromatin immunoprecipitation, cells were fixed with 1% methanol-free formaldehyde (Cell Signaling Technology, #12606) for 8 min and quenched with 0.125

M glycine (Sigma-Aldrich, #G8898). Chromatin was isolated by adding lysis buffer, followed by disruption with a Dounce homogenizer (ActiveMotif, #40401). The lysates were sonicated and the DNA sheared to an average length of 300-500 bp. Genomic DNA (input) was prepared by treating aliquots of chromatin with RNase, proteinase K, and heat for de-crosslinking, followed by ethanol precipitation. Pellets were resuspended, and the resulting DNA was quantified on an ND-2000 NanoDrop spectrophotometer (Thermo Fisher Scientific). Extrapolation to the original chromatin volume allowed quantitation of the total chromatin yield. An aliquot of chromatin (150 µg) was pre-cleared with protein G agarose beads (Thermo Fisher Scientific, #15920010). Proteins of interest were immunoprecipitated using 15 µg of antibody targeting EVI1 (Cell Signaling Technologies, cat. #2593S) and protein G magnetic beads (Thermo Fisher Scientific, #88847). Protein complexes were trypsinized to release the immunoprecipitated from the beads and digest the protein samples. Protein digests were purified using a C18 spin column (Harvard Apparatus, Holliston, MA, USA, #74-7242). The peptides were vacuum-dried using a SPD130XL SpeedVac (Thermo Fisher Scientific).

2.18. Mass spectrometry

Digested peptides were analyzed by LC-MS/MS on a Q Exactive Orbitrap mass spectrometer linked to Dionex Ultimate 3000 HPLC and a nanospray Flex^{TM} ion source (Thermo Fisher Scientific). Samples were loaded directly onto the separation column BEH C18, 75 µm x 100 mm, 130Å 1.7-µm particle size (Waters Corporation, Milford, MA, USA). Peptides were eluted using a 100-min gradient with a 323 nL/min flow rate. An MS survey scan was obtained for the m/z range 340-1600, and MS/MS spectra were acquired using a top 15 method, where the top 15 ions in the MS spectra were subjected to high-energy collisional dissociation. An isolation mass window of 1.6 m/z was used for the precursor ion selection and a normalized collision energy of 27% for fragmentation. A 20-second duration was used for the dynamic exclusion.

Tandem mass spectra were extracted and analyzed by PEAKS Studio version 8 build 20. Charge state deconvolution and deisotoping were not performed. The database consisted of the Uniprot database (version 180508, 71,771 curated entries) and the cRAP database of common laboratory contaminants (www.thegpm.org/crap; 114

entries). The database was searched with a fragment ion mass tolerance of 0.02 Da and a parent ion tolerance of 10 parts per million. Post-translational variable modifications consisted of methionine oxidation, asparagine, and glutamine deamidation. Peaks studio built-in decoy sequencing and FDR determination (decoy fused method) with a cutoff set to -10log*P* > 20 was used to validate MS/MS-based peptide and the parsimony rules for protein identifications. A threshold of ≥-10log*P* of 20 was applied for peptide identifications. The weighted sum of nine parameters for peptide scoring is converted to a *P* value, representing the probability of false identification. Protein identifications were accepted if they could pass the -10log*P* of 20 and contained at least one identified unique peptide. Proteins that contained similar peptides and could not be differentiated on MS/MS analysis alone were grouped to satisfy the principles of parsimony. Proteins sharing significant peptide evidence were grouped into protein groups.

The hit list was generated by taking all proteins (sample vs. IgG control) with a spectral count of five and above from each replicate.

For a label-free quantitation (LFQ) analysis, we included technical and biological replicates (n = 6) in a group named "3q26 AML" and compared them to the group including all the correlative IgG controls (n=6), named "Control". The Thermo raw files were analyzed using MaxQuant (MQ) version 2.4.2.0. The LFQ intensities of proteins from MQ analysis were imported and filtered for reverse identifications (false positives), contaminants, and proteins "only identified by site". Data were transformed to $\log_2$ scale. Then, we imputed missing values and replaced them from a normal distribution. The protein quantification and calculation of statistical significance were performed with a two-sample t-test and with a permutation-based correction controlled with an FDR threshold of 0.05. A protein was considered as EVI1's interactor if the difference between the “3q26 AML” and “Control” groups was statistically significant ($P < 0.05$), the fold change was 4, and it was identified with a minimum of two peptides

2.19. RNA sequencing

PolyA-enriched, strand-specific RNA libraries were generated with the TruSeq mRNA stranded sample preparation kit (Illumina, San Diego, CA, USA, #20020594) starting from 1 µg of RNA from each sample. In brief, RNA was subjected to polyA selection

using magnetic oligo-dT beads (Thermo Fisher Scientific, #61002). A 94 °C-incubation for 4 min partially fragmented polyA RNA. Both actinomycin-D (during the first-strand cDNA synthesis) and dUTP (during the second-strand synthesis) were used to keep the strand information. The libraries were end-repaired and adenylated before being ligated with Y-shape single-indexed adapters and amplified by 11 PCR cycles. The last purification step was performed with Ampure XP beads (Beckman Coulter, #A63882) at 0.8x to remove all adapter dimers. Each library was quantified and quality-controlled using a Qubit 4 fluorometer (Thermo Fisher Scientific) and LabChip GX (Perkin Elmer, Waltham, MA, USA). The adaptor-tagged pool of libraries was loaded onto Illumina Hiseq2500 rapid-run flow cells (SR100 chemistry) for cluster generation and deep sequencing. The raw sequence files were quality-controlled using FastQC (v 1.3) (http://www.bioinformatics.babraham.ac.uk/projects/fastqc/, accessed in May 2020). Transcripts were aligned using the STAR package (v2.7.1a) and quantified using the "quantMode GeneCounts" function with ENSEMBL annotation and the human genome version GRCh38 as a reference. Read counts generated by STAR were analyzed using the DESeq2 R package to detect differentially expressed genes (DEGs) with an adjusted *P* value (*Adj.P*) less than 0.05.

2.20. Single cell RNA sequencing

Sequencing were carried out at the University of Texas MD Anderson Cancer Center's Advanced Technology Genomics Core (PR#002 and PDLX_PR#003) or at the NGS core facility of the Istituto Romagnolo per lo Studio dei Tumori "Dino Amadori" (PR#008). Cell viability was detected using the Countess II FL Automated Cell Counter (Thermo Fisher Scientific). Single cells were lysed, barcoded, and normalized for input onto the Chromium Single Cell A Chip Kit (10x Genomics, Pleasanton, CA, USA). Indexed sample libraries were pulled together and sequenced using a NovaSeq6000 SP 100-cycle flow cell (Illumina). Sequencing reads were aligned to the human genome version GRCh38. A digital expression matrix was generated for each sample using Cellranger software (10x Genomics), and the data were integrated using Harmony and analyzed using Seurat (R package) [133, 134]. Cells with less than 100 genes and 500 unique molecular identifiers were excluded from the analysis. Cell types were assigned using the Seurat label transferring method and a bone marrow–specific

reference (included in the SeuratData package). Conserved markers and differentially expressed genes were identified for each cluster/cell type using the Benjamini-Hochberg method to *Adj.P* for multiple testing. Statistically significant DEGs for each cluster/cell type were used to perform a gene set enrichment analysis (GSEA) using the ClusterProfiler package and the Hallmark gene-set from MSigDB. Furthermore, the identification of the leukemic cell population was assessed by computing a transcriptional signature score using the UCell R package (score ≥ 0.2) based on the expression of leukemia-associated immunophenotype for PR#002 (CD34, KIT, CD33, ANPEP, CD38, CD7, NCAM1, CD4, CD19, DNTT, ITGB3, HLA-DRA, HLA-DRB1, and HLA-DRB5) and PDLX_PR#003 (CD34, CD45 KIT, CD33, ANPEP, CD38, CD2, TFRC, HLA-DRA, HLA-DRB1, HLA-DRB5, MYC, and MECOM) in the treated and untreated samples, PR#008 (CD34, KIT, CD33, ANPEP, CD38, CD2, TFRC, MECOM, HLA-DRA, HLA-DRB5, HLA-DRB1, PTPRC, MYC).

2.21. Next-generation sequencing

DNA was extracted using a Maxwell® 16 DNA purification kit (Promega, #AS1010), following the manufacturer's instructions. The concentration and purity of the DNA samples were determined with a Qubit 4 fluorometer (Thermo Fisher Scientific, #33226). Primary samples were sequenced at the NGS platform of the University-Hospital of Parma using the "Myeloid Solution" kit (Sophia Genetics SA, Saint Sulpice, Switzerland, #BS.0207.0102-48). Library preparation and sequencing were performed on a MySeq system (Illumina) following the manufacturer's instructions. Data were analyzed with Sophia DDM® software version 5.10.11.1 (Sophia Genetics SA).

2.22. Animal Models

Patient-derived leukemia xenografts (PDLXs) were established by tail vein injection of mononucleated cells (2.0 x 10^6) isolated from AML patients, PR#003, PR#008, PR#009, with t(3;3)(q21.3;q26.2), t(3;3)(q21.3;q26.2), and inv(3)(q21.3q26.2), respectively, into 6-week-old male non-obese diabetic, severe combined immune-deficient, interleukin (IL)-2 receptor gamma-deficient mice (NOD-*SCID* IL2Rgamma^{null}, NSG, The Jackson Laboratory, Charles River Italia). Leukemic cell engraftment was

monitored every 2 weeks by flow cytometry of peripheral blood cells stained with an anti-human CD45-PE antibody (Becton Dickinson, Franklin Lakes, NJ, USA, #555483). For PDLX_PR#003, 10 × 10^6 cells were injected into the flank to establish a subcutaneous orthotopic model. Mice' body weight and tumor growth were evaluated every two days using caliper measurements. Tumors did not exceed 10% of the animal's body weight and had an average diameter of 15 mm. Mice were housed in specific-pathogen-free conditions (25°C, 12-hr light/12-hr dark cycle, 50% humidity). All procedures were approved under the MD Anderson (Houston, TX) Institutional Animal Care and Use Committee protocol or the N.682/2019-PR protocol at the University of Parma. Mice were sacrificed when signs of distress were observed.

For pharmacodynamic studies, three 6-week-old male NOD-*SCID* IL2Rgamma^{null} (NSG, The Jackson Laboratory, Charles River Italia) mice were treated when cell engraftment of circulating hCD45 reached at least 10% of the total mononucleated cells in peripheral blood with a single administration of 10 mg/kg entinostat (PDLX_PR#003 and PDLX_PR#009) or 50 mg/kg of WS6 (PDLX_PR#009) diluted in DMSO (Sigma-Aldrich, #276855); peripheral blood cells were collected before and after 6 hr of treatment with HDACis for immunofluorescence analysis.

For efficacy studies we used the triple-transgenic NSG-SGM3 (NSGS)(PDLX_PR#003) mice expressing human IL3, GM-CSF (CSF2), and SCF (KITLG) or NSG (PDLX_PR#008). AML leukemia cells (1 x 10^6) from the PDLX_PR#003 and (10 x 10^6) PDLX_PR#008 model were transplanted by tail vein injection in 12- to 16-week-old male and female NSGS mice, irradiated (125 cGy) 12 hr before transplantation (PDLX_PR#003). Engraftment of human PDLX cells was monitored every 2 weeks by flow cytometry of bone marrow–aspirated samples (PDLX_PR#003) or peripheral blood (PDLX_PR#008) stained with an anti-human CD45 antibody (BD Bioscience, Franklyn Lakes, NJ, USA, #AB11153499, #555482 and #555483, all diluted 1:40). Mice were selected for treatment randomization 4 to 6 weeks after transplantation when the human fraction of cells in the bone marrow was ≥ 0.5% or ≥ 0.1% in the peripheral blood. Entinostat (MedChemExpress, Sollentuna, Sweden, #HY-12163) and azacitidine (Selleck Chemicals, #S1782) were dissolved in DMSO, diluted in sterile PBS, and administered by oral gavage at 10 mg/kg per five days/week for three weeks and by intraperitoneal injection at 1 mg/kg per five days respectively. WS6 was dissolved in Tween 80 (50:50), diluted in sterile PBS, and

administered by intraperitoneal injection (IP) at 25 mg/kg per five days/week for three weeks. Mice were euthanized by cervical dislocation and organ biopsies (tibias and femurs) were collected from animals and fixed overnight in 10% neutral-buffered formalin (Sigma-Aldrich, # HT501128-4L). Tibias or vertebrae were incubated for 24 hr in Cal-Ex (Thermo Fisher Scientific, #C511-1D) to remove calcium residues and then dehydrated and preserved in 70% ethanol at ambient temperature. Fixed tissues were then embedded in paraffin following standard protocols. Leukemic cells were released from femurs and tibias by mechanic crushing in a solution of 2% FBS/PBS and filtered using 30-µm pre-separation filters (Miltenyi Biotec, Bergisch Gladbach, Germany #130-041-407) prior to analysis of hCD45 by flow cytometry.

2.23. Statistical analysis

Statistical analyses were performed using GraphPad Prism 8 or R software. The means, standard deviation (±SD), group size, experimental details, and statistical significance are described in the figure legends in the methods section. The assumption of normal distribution was not determined, and the *P* value among samples was calculated by parametric and non-parametric t-test. We used one- or two-way ANOVA using statistical correction for multiple comparison algorithms, as specified in the figure legends, to determine appropriate significance among groups.

The information presented in this thesis has been previously published in the article: Marchesini M, Gherli A, **Simoncini E**, et al. Orthogonal proteogenomic analysis identifies the druggable PA2G4-MYC axis in 3q26 AML. Nat Commun. 2024;15(1):4739 [1].

3. Results

3.1. Identification of small molecules modulating *EVI1*

We performed a phenotypic screen focusing on antiproliferative agents in parallel with a gene-expression-based screen approach to identify molecules that impair cell proliferation by suppressing an *EVI1* signature (**Figure 1A**) in AML cells overexpressing EVI1 ($EVI1^{High}$). We screened 5292 drugs or drug-like small molecules, including natural derivative compounds in the human 3q26 $EVI1^{High}$ AML cell lines MOLM1 and UCSD/AML1 carrying the chromosome recombinations inv(3)(q21.3q26.2) and t(3;3)(q21.3;q26.2), respectively. We scored compounds based on their ability to suppress proliferation compared to vehicle controls (ΔPOC). We selected 228 (95th percentile) small molecules to pursue further based on ΔPOC inhibition (**Figure 1B**). The effect of compound treatment was normally distributed, and the majority of the compounds did not impair cell viability (**Figure 1C, D**). Plate-specific spatial biases did not affect the experimental screening data (**Figure 1E**), except for differences due to cell lines. Among top-scoring hits, with the potential for clinical translation, HDACis, proteasome modulators, topoisomerase and protein kinase inhibitors reduced the growth of $EVI1^{High}$ AML by 90% (**Figure 1F**). Of these, 40 small molecules with the highest ΔPOC index (> 84%, *Adj.P* ≤ 2 x 10^{-33}) were counter-screened in an additional t(3;3)(q21.3;q26.2) $EVI1^{High}$ AML cell line (HNT34) and two not-translocated ($EVI1^{Low}$) AML cell lines, NOMO1 ($KRAS^{G13D}$) and THP1 ($NRAS^{G12D}$); these were selected because they carry mutations in the RAS signaling [65] as in 3q26 AMLs. The HDACis AR-42, belinostat, trichostatin A, and entinostat preferentially affect the proliferation of $EVI1^{High}$ AML cells compared to $EVI1^{Low}$, suggesting that EVI1 sensitizes 3q26 AML cells to HDACi-mediated cytotoxicity (**Figure 1G**).

We redefined an *EVI1* transcriptional signature from genome-wide expression profiling of $EVI1^{High}$ AML (TF1) transduced with a siRNA targeting *EVI1* [135]. We obtained a set of 1428 modulated genes ($P \leq 0.05$ by the two-sided Student's t-test) and selected the top 100 up- or down-regulated genes, ranked by the signal-to-noise ratio, to define an *EVI1* "*On"* versus an "*Off"* state (**Figure 2A**). We then interrogated publicly available large-scale chemical and genetic perturbation datasets (https://clue.io/cmap) [125] to identify small molecules that mimic *EVI1* transcriptional suppression. HDACis ranked

on the top of the hit list were associated with the *EVI1* "*Off"* status (**Figure 2B**). Most (56.2%) of the HDACis sampled in the CMap libraries scored among the top 250 hits (*P* = 0.0006, **Figure 2C**)**.** However, because HDACis are overrepresented in small molecule libraries compared to other classes, we determined whether the size of the compound class (n = 32) interfered with our result. Compound classes with similar or higher representation, such as histamine (n = 52), glucocorticoid, (n = 47), or acetylcholine receptor antagonists (n = 66), did not show significant enrichment with an *EVI1* "*Off* "status (**Figure 2D**). Consistently, a tertiary screen of 4942 small molecules confirmed the potent antiproliferative activity of HDACis compared to non *EVI1* "*Off*" inducers (**Figure 2E**) in TF1 cells.

To validate data derived from the analysis of published datasets [135], we downregulated *EVI1* by shRNA in HNT34 cells and detected changes in RNA abundance with more than 2224 transcripts changing from $\log_2$ fold ≥ 2 (false discovery rate (FDR) ≤ 0.01) (**Figure 2F**). The overlap between *EVI1*-regulated gene signatures in HNT34 and *EVI1*-dependent genes in TF1 (**Figure 2G**) indicates their appropriateness for additional gene-expression-based *in silico* drug screening approaches. Projection of the HNT34 signature onto the LINCS L1000 [136] dataset space demonstrated that transcriptional changes associated with an *EVI1 "Off"* status mimic and match HDACis signatures (**Figure 2H-J**). The suppression of an *EVI1*-transcriptional program due to HDAC perturbation was also replicated in a separate dataset derived from AML cell lines distinguished based on their 3q26 status (**Figure 2H-J**) [38].

Taken together, these data suggest that HDACis inhibit 3q26 AML cell proliferation and modulate *EVI1*, supporting their investigation as a targeted approach in 3q26 AMLs.

3.2. HDACis suppress 3q26 AML growth

To set conditions for validating our results, we confirmed the expression of EVI1 and ΔEVI1 protein isoforms [99] in the 3q26 $EVI1^{High}$ AML cell lines (**Figure 3A, B**) and demonstrated the dependency of these cells on EVI1 expression (**Figure 3C-E**). Suppression of *EVI1* abrogates the growth and the clonogenic capacity of $EVI1^{High}$ AML (**Figure 3E, F**).

We then selected a panel of molecules with pan (AR-42, belinostat) or selective (entinostat, class 1/2) HDAC inhibitory activity based on their potential in clinical translation in high risk-AML. AR-42 (ΔPOC = 99.54; *Adj.P* = 1.51 x 10^{-34}) has been investigated in clinical trials for the treatment of hematologic malignancies (e.g. NCT01129193 and NCT02569320); belinostat (also known as PXD101, ΔPOC = 98.14; *Adj.P* = 1.51 x 10^{-34}) has been approved for cutaneous of T-cell lymphoma [137]; and entinostat (ΔPOC = 87.43; *Adj.P* = 7.55 x 10^{-34}) has been tested in myeloid malignancies, irrespective of the genetic status (e.g. NCT00313586 and NCT01159301) [138]. All molecules displayed half-maximal inhibitory concentrations (IC_{50}) within the low micromolar range: AR-42 from 0.221 μM to 0.438 μM (0.329 ± 0.153), belinostat from 0.379 μM to 0.951 μM (0.665 ± 0.404), and entinostat from 0.812 μM to 1.686 μM (1.249 ± 0.618) (**Figure 4A**). Treatment with HDACis also induced a dose-dependent increase in apoptosis (**Figure 4B, C**), and suppressed blast colony formation (**Figure 4D, E**).

3.3. EVI1 sensitizes 3q26 AML to HDAC-mediated suppression

To test whether the effects of HDACis were due to EVI1 suppression, we treated $EVI1^{High}$ AML cell lines with AR-42, belinostat, and entinostat and observed a loss of EVI1 both at transcriptional and protein level. In contrast, cleaved caspase 3 was regulated in the opposite direction, consistent with the apoptosis data presented above (**Figure 5A-C**).

In addition, the interaction of 3q26 AML cells with a collagen substrate in a three-dimensional (3D) porous and cell-permeant culture system [139] (**Figure 5D**) used to mimic the bone marrow microenvironment did not rescue the cytotoxic effect of HDACis. Here, $EVI1^{High}$ cells aggregate in niche-like structures similar to AML clusters in the bone marrow stroma, retain EVI1 expression, and grow with a doubling time of ~ 6 six days (**Figure 5E-G**). $EVI1^{High}$ cells cultured in biomimetic 3D collagen scaffolds develop resistance to ara-C but not to HDACis, suggesting that cell-extrinsic mechanisms of acquired resistance to chemotherapy agents can be overcome by targeting EVI1 in 3q26 AML (**Figure 5H**).

To further assess whether EVI1 sensitizes AML cells to HDAC inhibition, we leveraged an EVI1-inducible leukemia model [140]. U937T cells that conditionally expressed the full-length isoform of *EVI1* under the control of the tetracycline promoter were grown in the presence (*EVI1* "*Off*") or absence of tetracycline (*EVI1* "*On*"). EVI1 expression was observed 24 hr after tetracycline removal (**Figure 6A, B**). U937T (E10 clone) were then treated with AR-42, belinostat, and entinostat in a 2-fold dilution series for three additional days. Despite a growth difference between U937T "*On*" or "*Off*" (**Figure 6C**), cells grown in the absence of tetracycline, with the highest EVI1 expression, were more sensitive to the effects of HDACis (**Figure 6D**). $EVI1^{High}$ and $EVI1^{Low}$ U937T were equally sensitive to ara-C, suggesting that the expression of EVI1 preferentially enhances the HDACi-induced inhibition of cell viability compared to chemotherapy (**Figure 6D**). Similar results were obtained in a constitutive model of *EVI1* expression in HL-60 cells (**Figure 6E-G**). We then sorted MOLM1 cells by size, distinguishing EVI1-positive cells with large nuclei and prominent nucleoli, and EVI1-negative cells, smaller in size with weak or no EVI1 protein expression (**Figures 3B** and **6H, I**)**.** In this isogenic model, HDACis were more active in MOLM1 $EVI1^{High}$ cells compared to MOLM1 $EVI1^{Low}$ (**Figure 6J**). Consistently, $EVI1^{High}$ (n = 5) and $EVI1^{Low}$ (n = 7) AML cell lines were equally sensitive to other chemotherapy agents but not to AR-42, belinostat, and entinostat (**Figure 6K**).

Collectively, these data demonstrate that EVI1 expression in 3q26 AML sensitizes cells to HDAC inhibition, providing a rationale for translating these molecules in clinical practice.

3.4. HDACis suppress $EVI1^{High}$ in patients with 3q26 AML

Since January 2017, we have admitted five patients to our hospital affected by AML carrying 3q26 abnormalities and collected six additional samples from different institutions (PR#001-009 and PR#023-024). Four out eleven patients had atypical 3q26 rearrangements (PR#001, PR#004, PR#005 and PR#024) (**Figure 7A**). Sequencing and cytogenetic analyses confirmed a high frequency of RAS mutations [64] (63.6% mutated in *KRAS* or *NRAS*) and monosomy of chromosome 7 (63.6%) compared to non-rearranged cases (PR#0010-022 and PR#025-039) (**Figure 7B**). All

patients carrying 3q26 abnormalities presented severe clinical conditions and experienced disease relapse after multiple lines of chemotherapy or HSCT. In primary AML blasts, suitable for *ex vivo* studies, AR-42, belinostat, and entinostat inhibited cell viability in 2D and 3D models (**Figure 8A-C**). 3q26 AML cells collected from clinical samples (n = 9) were more sensitive to HDAC suppression than were other AML subtypes (n = 28) and equally responsive to chemotherapy agents *in vitro* (**Figure 8D**). For samples with adequate cells for additional tests, EVI1 expression was almost undetectable after 24 hr of HDACis treatment, consistent with the disappearance from the nucleus, and inversely correlated with the increase of cleaved caspase 3 (**Figure 8E-G**). Importantly, ara-C did not cause significant changes in EVI1 nuclear protein abundance (**Figure 8F-H**).

Three patients (PR#001, PR#002, and PR#003) were enrolled in a compassionate use program that tested azacitidine at 50 mg/m^2 (days 1-10) and entinostat 4 mg/m^2 (days 3 and 10), every 28 days. This schedule was approved in the NCT00101179 clinical trial for AML or myelodysplastic syndromes [141]. Two patients received standard support or chemotherapy (PR#004 and PR#005); the remaining were treated in a different hospital. The mean survival duration of patients receiving an entinostat-based regimen was 20.3 months without significant organ toxicity compared to 4.5 months for those receiving standard of care (**Figure 9A, B**).

Leveraging previous studies describing the pharmacokinetics properties of entinostat [142], we also demonstrated that EVI1 protein levels markedly decrease in circulating AML blasts following 4 mg/m^2 of entinostat compared to ara-C both in treated patients (**Figure 9C**) or in the matched 3q26 PDLX models (**Figure 9D**).

In summary, these data support the idea of testing HDACi-based combination therapy in patients with 3q26 AML in randomized clinical trials and suggest the use of EVI1 as a potential biomarker of response to epigenetic treatment or resistance to standard of care (**Figure 9E**) in patients with EVI1-dependent leukemia.

3.5. EVI1 inhibition modulates the Myc transcriptional program

We then hypothesized that the preferential activity of HDACis in 3q26 AML may be related to the impaired function of the EVI1 co-transcriptional complex. We profiled EVI1^{High} AML cell lines after 16 hr of treatment with AR-42 (0.5 μM and 1.0 μM, respectively) and entinostat (2 μM and 4 μM, respectively) by mRNA and ChIP-Seq. Consistent with the role of HDAC in chromatin-dependent transcriptional regulation, there was a preponderance of up-regulated genes (1309) versus down-regulated genes (107) (**Figure 10A**). To assess the effects of HDACis on the transcriptional programs regulated by *EVI1*, we interrogated our data with four well-validated gene signatures for statistically significant enrichment by single-sample gene set enrichment analysis (ssGSEA) [143]. We incorporated the following databases: Molecular Signatures Database (MSigDB) of 50 gene sets, Elsevier of 1721 gene sets, Kyoto Encyclopedia of Genes and Genomes (KEGG) of 308 gene sets, and BioPlanet datasets of 1510 gene sets. In each database, we combined EVI1^{High} datasets derived from the analysis of *EVI1* upregulated signatures in primary myeloid leukemias cells carrying 3q26 abnormalities (GSE14468, GSE134589) [102, 144]. Next, we determined whether any of the gene sets in our selected collection were significantly enriched in EVI1^{High} AML treated with DMSO (control) compared to those treated with HDACis. Data from the four databases revealed that treated samples were strongly correlated with signatures associated with the modulation of *MYC* oncogene (**Figure 10B, C**).

We then set up a longitudinal study and profiled bone marrow cells of PR#002 by single-cell RNA sequencing (scRNASeq) before and after four cycles of azacitidine and entinostat. A cluster dimensional analysis revealed 18 groups of transcriptionally distinct cell populations, among which 15 were represented in both samples (**Figure 10D**). After treatment, we observed a reduction of the more undifferentiated myeloid compartment and a stimulatory effect, as seen before with HDACis [145], on the immune system cells (**Figure 10E**).

Next, we computed a score based on the combined expression of the patients' leukemic markers (*CD34*, *KIT*, *CD33*, *ANPEP*, *CD38*, *CD7*, *NCAM1*, *CD4*, *CD19*, *DNTT*, *ITGB3*, *HLA-DRA*, *HLA-DRB1*, and *HLA-DRB5*) using UCell [146] and identified

the leukemic population (LP) in the PR#002 clone as the group of cells with score > 0.2. This population accounts for 29.5% of the sample and is predominantly composed of hematopoietic stem cells (HSCs) (61.4%) and lympho-myeloid primed progenitor (LMPP) (31.6%) cell types. After therapy, LP decreased to 3.1% while maintaining a similar proportion of the cluster distribution (70.7% HSCs and 20.2% LMPP) if compared with the sample before treatment (**Figure 10F, G**).

In HSCs, LMPP, or LP cells, highly expressed genes are correlated with Myc-associated gene sets, suggesting an inhibitory effect on Myc signaling after azacitidine and entinostat treatment in human 3q26 AML (**Figure 10H, I**). Consistently, we observed a reduction in MYC expression in the leukemic cells in the bone marrow of PR#002 after two cycles of azacitidine and entinostat (**Figure 10J**). Perhaps it was not surprising that genetic or HDACi-mediated suppression of *EVI1* led to a decrement of MYC in cell lines and in *ex vivo* $EVI1^{High}$ AML patient blasts (**Figure 10K-M**). This result is consistent with ChIP-Seq findings that reveal a biding of *EVI1* at the *MYC* promoter locus marked by acetylated histone H3K27 (H3K27Ac). This pattern is significantly diminished following treatment with HDACis treatment (**Figure 10N**).

Next, we asked whether azacitidine contributed to the clinical response seen in 3q26 AML patients and whether azacitidine played a part in the observed phenotypes. Then, we recapitulated our clinical protocol testing azacitidine and entinostat in a 3q26 PDLX model**.** We showed that entinostat controls proliferation**,** *EVI1* modulation and a Myc signaling of PDLX_PR#008 LP (**Figure 11A-D**) with minimal contribution from azacitidine (**Figure 11E-G**).

Finally, to exclude a direct effect of HDACis on MYC as previously reported for other cancers [147-149] we compared the effects of AR-42, belinostat and entinostat in AML MYC^{High} versus MYC^{Low} (**Figure 12A, B**) or by overexpressing *MYC* in the U937T inducible model (**Figure 12C, D**). Differently from *EVI1,* in these models, *MYC* did not render cells more sensitive to HDAC inhibition whereas, as expected, it exhibited this effect for JQ-1, a potent repressor of *MYC* super-enhancers (**Figure 12E, F**) [111]. While we cannot exclude an effect of azacitidine on the leukemia response in humans, these results suggest that an HDAC epigenetic-based therapy limits Myc pathways in 3q26 AML and that azacitidine-based protocols may not be as effective in 3q26 AML as they are in other AML subgroups.

3.6. PA2G4 bridges EVI1 with Myc signaling

To prioritize any significant pathway scored by ssGSEA, we dissected the EVI1 chromatin-associated complex by rapid immunoprecipitation mass spectrometry (MS) of endogenous proteins (RIME) [150]. We performed these experiments in UCSD/AML1 and HNT34 cell lines and cells derived from the PDLX_PR#003 model (**Figure 13A**). This model retained the parental t(3;3)(q21.3;q26.2) and EVI1 expression in the tumor mass (**Figure 13B, C**). We identified 107 EVI1-interacting proteins in HNT34 cells, 117 in UCSD/AML1, and 155 in the PDLX model sample (**Figure 13A**). Sixty-nine were common in all samples (**Figure 13D**). Among EVI1 protein partners, we found that translation-related proteins were represented prominently, as well as translational initiating factors (1), ribosomal proteins (47) and RNA binding factors (2), transcription factors (2), histones (2), and DNA and RNA processing proteins (4). A small group of proteins with heterogeneous functions (CENPV, RPN1, FBL, SND1, PARP1, PA2G4, PABPC1, RACK1, MTDH, and ESYT1) was also recovered. In addition, EVI1 partners identified by stable isotope–labeling amino acids in cell culture–based quantitative proteomics, such as PARP1, XRCC5, RPS19, and H2AZ [151], were also identified by our approach.

We intersected the 69 hits with the enriched genes scored by ssGSEA. Eleven of the 69 RIME targets were represented in the *MYC Targets V1 pathway.* In all other instances, the intersection resulted in two or fewer hits, suggesting that EVI1 and Myc signaling share co-regulators in their transcriptional machinery (**Figure 13E**). Ten out eleven these proteins were confirmed by repeating the analysis of MS RIME data with a label-free quantification (LFQ) approach (**Figure 13F**). A difference in *EVI1*-dependent transcriptional regulation was demonstrated with HDACis in only 3 of 11 common hits: Fibrillarin (*FBL*: $\log_2$ fold change = -0.74, *Adj.P* = 0.017), nucleolar RNA helicase 2 (*DDX21*: $\log_2$ fold change = -0.69, *Adj.P* = 0.006), and, proliferation-associated 2G4 (*PA2G4:* $\log_2$ fold change = -1.45, *Adj.P* = 1.34 x 10^{-06}) (**Figure 13G, H**) that was retained for validation since, in our model, PA2G4 interacts with EVI1 (**Figures 13A, 14A, B**) and is transcriptionally repressed by HDACis treatment (**Figure 14C**).

PA2G4 is involved in protein translation, cell cycle progression [152-154], and a cancer-druggable feed-forward transcriptional regulator of *MYCN* in neuroblastoma

[155]. Similarly, *PA2G4* is positively correlated with *MYC* expression in AML primary datasets (GSE14468, n = 524 and GSE134589, n = 672; **Figure 14D**) [156, 157] and interestingly, both *EVI1* and *MYC* occupy the promoter region upstream *PA2G4* transcription site (**Figure 14E**), suggesting that these genes are required for *PA2G4* control in 3q26 leukemia (**Figure 13G**).

We next addressed whether the effect of HDACis on *EVI1* was at least partly related to PA2G4 and showed that *PA2G4* knockout abrogates EVI1 and consequently MYC protein (**Figure 14F**); it then prevents the growth and formation of colonies in 3q26 AML (**Figure 14G, H**). Conversely, the overexpression of *PA2G4* increased EVI1 and MYC protein levels (**Figure 14I**) and partially rescued AML cells from the apoptotic effect of HDAC inhibition (**Figure 14J**), suggesting that PA2G4 is a putative mediator of HDAC inhibition.

Because genetic loss of *PA2G4* occurs in the absence of transcriptional regulation of *EVI1* or *MYC* (**Figure 14K**), we speculated that PA2G4 protects EVI1 from proteasome degradation, as seen for MYCN in neuroblastoma [155]. Consistently, MG132 treatment partially rescues the EVI1 level in 3q26 AML cell lines (**Figure 14L**), suggesting that PA2G4 acts as a scaffolding protein for *EVI1* transcriptional complex.

Taken together, our data suggest that PA2G4 bridges EVI1 to MYC and supports the disruption of this protein to diminish their respective oncogenic signals in this leukemia subtype.

3.7. Selective PA2G4 inhibitor WS6 depletes EVI1 and MYC signaling and blocks 3q26 AML *in vivo*

The selective PA2G4 inhibitor, WS6, was recently identified on high-throughput screening for inducers of β pancreatic islet cells [158]. WS6 is a dyarilurea compound that interferes with PA2G4-MYCN binding [155]. Given the homology of *MYC* to *MYCN* [159], we tested this molecule with the functional assays described above. WS6 inhibited cell proliferation greatly in AML $EVI1^{High}$ vs. AML $EVI1^{Low}$ (**Figure 15A-D**) and potentiate the effect of HDACis (**Figure 15E**). To exclude the WS6 off-target effect, we demonstrated that WS6 lacks activity against HDAC in biological assays, as shown by the comparative quantification of H3K27 acetylation and β-tubulin in $EVI1^{High}$-treated

AML cell lines (**Figure 15F**). WS6 markedly decreased MYC and EVI1 in EVI1^{High} primary blasts and EVI1^{High} AML cell lines (**Figure 15G, H**) and consequently their occupancy at the *PA2G4* promoter (**Figure 14E**). Similarly to HDACis, WS6 diminished EVI1 expression in circulating AML cells in 3q26 PDLX models *in vivo* (**Figure 16A**). WS6 is a tool compound that has not yet been optimized for continuous systemic delivery; thus, we tested the tumor-suppressing capacity of this molecule by treating two 3q26 AML PDLXs (PDLX_PR#003_ PDLX_PR#008) models at 25 mg/kg for 5 days/week for 15 days. We demonstrated that IP administration of WS6 inhibited LP progression, compared to vehicle-treated control, traced by hCD45+ (**Figure 16B, C**) or scRNASeq quantification (**Figure 16D, E**). No major toxicities were seen in treated animals. In addition, EVI1 and MYC protein levels were diminished in WS6-treated tumors compared to vehicle-treated control animals (**Figure 16F, G**), linking growth inhibition (Ki67) to the suppression of EVI1-MYC.

Taken together, these results demonstrate that PA2G4 is a druggable mediator of EVI1 complex and suggest that PA2G4 inhibitors should be selectively optimized for clinical applications.

The information presented in this thesis has been previously published in the article: Marchesini M, Gherli A, **Simoncini E**, et al. Orthogonal proteogenomic analysis identifies the druggable PA2G4-MYC axis in 3q26 AML. Nat Commun. 2024;15(1):4739 [1].

4. Discussion

Despite recent advancements in the treatment of low- and intermediate-risk AML by targeting mutationally activated kinases [160-162] and newer initial treatment options for a subset of patients [163, 164], high- risk AML with recurrent genetic abnormalities, such as inv(3) (q21.3q26.2) and t(3;3)(q21.3;q26.2) remains a significant clinical challenge. In these patient subgroups, induction [165, 166] and maintenance cytotoxic chemotherapy have consistently failed to show a benefit [167]. Patients with 3q26 AML, for example, eventually experience relapse, even after allogeneic hematopoietic cell transplantation with curative intent [168, 169].

In this case, the development of a small molecule that can block the activity of EVI1 would be an attractive approach [170-172]. Given this temporary absence, an alternative is to focus on unbiased strategies, searching for modulators in one or more leukemogenic steps in the metabolic, transcriptional, or epigenetic pathways that are aberrantly activated by EVI1 in 3q26 AML [38, 119]. Closer to clinical translation, the PARP inhibitor emerged as a transcriptional repressor of *EVI1* by decreasing the interaction frequency between the *G2DHE* and the *EVI1* promoter [115]. However, the risk of secondary myelodysplastic syndrome and AML in cancer patients treated with PARP inhibitors such as olaparib and veliparib [173] raises concerns about their use in myeloid leukemia and hematological malignancies more broadly.

Our strategy was meant to identify clinically ready solutions to modulate EVI1 in 3q26 AML.

Among potential targets, we decided to validate structurally different pan-HDACis and more selective molecules in various stages of clinical development and subsequently identified a potential mediator of this response.

The functional interaction of EVI1 with the HDAC complexes was initially postulated in heterologous cells transfected with different *EVI1* cDNAs isoforms [101, 174, 175] or by quantitative proteomics combined with yeast two-hybrid screens and subsequently validated by coimmunoprecipitation experiments with endogenous EVI1 in cancer cell lines [151]. While collectively, these studies suggest that EVI1 mainly associates and cooperates with HDAC1 [101, 151, 175], HDAC2 [151] (class I), or HDAC4 (class II) [100], the number of studies validating EVI1-HDAC co-transcriptional complex in human 3q26 AML and cancer models is surprisingly low.

Nevertheless, our results for EVI1 expression upon HDACis treatment place this compound class in a fascinating scenario. While HDACis have been shown to induce histone hyperacetylation, apoptosis, and anti-proliferative activities against a wide range of rearranged leukemia cell lines or mouse models preclinically, no pharmacodynamic demonstrations exist of their target engagement in AML clinical trials. Further research will be crucial to uncover their potential as therapeutic agents in 3q26 AML, particularly with the next generation of selective HDACis.

MYC is broadly altered in AMLs [176] and it is an independent prognostic factor in high-risk AMLs, especially those associated with myelodysplasia-related changes (AML-MRC) [177-179]. Ottema and colleagues recently found that the translocation of the *MYC SE* leads to *EVI1* overexpression in t(3;8)(q26;q24) AML [74]. This data suggests that therapeutic approaches that interfere with TFs and co-activators docking to this prototypical location (SE-EVI1 promoter) negatively affect EVI1 expression in t(3;8)(q26;q24) or other 3q26 rearranged cases. However, the identification of EVI1 interactome in AML is still lacking. Previous studies identified potential EVI1 interactors in different tumor types [91, 104, 151, 180, 181] but, given the heterogeneity of these models, the number of genes overlapping across these approaches is low.

While we confirmed the co-immunoprecipitation of previously reported putative EVI1 co-regulators, such as PARP1, XRCC5, RPS19, and H2AZ [151], we did not observe enrichment for HDACs or MYC by RIME. The interaction with the HDAC machinery, and hence the response to therapy, might be indirect and mediated by different co-regulatory proteins. We showed that PA2G4 contributes to linking HDAC response to EVI1 loss and, in turn, to MYC suppression.

PA2G4 accounts for 10 exons and encodes two splice *PA2G4* (also known as ErbB3-binding protein 1, EBP1) variants, p48 and p42. The difference, 54 amino acids in the N-terminus, between the long and short isoforms directs unique function, oncogenic or tumor suppressive [182], and association with different binding partners and their regulation [183]. p48 PA2G4 is the dominant form that is highly expressed in mammalian cells during embryogenesis or re-expressed in several cancer types, including glioblastoma multiforme and lung cancer [184, 185]. p42, the short form, is scarcely detectable in cancers, while its tumor-suppressive role has been established in several tumor models [185-187].

Similar to a *MYCN*-dependent neuroblastoma model [155], the genetic and chemical disruption of the PA2G4-MYC interface with the small molecule inhibitor WS6 [158] altered AML cell proliferation, supporting an oncogenic role of PA2G4 in 3q26 AML. In AML, the mechanistic role of PA2G4 has not yet been investigated. Previous studies demonstrated that PA2G4 is highly expressed in AML clinical samples compared to mononuclear cells from healthy donors [188]. However, since only a few cases have been cytogenetically characterized [188], it is impossible to speculate whether patients carrying 3q26 aberrancies express a higher level of PA2G4 than do other subgroups. Interestingly, *PA2G4* is part of a transcriptional core signature of four genes (*DNMT1*, *MYB*, *PA2G4*, and *YBX1*) repressed with de-differentiation in all-trans retinoic acid-induced NB4 and HL-60 AML cell lines, suggesting that PA2G4 plays a role in AML maintenance [189]. Furthermore, in the murine myeloid precursor 32D cell line, PA2G4 participates in the regulation of HDAC8 ubiquitination that is disrupted by the forced expression of the *Cbfb-MYH11* fusion, indicating a contribution of PA2G4 in MDM2-mediated HDAC8 ubiquitination in inv(16) leukemia [170].

Overall, we propose a clinical treatment strategy that capitalizes on the *EVI1*-suppressing capacity of some HDACis in patients carrying 3q26 abnormalities that lack biomarker-directed treatment approaches. Furthermore, based on the mechanism driving efficacy upon HDAC inhibition, our work positions PA2G4 as a druggable target for a neglected population with EVI1-expressing AML and potentially for other Myc-dependent cancers.

The information presented in this thesis has been previously published in the article: Marchesini M, Gherli A, **Simoncini E**, et al. Orthogonal proteogenomic analysis identifies the druggable PA2G4-MYC axis in 3q26 AML. Nat Commun. 2024;15(1):4739 [1].

5. Conclusions

Despite remarkable improvement in next-generation technologies, success in treating subtype of AML driven by dysregulated TFs are limited. The overexpression of the TF *EVI1* marks the most lethal AML subgroup carrying chromosome 3q26 abnormalities. While 3q26 AMLs have been identified as a distinct subgroup of AML, little has been done to improve their clinical outcome.

Here, we identify a druggable mediator of HDACis response in 3q26 AML and mechanistical demonstrated evidence of targeted suppression of EVI1 using phenotypic and genome-based analysis of the EVI1 chromatin complex in preciclinial-3q26-leukemia models and leukemia patients. In summary, our study highlights PA2G4 as a crucial mediator of the EVI1-Myc pathway in AML. We suggest that targeting PA2G4 could offer a new therapeutic approach for 3q26 AML and other Myc-driven cancers.

6. References

1. Marchesini, M., et al., *Orthogonal proteogenomic analysis identifies the druggable PA2G4-MYC axis in 3q26 AML.* Nat Commun, 2024. **15**(1): p. 4739.
2. Jacob, F. and J. Monod, *Genetic regulatory mechanisms in the synthesis of proteins.* J Mol Biol, 1961. **3**: p. 318-56.
3. Papavassiliou, A.G., *Molecular medicine. Transcription factors.* N Engl J Med, 1995. **332**(1): p. 45-7.
4. Lee, T.I. and R.A. Young, *Transcriptional regulation and its misregulation in disease.* Cell, 2013. **152**(6): p. 1237-51.
5. Konstantinopoulos, P.A. and A.G. Papavassiliou, *Seeing the future of cancer-associated transcription factor drug targets.* JAMA, 2011. **305**(22): p. 2349-50.
6. Yeh, J.E., P.A. Toniolo, and D.A. Frank, *Targeting transcription factors: promising new strategies for cancer therapy.* Curr Opin Oncol, 2013. **25**(6): p. 652-8.
7. Darnell, J.E., Jr., *Transcription factors as targets for cancer therapy.* Nat Rev Cancer, 2002. **2**(10): p. 740-9.
8. Vaquerizas, J.M., et al., *A census of human transcription factors: function, expression and evolution.* Nat Rev Genet, 2009. **10**(4): p. 252-63.
9. Papavassiliou, K.A. and A.G. Papavassiliou, *Transcription Factor Drug Targets.* J Cell Biochem, 2016. **117**(12): p. 2693-2696.
10. Zhang, Z., et al., *Genomic analysis of the nuclear receptor family: new insights into structure, regulation, and evolution from the rat genome.* Genome Res, 2004. **14**(4): p. 580-90.
11. Koehler, A.N., *A complex task? Direct modulation of transcription factors with small molecules.* Curr Opin Chem Biol, 2010. **14**(3): p. 331-40.
12. Schacke, H., et al., *Dissociation of transactivation from transrepression by a selective glucocorticoid receptor agonist leads to separation of therapeutic effects from side effects.* Proc Natl Acad Sci U S A, 2004. **101**(1): p. 227-32.
13. Tilley, W.D., et al., *Hormones and cancer: new insights, new challenges.* Trends Endocrinol Metab, 2001. **12**(5): p. 186-8.
14. Shi, Y., *Orphan nuclear receptors in drug discovery.* Drug Discov Today, 2007. **12**(11-12): p. 440-5.
15. Brivanlou, A.H. and J.E. Darnell, Jr., *Signal transduction and the control of gene expression.* Science, 2002. **295**(5556): p. 813-8.
16. Nesbit, C.E., J.M. Tersak, and E.V. Prochownik, *MYC oncogenes and human neoplastic disease.* Oncogene, 1999. **18**(19): p. 3004-16.
17. Cheng, Y., et al., *Rational drug design via intrinsically disordered protein.* Trends Biotechnol, 2006. **24**(10): p. 435-42.
18. Berg, T., et al., *Small-molecule antagonists of Myc/Max dimerization inhibit Myc-induced transformation of chicken embryo fibroblasts.* Proc Natl Acad Sci U S A, 2002. **99**(6): p. 3830-5.
19. Lu, X., et al., *Disruption of the MYC transcriptional function by a small-molecule antagonist of MYC/MAX dimerization.* Oncol Rep, 2008. **19**(3): p. 825-30.
20. Weng, A.P., et al., *Activating mutations of NOTCH1 in human T cell acute lymphoblastic leukemia.* Science, 2004. **306**(5694): p. 269-71.
21. Di Ianni, M., et al., *A new genetic lesion in B-CLL: a NOTCH1 PEST domain mutation.* Br J Haematol, 2009. **146**(6): p. 689-91.

22. Kridel, R., et al., *Whole transcriptome sequencing reveals recurrent NOTCH1 mutations in mantle cell lymphoma.* Blood, 2012. **119**(9): p. 1963-71.
23. Roti, G. and K. Stegmaier, *Targeting NOTCH1 in hematopoietic malignancy.* Crit Rev Oncog, 2011. **16**(1-2): p. 103-15.
24. Roti, G., et al., *Complementary genomic screens identify SERCA as a therapeutic target in NOTCH1 mutated cancer.* Cancer Cell, 2013. **23**(3): p. 390-405.
25. Cullion, K., et al., *Targeting the Notch1 and mTOR pathways in a mouse T-ALL model.* Blood, 2009. **113**(24): p. 6172-81.
26. Real, P.J., et al., *Gamma-secretase inhibitors reverse glucocorticoid resistance in T cell acute lymphoblastic leukemia.* Nat Med, 2009. **15**(1): p. 50-8.
27. Mitelman, F., B. Johansson, and F. Mertens, *The impact of translocations and gene fusions on cancer causation.* Nat Rev Cancer, 2007. **7**(4): p. 233-45.
28. Gery, S. and H.P. Koeffler, *Transcription factors in hematopoietic malignancies.* Curr Opin Genet Dev, 2007. **17**(1): p. 78-83.
29. Brien, G.L., K. Stegmaier, and S.A. Armstrong, *Targeting chromatin complexes in fusion protein-driven malignancies.* Nat Rev Cancer, 2019. **19**(5): p. 255-269.
30. Bushweller, J.H., *Targeting transcription factors in cancer - from undruggable to reality.* Nat Rev Cancer, 2019. **19**(11): p. 611-624.
31. Arkin, M.R., Y. Tang, and J.A. Wells, *Small-molecule inhibitors of protein-protein interactions: progressing toward the reality.* Chem Biol, 2014. **21**(9): p. 1102-14.
32. Illendula, A., et al., *Small Molecule Inhibitor of CBFbeta-RUNX Binding for RUNX Transcription Factor Driven Cancers.* EBioMedicine, 2016. **8**: p. 117-131.
33. Silvian, L.F., et al., *Small molecule inhibition of the TNF family cytokine CD40 ligand through a subunit fracture mechanism.* ACS Chem Biol, 2011. **6**(6): p. 636-47.
34. Tisato, V., et al., *MDM2/X inhibitors under clinical evaluation: perspectives for the management of hematological malignancies and pediatric cancer.* J Hematol Oncol, 2017. **10**(1): p. 133.
35. Helin, K. and D. Dhanak, *Chromatin proteins and modifications as drug targets.* Nature, 2013. **502**(7472): p. 480-8.
36. Gehling, V.S., et al., *Discovery, Design, and Optimization of Isoxazole Azepine BET Inhibitors.* ACS Med Chem Lett, 2013. **4**(9): p. 835-40.
37. Filippakopoulos, P., et al., *Selective inhibition of BET bromodomains.* Nature, 2010. **468**(7327): p. 1067-73.
38. Groschel, S., et al., *A single oncogenic enhancer rearrangement causes concomitant EVI1 and GATA2 deregulation in leukemia.* Cell, 2014. **157**(2): p. 369-381.
39. Roti, G. and K. Stegmaier, *Genetic and proteomic approaches to identify cancer drug targets.* Br J Cancer, 2012. **106**(2): p. 254-61.
40. Stegmaier, K., et al., *Gene expression-based high-throughput screening(GE-HTS) and application to leukemia differentiation.* Nat Genet, 2004. **36**(3): p. 257-63.
41. Peck, D., et al., *A method for high-throughput gene expression signature analysis.* Genome Biol, 2006. **7**(7): p. R61.
42. Hughes, T.R., et al., *Functional discovery via a compendium of expression profiles.* Cell, 2000. **102**(1): p. 109-26.
43. Stegmaier, K., et al., *Gefitinib induces myeloid differentiation of acute myeloid leukemia.* Blood, 2005. **106**(8): p. 2841-8.

44. Hahn, C.K., et al., *Proteomic and genetic approaches identify Syk as an AML target.* Cancer Cell, 2009. **16**(4): p. 281-94.
45. Banerji, V., et al., *The intersection of genetic and chemical genomic screens identifies GSK-3alpha as a target in human acute myeloid leukemia.* J Clin Invest, 2012. **122**(3): p. 935-47.
46. Antipova, A.A., B.R. Stockwell, and T.R. Golub, *Gene expression-based screening for inhibitors of PDGFR signaling.* Genome Biol, 2008. **9**(3): p. R47.
47. Corsello, S.M., et al., *Identification of AML1-ETO modulators by chemical genomics.* Blood, 2009. **113**(24): p. 6193-205.
48. Lamb, J., et al., *The Connectivity Map: using gene-expression signatures to connect small molecules, genes, and disease.* Science, 2006. **313**(5795): p. 1929-35.
49. Lamb, J., *The Connectivity Map: a new tool for biomedical research.* Nat Rev Cancer, 2007. **7**(1): p. 54-60.
50. Wei, G., et al., *Gene expression-based chemical genomics identifies rapamycin as a modulator of MCL1 and glucocorticoid resistance.* Cancer Cell, 2006. **10**(4): p. 331-42.
51. Dohner, H., D.J. Weisdorf, and C.D. Bloomfield, *Acute Myeloid Leukemia.* N Engl J Med, 2015. **373**(12): p. 1136-52.
52. Papaemmanuil, E., et al., *Genomic Classification and Prognosis in Acute Myeloid Leukemia.* N Engl J Med, 2016. **374**(23): p. 2209-2221.
53. Patel, J.P., et al., *Prognostic relevance of integrated genetic profiling in acute myeloid leukemia.* N Engl J Med, 2012. **366**(12): p. 1079-89.
54. Grimwade, D., et al., *Refinement of cytogenetic classification in acute myeloid leukemia: determination of prognostic significance of rare recurring chromosomal abnormalities among 5876 younger adult patients treated in the United Kingdom Medical Research Council trials.* Blood, 2010. **116**(3): p. 354-65.
55. De Braekeleer, M., et al., *3q26/EVI1 rearrangements in myeloid hemopathies: a cytogenetic review.* Future Oncol, 2015. **11**(11): p. 1675-86.
56. Lugthart, S., et al., *Clinical, molecular, and prognostic significance of WHO type inv(3)(q21q26.2)/t(3;3)(q21;q26.2) and various other 3q abnormalities in acute myeloid leukemia.* J Clin Oncol, 2010. **28**(24): p. 3890-8.
57. Groschel, S., et al., *High EVI1 expression predicts outcome in younger adult patients with acute myeloid leukemia and is associated with distinct cytogenetic abnormalities.* J Clin Oncol, 2010. **28**(12): p. 2101-7.
58. Buonamici, S., et al., *The role of EVI1 in normal and leukemic cells.* Blood Cells Mol Dis, 2003. **31**(2): p. 206-12.
59. Sun, J., et al., *De novo acute myeloid leukemia with inv(3)(q21q26.2) or t(3;3)(q21;q26.2): a clinicopathologic and cytogenetic study of an entity recently added to the WHO classification.* Mod Pathol, 2011. **24**(3): p. 384-9.
60. Sitges, M., et al., *Acute myeloid leukemia with inv(3)(q21.3q26.2)/t(3;3)(q21.3;q26.2): Study of 61 patients treated with intensive protocols.* Eur J Haematol, 2020. **105**(2): p. 138-147.
61. Rogers, H.J., et al., *Complex or monosomal karyotype and not blast percentage is associated with poor survival in acute myeloid leukemia and myelodysplastic syndrome patients with inv(3)(q21q26.2)/t(3;3)(q21;q26.2): a Bone Marrow Pathology Group study.* Haematologica, 2014. **99**(5): p. 821-9.

62. Groschel, S., et al., *Mutational spectrum of myeloid malignancies with inv(3)/t(3;3) reveals a predominant involvement of RAS/RTK signaling pathways.* Blood, 2015. **125**(1): p. 133-9.
63. Summerer, I., et al., *Prognosis of MECOM (EVI1)-rearranged MDS and AML patients rather depends on accompanying molecular mutations than on blast count.* Leuk Lymphoma, 2020. **61**(7): p. 1756-1759.
64. Lavallee, V.P., et al., *EVI1-rearranged acute myeloid leukemias are characterized by distinct molecular alterations.* Blood, 2015. **125**(1): p. 140-3.
65. Haferlach, C., et al., *The inv(3)(q21q26)/t(3;3)(q21;q26) is frequently accompanied by alterations of the RUNX1, KRAS and NRAS and NF1 genes and mediates adverse prognosis both in MDS and in AML: a study in 39 cases of MDS or AML.* Leukemia, 2011. **25**(5): p. 874-7.
66. Medeiros, B.C., et al., *Immunophenotypic features of acute myeloid leukemia with inv(3)(q21q26.2)/t(3;3)(q21;q26.2).* Leuk Res, 2010. **34**(5): p. 594-7.
67. Groschel, S., et al., *Deregulated expression of EVI1 defines a poor prognostic subset of MLL-rearranged acute myeloid leukemias: a study of the German-Austrian Acute Myeloid Leukemia Study Group and the Dutch-Belgian-Swiss HOVON/SAKK Cooperative Group.* J Clin Oncol, 2013. **31**(1): p. 95-103.
68. Ho, P.A., et al., *High EVI1 expression is associated with MLL rearrangements and predicts decreased survival in paediatric acute myeloid leukaemia: a report from the children's oncology group.* Br J Haematol, 2013. **162**(5): p. 670-7.
69. Hou, A., et al., *Expression of MECOM is associated with unfavorable prognosis in glioblastoma multiforme.* Onco Targets Ther, 2016. **9**: p. 315-20.
70. Xu, X., S. Liu, and X. Ji, *Overexpression of ecotropic viral integration site-1 is a prognostic factor of lung squamous cell cancer.* Onco Targets Ther, 2017. **10**: p. 2739-2744.
71. Brooks, D.J., et al., *Expression of the zinc finger gene EVI-1 in ovarian and other cancers.* Br J Cancer, 1996. **74**(10): p. 1518-25.
72. Liang, B. and J. Wang, *EVI1 in Leukemia and Solid Tumors.* Cancers (Basel), 2020. **12**(9).
73. Yamazaki, H., et al., *A remote GATA2 hematopoietic enhancer drives leukemogenesis in inv(3)(q21;q26) by activating EVI1 expression.* Cancer Cell, 2014. **25**(4): p. 415-27.
74. Ottema, S., et al., *The leukemic oncogene EVI1 hijacks a MYC super-enhancer by CTCF-facilitated loops.* Nat Commun, 2021. **12**(1): p. 5679.
75. Bahr, C., et al., *A Myc enhancer cluster regulates normal and leukaemic haematopoietic stem cell hierarchies.* Nature, 2018. **553**(7689): p. 515-520.
76. Mucenski, M.L., et al., *Identification of a common ecotropic viral integration site, Evi-1, in the DNA of AKXD murine myeloid tumors.* Mol Cell Biol, 1988. **8**(1): p. 301-8.
77. Morishita, K., et al., *The human Evi-1 gene is located on chromosome 3q24-q28 but is not rearranged in three cases of acute nonlymphocytic leukemias containing t(3;5)(q25;q34) translocations.* Oncogene Res, 1990. **5**(3): p. 221-31.
78. Fears, S., et al., *Intergenic splicing of MDS1 and EVI1 occurs in normal tissues as well as in myeloid leukemia and produces a new member of the PR domain family.* Proc Natl Acad Sci U S A, 1996. **93**(4): p. 1642-7.
79. Hinai, A.A. and P.J. Valk, *Review: Aberrant EVI1 expression in acute myeloid leukaemia.* Br J Haematol, 2016. **172**(6): p. 870-8.

80. Palmer, S., et al., *Evi-1 transforming and repressor activities are mediated by CtBP co-repressor proteins.* J Biol Chem, 2001. **276**(28): p. 25834-40.
81. Delwel, R., et al., *Four of the seven zinc fingers of the Evi-1 myeloid-transforming gene are required for sequence-specific binding to GA(C/T)AAGA(T/C)AAGATAA.* Mol Cell Biol, 1993. **13**(7): p. 4291-300.
82. Funabiki, T., B.L. Kreider, and J.N. Ihle, *The carboxyl domain of zinc fingers of the Evi-1 myeloid transforming gene binds a consensus sequence of GAAGATGAG.* Oncogene, 1994. **9**(6): p. 1575-81.
83. Bordereaux, D., et al., *Alternative splicing of the Evi-1 zinc finger gene generates mRNAs which differ by the number of zinc finger motifs.* Oncogene, 1990. **5**(6): p. 925-7.
84. Alzuherri, H., et al., *Conservation and expression of a novel alternatively spliced Evi1 exon.* Gene, 2006. **384**: p. 154-62.
85. Huang, S., G. Shao, and L. Liu, *The PR domain of the Rb-binding zinc finger protein RIZ1 is a protein binding interface and is related to the SET domain functioning in chromatin-mediated gene expression.* J Biol Chem, 1998. **273**(26): p. 15933-9.
86. Pinheiro, I., et al., *Prdm3 and Prdm16 are H3K9me1 methyltransferases required for mammalian heterochromatin integrity.* Cell, 2012. **150**(5): p. 948-60.
87. Perkins, A.S., et al., *Patterns of Evi-1 expression in embryonic and adult tissues suggest that Evi-1 plays an important regulatory role in mouse development.* Development, 1991. **111**(2): p. 479-87.
88. Hoyt, P.R., et al., *The Evi1 proto-oncogene is required at midgestation for neural, heart, and paraxial mesenchyme development.* Mech Dev, 1997. **65**(1-2): p. 55-70.
89. Wieser, R., *The oncogene and developmental regulator EVI1: expression, biochemical properties, and biological functions.* Gene, 2007. **396**(2): p. 346-57.
90. Aytekin, M., et al., *Regulation of the expression of the oncogene EVI1 through the use of alternative mRNA 5'-ends.* Gene, 2005. **356**: p. 160-8.
91. Goyama, S., et al., *Evi-1 is a critical regulator for hematopoietic stem cells and transformed leukemic cells.* Cell Stem Cell, 2008. **3**(2): p. 207-20.
92. Yuasa, H., et al., *Oncogenic transcription factor Evi1 regulates hematopoietic stem cell proliferation through GATA-2 expression.* EMBO J, 2005. **24**(11): p. 1976-87.
93. Yuan, X., et al., *The role of EVI-1 in normal hematopoiesis and myeloid malignancies (Review).* Int J Oncol, 2015. **47**(6): p. 2028-36.
94. Kreider, B.L., S.H. Orkin, and J.N. Ihle, *Loss of erythropoietin responsiveness in erythroid progenitors due to expression of the Evi-1 myeloid-transforming gene.* Proc Natl Acad Sci U S A, 1993. **90**(14): p. 6454-8.
95. Laricchia-Robbio, L., et al., *Point mutations in two EVI1 Zn fingers abolish EVI1-GATA1 interaction and allow erythroid differentiation of murine bone marrow cells.* Mol Cell Biol, 2006. **26**(20): p. 7658-66.
96. Morishita, K., et al., *Activation of EVI1 gene expression in human acute myelogenous leukemias by translocations spanning 300-400 kilobases on chromosome band 3q26.* Proc Natl Acad Sci U S A, 1992. **89**(9): p. 3937-41.
97. Senyuk, V., et al., *Repression of RUNX1 activity by EVI1: a new role of EVI1 in leukemogenesis.* Cancer Res, 2007. **67**(12): p. 5658-66.

98. Laricchia-Robbio, L., et al., *EVI1 Impairs myelopoiesis by deregulation of PU.1 function.* Cancer Res, 2009. **69**(4): p. 1633-42.
99. Paredes, R., et al., *EVI1 protein interaction dynamics: Targetable for therapeutic intervention?* Exp Hematol, 2022. **107**: p. 1-8.
100. Chakraborty, S., et al., *Interaction of EVI1 with cAMP-responsive element-binding protein-binding protein (CBP) and p300/CBP-associated factor (P/CAF) results in reversible acetylation of EVI1 and in co-localization in nuclear speckles.* J Biol Chem, 2001. **276**(48): p. 44936-43.
101. Izutsu, K., et al., *The corepressor CtBP interacts with Evi-1 to repress transforming growth factor beta signaling.* Blood, 2001. **97**(9): p. 2815-22.
102. Glass, C., et al., *Global Identification of EVI1 Target Genes in Acute Myeloid Leukemia.* PLoS One, 2013. **8**(6): p. e67134.
103. Shimabe, M., et al., *Pbx1 is a downstream target of Evi-1 in hematopoietic stem/progenitors and leukemic cells.* Oncogene, 2009. **28**(49): p. 4364-74.
104. Yoshimi, A., et al., *Evi1 represses PTEN expression and activates PI3K/AKT/mTOR via interactions with polycomb proteins.* Blood, 2011. **117**(13): p. 3617-28.
105. Kustikova, O.S., et al., *Activation of Evi1 inhibits cell cycle progression and differentiation of hematopoietic progenitor cells.* Leukemia, 2013. **27**(5): p. 1127-38.
106. Matsumoto, A., et al., *p57 is required for quiescence and maintenance of adult hematopoietic stem cells.* Cell Stem Cell, 2011. **9**(3): p. 262-71.
107. Kurokawa, M., et al., *The evi-1 oncoprotein inhibits c-Jun N-terminal kinase and prevents stress-induced cell death.* EMBO J, 2000. **19**(12): p. 2958-68.
108. Pradhan, A.K., et al., *Acetylation of the proto-oncogene EVI1 abrogates Bcl-xL promoter binding and induces apoptosis.* PLoS One, 2011. **6**(9): p. e25370.
109. Maicas, M., et al., *Functional characterization of the promoter region of the human EVI1 gene in acute myeloid leukemia: RUNX1 and ELK1 directly regulate its transcription.* Oncogene, 2013. **32**(16): p. 2069-78.
110. Lux, S. and M.D. Milsom, *EVI1-mediated Programming of Normal and Malignant Hematopoiesis.* Hemasphere, 2023. **7**(10): p. e959.
111. Loven, J., et al., *Selective inhibition of tumor oncogenes by disruption of super-enhancers.* Cell, 2013. **153**(2): p. 320-34.
112. Bradner, J.E., D. Hnisz, and R.A. Young, *Transcriptional Addiction in Cancer.* Cell, 2017. **168**(4): p. 629-643.
113. Birdwell, C., et al., *EVI1 dysregulation: impact on biology and therapy of myeloid malignancies.* Blood Cancer J, 2021. **11**(3): p. 64.
114. Raisner, R., et al., *Enhancer Activity Requires CBP/P300 Bromodomain-Dependent Histone H3K27 Acetylation.* Cell Rep, 2018. **24**(7): p. 1722-1729.
115. Kiehlmeier, S., et al., *Identification of therapeutic targets of the hijacked super-enhancer complex in EVI1-rearranged leukemia.* Leukemia, 2021. **35**(11): p. 3127-3138.
116. Saha, H.R., et al., *Suppression of GPR56 expression by pyrrole-imidazole polyamide represents a novel therapeutic drug for AML with high EVI1 expression.* Sci Rep, 2018. **8**(1): p. 13741.
117. Saito, Y., et al., *Maintenance of the hematopoietic stem cell pool in bone marrow niches by EVI1-regulated GPR56.* Leukemia, 2013. **27**(8): p. 1637-49.

118. Grasedieck, S., et al., *The retinoic acid receptor co-factor NRIP1 is uniquely upregulated and represents a therapeutic target in acute myeloid leukemia with chromosome 3q rearrangements.* Haematologica, 2022. **107**(8): p. 1758-1772.
119. Fenouille, N., et al., *The creatine kinase pathway is a metabolic vulnerability in EVI1-positive acute myeloid leukemia.* Nat Med, 2017. **23**(3): p. 301-313.
120. Benajiba, L., et al., *Creatine kinase pathway inhibition alters GSK3 and WNT signaling in EVI1-positive AML.* Leukemia, 2019. **33**(3): p. 800-804.
121. Schmoellerl, J., et al., *EVI1 drives leukemogenesis through aberrant ERG activation.* Blood, 2023. **141**(5): p. 453-466.
122. Masamoto, Y., et al., *EVI1 exerts distinct roles in AML via ERG and cyclin D1 promoting a chemoresistant and immune-suppressive environment.* Blood Adv, 2023. **7**(8): p. 1577-1593.
123. Chi, H.T., et al., *Detection of exon 12 type A mutation of NPM1 gene in IMS-M2 cell line.* Leuk Res, 2010. **34**(2): p. 261-2.
124. Twarog, N.R., et al., *BRAID: A Unifying Paradigm for the Analysis of Combined Drug Action.* Sci Rep, 2016. **6**: p. 25523.
125. Subramanian, A., et al., *A Next Generation Connectivity Map: L1000 Platform and the First 1,000,000 Profiles.* Cell, 2017. **171**(6): p. 1437-1452 e17.
126. Pilarczyk, M., et al., *Connecting omics signatures and revealing biological mechanisms with iLINCS.* Nat Commun, 2022. **13**(1): p. 4678.
127. Efron, B., *Bootstrap Methods: Another Look at the Jackknife.* Breakthroughs in statistics: Methodology and distribution., 1992. **Vol. II**: p. 569-593.
128. Bankhead, P., et al., *QuPath: Open source software for digital pathology image analysis.* Sci Rep, 2017. **7**(1): p. 16878.
129. Ewels, P.A., et al., *The nf-core framework for community-curated bioinformatics pipelines.* Nat Biotechnol, 2020. **38**(3): p. 276-278.
130. Zhang, Y., et al., *Model-based analysis of ChIP-Seq (MACS).* Genome Biol, 2008. **9**(9): p. R137.
131. Heinz, S., et al., *Simple combinations of lineage-determining transcription factors prime cis-regulatory elements required for macrophage and B cell identities.* Mol Cell, 2010. **38**(4): p. 576-89.
132. Robinson, J.T., et al., *Integrative genomics viewer.* Nat Biotechnol, 2011. **29**(1): p. 24-6.
133. Satija, R., et al., *Spatial reconstruction of single-cell gene expression data.* Nat Biotechnol, 2015. **33**(5): p. 495-502.
134. Hao, Y., et al., *Integrated analysis of multimodal single-cell data.* Cell, 2021. **184**(13): p. 3573-3587 e29.
135. Vazquez, I., et al., *Down-regulation of EVI1 is associated with epigenetic alterations and good prognosis in patients with acute myeloid leukemia.* Haematologica, 2011. **96**(10): p. 1448-56.
136. Wang, Z., et al., *L1000FWD: fireworks visualization of drug-induced transcriptomic signatures.* Bioinformatics, 2018. **34**(12): p. 2150-2152.
137. Lee, H.Z., et al., *FDA Approval: Belinostat for the Treatment of Patients with Relapsed or Refractory Peripheral T-cell Lymphoma.* Clin Cancer Res, 2015. **21**(12): p. 2666-70.
138. Prebet, T., et al., *Prolonged administration of azacitidine with or without entinostat for myelodysplastic syndrome and acute myeloid leukemia with myelodysplasia-related changes: results of the US Leukemia Intergroup trial E1905.* J Clin Oncol, 2014. **32**(12): p. 1242-8.

139. Liverani, C., et al., *Lineage-specific mechanisms and drivers of breast cancer chemoresistance revealed by 3D biomimetic culture.* Mol Oncol, 2022. **16**(4): p. 921-939.
140. Konrad, T.A., et al., *Inducible expression of EVI1 in human myeloid cells causes phenotypes consistent with its role in myelodysplastic syndromes.* J Leukoc Biol, 2009. **86**(4): p. 813-22.
141. Prebet, T., et al., *Azacitidine with or without Entinostat for the treatment of therapy-related myeloid neoplasm: further results of the E1905 North American Leukemia Intergroup study.* Br J Haematol, 2016. **172**(3): p. 384-91.
142. Wang, J., et al., *Phase I Study and Pilot Efficacy Analysis of Entinostat, a Novel Histone Deacetylase Inhibitor, in Chinese Postmenopausal Women with Hormone Receptor-Positive Metastatic Breast Cancer.* Target Oncol, 2021. **16**(5): p. 591-599.
143. Barbie, D.A., et al., *Systematic RNA interference reveals that oncogenic KRAS-driven cancers require TBK1.* Nature, 2009. **462**(7269): p. 108-12.
144. Tyner, J.W., et al., *Functional genomic landscape of acute myeloid leukaemia.* Nature, 2018. **562**(7728): p. 526-531.
145. San Jose-Eneriz, E., et al., *HDAC Inhibitors in Acute Myeloid Leukemia.* Cancers (Basel), 2019. **11**(11).
146. Andreatta, M. and S.J. Carmona, *UCell: Robust and scalable single-cell gene signature scoring.* Comput Struct Biotechnol J, 2021. **19**: p. 3796-3798.
147. Pei, Y., et al., *HDAC and PI3K Antagonists Cooperate to Inhibit Growth of MYC-Driven Medulloblastoma.* Cancer Cell, 2016. **29**(3): p. 311-323.
148. Winkler, R., et al., *Targeting the MYC interaction network in B-cell lymphoma via histone deacetylase 6 inhibition.* Oncogene, 2022. **41**(40): p. 4560-4572.
149. Topper, M.J., et al., *Epigenetic Therapy Ties MYC Depletion to Reversing Immune Evasion and Treating Lung Cancer.* Cell, 2017. **171**(6): p. 1284-1300 e21.
150. Mohammed, H., et al., *Rapid immunoprecipitation mass spectrometry of endogenous proteins (RIME) for analysis of chromatin complexes.* Nat Protoc, 2016. **11**(2): p. 316-26.
151. Bard-Chapeau, E.A., et al., *EVI1 oncoprotein interacts with a large and complex network of proteins and integrates signals through protein phosphorylation.* Proc Natl Acad Sci U S A, 2013. **110**(31): p. E2885-94.
152. Squatrito, M., et al., *EBP1 is a nucleolar growth-regulating protein that is part of pre-ribosomal ribonucleoprotein complexes.* Oncogene, 2004. **23**(25): p. 4454-65.
153. Liu, Z., et al., *Ebp1 isoforms distinctively regulate cell survival and differentiation.* Proc Natl Acad Sci U S A, 2006. **103**(29): p. 10917-22.
154. Ko, H.R., et al., *Roles of ErbB3-binding protein 1 (EBP1) in embryonic development and gene-silencing control.* Proc Natl Acad Sci U S A, 2019. **116**(49): p. 24852-24860.
155. Koach, J., et al., *Drugging MYCN Oncogenic Signaling through the MYCN-PA2G4 Binding Interface.* Cancer Res, 2019. **79**(21): p. 5652-5667.
156. Wouters, B.J., et al., *Double CEBPA mutations, but not single CEBPA mutations, define a subgroup of acute myeloid leukemia with a distinctive gene expression profile that is uniquely associated with a favorable outcome.* Blood, 2009. **113**(13): p. 3088-91.

157. Vadakekolathu, J., et al., *Immune landscapes predict chemotherapy resistance and immunotherapy response in acute myeloid leukemia.* Sci Transl Med, 2020. **12**(546).
158. Shen, W., et al., *Small-molecule inducer of beta cell proliferation identified by high-throughput screening.* J Am Chem Soc, 2013. **135**(5): p. 1669-72.
159. Kohl, N.E., et al., *Human N-myc is closely related in organization and nucleotide sequence to c-myc.* Nature, 1986. **319**(6048): p. 73-7.
160. Kim, E.S., *Midostaurin: First Global Approval.* Drugs, 2017. **77**(11): p. 1251-1259.
161. Dhillon, S., *Gilteritinib: First Global Approval.* Drugs, 2019. **79**(3): p. 331-339.
162. Yamaura, T., et al., *A novel irreversible FLT3 inhibitor, FF-10101, shows excellent efficacy against AML cells with FLT3 mutations.* Blood, 2018. **131**(4): p. 426-438.
163. Dombret, H., et al., *International phase 3 study of azacitidine vs conventional care regimens in older patients with newly diagnosed AML with >30% blasts.* Blood, 2015. **126**(3): p. 291-9.
164. Stein, E.M., et al., *Molecular remission and response patterns in patients with mutant-IDH2 acute myeloid leukemia treated with enasidenib.* Blood, 2019. **133**(7): p. 676-687.
165. Stone, R.M., *Consolidation chemotherapy for adults with AML in first remission: is there a best choice?* J Clin Oncol, 2013. **31**(17): p. 2067-9.
166. Ravandi, F., J. Cortes, and H. Kantarjian, *Is there a standard induction regimen for patients with AML?* Lancet Oncol, 2013. **14**(7): p. 565-6.
167. Rashidi, A., et al., *Maintenance therapy in acute myeloid leukemia: an evidence-based review of randomized trials.* Blood, 2016. **128**(6): p. 763-73.
168. Reiter, E., et al., *Low curative potential of bone marrow transplantation for highly aggressive acute myelogenous leukemia with inversioin inv (3)(q21q26) or homologous translocation t(3;3) (q21;q26).* Ann Hematol, 2000. **79**(7): p. 374-7.
169. Halaburda, K., et al., *AlloHSCT for inv(3)(q21;q26)/t(3;3)(q21;q26) AML: a report from the acute leukemia working party of the European society for blood and marrow transplantation.* Bone Marrow Transplant, 2018. **53**(6): p. 683-691.
170. Zhang, L., et al., *Targeting miR-126 in inv(16) acute myeloid leukemia inhibits leukemia development and leukemia stem cell maintenance.* Nat Commun, 2021. **12**(1): p. 6154.
171. Perkins, A.S. and J.H. Kim, *Zinc fingers 1-7 of EVI1 fail to bind to the GATA motif by itself but require the core site GACAAGATA for binding.* J Biol Chem, 1996. **271**(2): p. 1104-10.
172. Zhang, Y., et al., *Targeting a DNA binding motif of the EVI1 protein by a pyrrole-imidazole polyamide.* Biochemistry, 2011. **50**(48): p. 10431-41.
173. Morice, P.M., et al., *Myelodysplastic syndrome and acute myeloid leukaemia in patients treated with PARP inhibitors: a safety meta-analysis of randomised controlled trials and a retrospective study of the WHO pharmacovigilance database.* Lancet Haematol, 2021. **8**(2): p. e122-e134.
174. Vinatzer, U., et al., *The leukaemia-associated transcription factors EVI-1 and MDS1/EVI1 repress transcription and interact with histone deacetylase.* Br J Haematol, 2001. **114**(3): p. 566-73.
175. Senyuk, V., et al., *The leukemia-associated transcription repressor AML1/MDS1/EVI1 requires CtBP to induce abnormal growth and differentiation of murine hematopoietic cells.* Oncogene, 2002. **21**(20): p. 3232-40.

176. Gabay, M., Y. Li, and D.W. Felsher, *MYC activation is a hallmark of cancer initiation and maintenance.* Cold Spring Harb Perspect Med, 2014. **4**(6).
177. Yun, S., et al., *Prognostic significance of MYC oncoprotein expression on survival outcome in patients with acute myeloid leukemia with myelodysplasia related changes (AML-MRC).* Leuk Res, 2019. **84**: p. 106194.
178. Ohanian, M., et al., *MYC protein expression is an important prognostic factor in acute myeloid leukemia.* Leuk Lymphoma, 2019. **60**(1): p. 37-48.
179. Mughal, M.K., et al., *Acute myeloid leukaemia: expression of MYC protein and its association with cytogenetic risk profile and overall survival.* Hematol Oncol, 2017. **35**(3): p. 350-356.
180. Bard-Chapeau, E.A., et al., *Ecotopic viral integration site 1 (EVI1) regulates multiple cellular processes important for cancer and is a synergistic partner for FOS protein in invasive tumors.* Proc Natl Acad Sci U S A, 2012. **109**(6): p. 2168-73.
181. Yatsula, B., et al., *Identification of binding sites of EVI1 in mammalian cells.* J Biol Chem, 2005. **280**(35): p. 30712-22.
182. Stevenson, B.W., et al., *A structural view of PA2G4 isoforms with opposing functions in cancer.* J Biol Chem, 2020. **295**(47): p. 16100-16112.
183. Ko, H.R., et al., *Opposing roles of the two isoforms of ErbB3 binding protein 1 in human cancer cells.* Int J Cancer, 2016. **139**(6): p. 1202-8.
184. Kim, C.K., et al., *Negative regulation of p53 by the long isoform of ErbB3 binding protein Ebp1 in brain tumors.* Cancer Res, 2010. **70**(23): p. 9730-41.
185. Kim, C.K., et al., *Long isoform of ErbB3 binding protein, p48, mediates protein kinase B/Akt-dependent HDM2 stabilization and nuclear localization.* Exp Cell Res, 2012. **318**(2): p. 136-43.
186. Hwang, I., H.R. Ko, and J.Y. Ahn, *The roles of multifunctional protein ErbB3 binding protein 1 (EBP1) isoforms from development to disease.* Exp Mol Med, 2020. **52**(7): p. 1039-1047.
187. Wang, Y., et al., *Distinct Interactions of EBP1 Isoforms with FBXW7 Elicits Different Functions in Cancer.* Cancer Res, 2017. **77**(8): p. 1983-1996.
188. Nguyen le, X.T., et al., *Expression and Role of the ErbB3-Binding Protein 1 in Acute Myelogenous Leukemic Cells.* Clin Cancer Res, 2016. **22**(13): p. 3320-7.
189. Tang, Y., et al., *Induced lineage promiscuity undermines the efficiency of all-trans-retinoid-acid-induced differentiation of acute myeloid leukemia.* iScience, 2021. **24**(5): p. 102410.
190. Subramanian, A., et al., *A Next Generation Connectivity Map: L1000 Platform and the First 1,000,000 Profiles.* Cell, 2017. **171**(6): p. 1437-1452.e17.
191. Subramanian, A., et al., *Gene set enrichment analysis: a knowledge-based approach for interpreting genome-wide expression profiles.* Proceedings of the National Academy of Sciences, 2005. **102**(43): p. 15545-15550.

7. Figure Legends

Figure 1: Small molecule screening identifies *EVI1* modulators.

A. Identification of *EVI1* "*Off*" modulators by the integration of phenotypic and *in silico* gene-expression-based screen approaches.
B. Circos plot summarizing primary small molecule screening in EVI1^{High} AML cell lines. The heatmap at the external circle shows the normalized percentage of cell death (∆POC) for the 95th percentile for the compounds tested. The middle circos shows the compound libraries: i) Spectrum Collection (n=1914); ii) the anti-cancer compound library (n=343); and iii) the NDL-3000 library (n=3035). The inner plot shows a hierarchical cluster of top candidates' scalar fingerprints (SMILE), based on the Tanimoto similarity metric.
C. Histogram showing the distribution of percentage over control (POC) values for the Selleck anticancer (dark blue), MicroSource Spectrum (dark turquoise), and TimTec Natural Derivative (cyan) compounds. The effect on viability was normalized to vehicle control (DMSO) and plotted on the x axis. The y axis indicates the number of small molecules with values falling in the POC intervals.
D. POC effect in MOLM1 and UCSD/AML1 3q26 AML cell lines. The line in the box-and-whisker plot represents the median centered ratio. The box's upper edge (hinge) indicates the 75th percentile of the data, and the lower hinge represents the 25th percentile. The whiskers represent the minimum and maximum data values. All small molecule libraries were tested in duplicates ± standard deviation (SD). Statistical significance was determined by a two-sided non-parametric t-test (Mann-Whitney).
E. Box-and-whisker plot showing POC's effect in MOLM1 (M) and UCSD/AML1 (U) AML cell lines by row plates. All small-molecules libraries were tested in n=2 biological replicates.
F. Dot plot showing the effects of the compound tested (n = 5292), ranked based on ∆POC. The yellow area indicates the 95th percentile. HDAC inhibitors (HDACis) are labeled in red.
G. Heatmap showing the effect AUC of 40 hit compounds. Columns represent AML cell lines, and rows represent small molecules. The color code indicates the

range of relative effects for a given molecule. Unsupervised clustering was computed by calculating Pearson correlation coefficients.

Figure 2: Genome-based approaches identify HDACis as *EVI1* modulators.

A. Volcano plot derived from TF1 cells gene expression data (Affymetrix microarray profiling from E-GEOD 16238 [135]) after treatment with an *EVI1*-directed siRNA (*EVI1* siRNA n=3) or non-targeting control (Control n=3). DEGs are depicted in dark yellow if upregulated in *EVI1* siRNA (SNR $\geq$ 1.5, *Adj.P* $\leq$ 0.01) or in violet if upregulated in Control (SNR $\leq$ - 1.5 or, *Adj.P* $\leq$ 0.01).
B. Rank-score log-scale plots for HDACis (n = 32), histamine (n = 52), glucocorticoid (n = 47), and acetylcholine receptor antagonists (n = 66). In black, the number of perturbagenes inferred in the connectivity map of which 2836 are small molecules. Compounds of interest are color-coded and expressed as a percentage relative to the entire library.
C. Bar plot showing the HDACis (in red) ranking in the ConnectivityMap [190] dataset. The tau score represents the level of similarity to the *EVI1* "*On"* or "*Off*" status.
D. Average *P* value (x axis) for molecules of interest (MOIs; y axis) computed by Wilcoxon rank-sum test by comparing 10,000 random drug sets against MOIs and performing 100 iterations.
E. Violin plots comparing ΔPOC activity between HDACis and the indicated drug classes. "n" indicates the number of small molecules within each class (HDACi n=29, histamine receptor antagonist n=19, glucocorticoid receptor antagonists n=31, acetylcholine receptor antagonists n=32, antineoplastic agents n=49). Statistical significance among groups was determined by one-way ANOVA (C) using Tukey's correction for multiple comparison testing.
F. Volcano plot derived from RNASeq gene expression data of HNT34 cells transduced with a non-targeting shRNA (Control, n=3) or after *EVI1*-directed shRNAs (sh#16, n=3 and sh#87, n=3) three days after selection. DEGs are depicted in violet if upregulated in Control ($\log_2$ fold change $\leq$ - 2, *Adj.P* $\leq$ 0.05) or in dark yellow if upregulated in *EVI1* shRNA ($\log_2$ fold change $\geq$ 2, *Adj.P* $\leq$ 0.05).

G. GSEA analysis of Affymetrix data from **Figure 2F** using the oncogenic gene sets from HNT34 transduced with shRNAs targeting *EVI1*. Enrichment plot of the *EVI1* overlapping genes is shown. GSEA enrichment score significance was based on a weighted Kolmogorov Smirnov (WKS) test corrected for multiple hypotheses testing: Benjamini & Hochberg (BH or FDR) [191]. NES, normalized enrichment score; FDR, false discovery rate.

H. Volcano plot of RNASeq expression in $EVI1^{High}$ (n=5) or $EVI1^{Low}$ (n=2) AML cell lines segregated based on the 3q26 status derived from the E-MTAB-2225 dataset [38]. From DEGs upregulated genes in $EVI1^{High}$ (n=8247) and upregulated in $EVI1^{Low}$ (n=7699) are depicted those with $\log_2$ fold change $\leq$ - 2 (n=118, violet) and with a $\log_2$ fold change $\geq$ 2 (n=144, dark yellow).

I. L1000FWD fireworks visualization of drug-induced signatures mimicking and reversing the differential gene expression signature generated from *EVI1*-silenced HNT34 and (left) and from $EVI1^{High}$ (n=5) or $EVI1^{Low}$ (n=2) AML cell lines contained in the E-MTAB-2225 dataset (right). Aquamarine circles indicate small molecules causing a reverse signature *EVI1* "*Off*". Light violet circles indicate small molecules mimicking a signature *EVI1* "*On*". HDACis drug-induced signatures are indicated in green overlapping with aquamarine circles.

J. Bar plot displaying top drugs inducing an *EVI1* "*Off*" status identified by the $L1000CDS^2$ query of HNT34 (from **Figure 2I**, left) and E-MTAB-2225 (**Figure 2I**, right) datasets. HDAC inhibitors are highlighted in green.

Figure 3: Effect of *EVI1* loss in 3q26 AML cell lines.

A. EVI1 and ΔEVI1 expression in $EVI1^{High}$ AML cell lines (n=3 biological replicates).

B. Nuclear localization expression of EVI1 (in red) detected by immunofluorescence (IF) in $EVI1^{High}$ AML cell lines (n=3 biological replicates per cell line). Cell nuclei were stained with DAPI (blue), scale bar: 10 μm.

C. EVI1 and ΔEVI1 expression in TF1, UCSD/AML1, HNT34 cells 6 days after shRNA transduction.

D. Percentage of *EVI1* mRNA relative to the control gene *RPL13A* (ΔΔCT) in TF1, UCSD/AML1, HNT34 cells 6 days after shRNA transduction.

E. Effect of *EVI1* loss in TF1, UCSD/AML1, HNT34 cells at three or six days after shRNA selection on cell proliferation.

F. Effect of shRNA-directed *EVI1* loss in the ability of TF1 (left panel) and UCSD/AML1 (right panel) to form colonies in methylcellulose compared to NT (n=2 biological replicates). Scale bar: 1000 μm. The histogram on the right shows the mean number of colonies per field 20 days after plating cells. NT = non-targeting, sh#16 and sh#87 = shRNA directed against *EVI1* (C, D, E, F).

Statistical significance among groups was determined by one-way (D upper and lower panel, F left panel) or two-way (E) ANOVA using Tukey's correction for multiple comparison testing; two-sided non-parametric t-test (Mann-Whitney) (D middle panel, F right panel). Data are presented as mean ± standard deviation (SD) in D (n=3 upper and lower panel, n=4 middle panel), E (n=4), F (n=10 fields per condition).

Figure 4: Effect of HDACis in 3q26 AML cell lines.

A. Effect of AR-42, belinostat, and entinostat on cell viability in $EVI1^{High}$ cell lines following 72 hours (hr) of treatment.

B. Annexin V/propidium iodide (PI) staining after 72 hr of HDACis treatment in MOLM1, UCSD/AML1, HNT34 and MUTZ-3. Events ≥ 20,000.

C. Apoptotic fold increase, expressed as a percentage of annexin V-positive cells relative to vehicle control.

D. Effect of HDACis on the ability of 3q26 AML cell lines to form colonies in methylcellulose. Representative images of UCSD/AML1 treated with vehicle (DMSO), 0.5 μM AR-42, 0.5 μM belinostat, and 0.5 μM entinostat (n=3 biological replicates). Scale bar: 1000 μm.

E. The histogram shows the mean number of colonies per field 20 days after plating cells.

Statistical significance among groups was determined by one-way (E) ANOVA using Tukey's correction for multiple comparison testing. Data are presented as mean ± standard deviation (SD) in A (n=2), and E (n=10 fields per condition).

Figure 5: HDACis modulate *EVI1* in 3q26 AML.

A. EVI1, ΔEVI1, and cleaved caspase 3 expression in 3q26 EVI1^{High} cell lines after 24 hr of treatment with DMSO or HDACis (n=2 biological replicates).
B. Representative IF images of EVI1 (red) in 3q26 EVI1^{High} cell lines (left, n=3 biological replicates per cell line). Cell nuclei were stained with DAPI (blue), scale bar: 100 μm. Right: fluorescence intensity of nuclear EVI1 content in 3q26 EVI1^{High} AML cell lines after 24 hr of treatment.
C. Percentage of *EVI1* mRNA relative to the control gene *RPL13A* (ΔΔCT) in EVI1^{High} AML cell lines.
D. Top panel: representative images of collagen type I scaffolds (n=3 imaged scaffolds). Scale bar: 500 μm. Bottom panel: scanning electron microscope (SEM) scaffold micrograph showing the collagen fibers' architecture and the biological matrix's porosity. Scale bar: 100 μm.
E. Hematoxylin-and-eosin–stained (H&E) histological sections of EVI1^{High} 3q26 AML cell line grown in collagen type I scaffolds for 7 days (n=3 imaged scaffolds per cell line). Insets show niche-like structures. Scale bar: 100 μm.
F. Expression of EVI1 in 3q26 AML cell lines in 3D models. Left: representative immunohistochemical staining (IHC) for EVI1 (brownish) in HNT34 cells and hematoxylin-and-eosin staining (H&E) for the collagen matrix (n=3 imaged scaffolds). Scale bar: 50 μm. Right: immunofluorescence images of MOLM1 grown for 7 days in 3D collagen type 1 scaffold incubated with anti-EVI1 (in red) (n=2 imaged scaffolds). Nuclei were stained with DAPI (blue) and the collagen matrix was detected by autofluorescence (green). Scale bar: 20 μm.
G. Histograms showing proliferation fold increase based on MTT absorbance relative to day 0 in EVI1^{High} MOLM1 and HNT34 cells grown in collagen type I scaffolds.
H. AUC effect of ara-C, AR-42, belinostat, and entinostat in EVI1^{High} MOLM1 (top) and HNT34 (bottom) grown in standard 2D or 3D collagen type I scaffold cell culture. Cell viability was assessed after 72 hr using the same concentration in 2D or 3D cell cultures.

   Statistical significance was determined by one-way (B, C) ANOVA with Tukey's correction for multiple comparison testing. Data are presented as mean ± SD in

B (UCSD/AML1 n=828, MOLM1 n=1028, HNT34 n=571), C (n=3), G (n=3), H (n=2).

Figure 6: EVI1 sensitized AML to HDACis.

A. IF images of U937T_E10 cells cultured in the presence ($EVI1^{Low}$, top panel) or absence ($EVI1^{High}$, bottom panel) of tetracycline, incubated with an anti-EVI1 (red) antibody (n=2 biological replicates). Nuclei in blue (DAPI). Scale bar: 100 µm.
B. EVI1 and ΔEVI1 expression in U937T_E10 cells in the presence or absence of tetracycline (n=3 biological replicates).
C. Effect of EVI1 expression on cell proliferation in U937T_E10 in the presence ($EVI1^{Low}$) or absence of tetracycline ($EVI1^{High}$). Histograms show the ATP absorbance fold increase relative to vehicle control.
D. Effect of HDACis, ara-C, methotrexate, vincristine and daunorubicine on cell viability after 72 hr of treatment in U937T_E10 cell cultured in the presence ($EVI1^{Low}$, black line) or absence ($EVI1^{High}$, red line) of tetracycline.
E. Representative IF showing HL-60 cells transduced with an empty (top panels) or an ORF-*EVI1* cDNA (bottom panels) vector and stained with an anti-EVI1 antibody (in red, n=2 biological replicates). Nuclei in blue (DAPI). Scale bar: 100 µm.
F. Western blot analysis showing HL-60 AML cell line transduced with an empty vector or an ORF-*EVI1* cDNA plasmid (n=2 biological replicates).
G. Effect of HDACis and ara-C on cell viability after 72 hr of treatment in HL-60 ± ORF-*EVI1* cDNA.
H. Abnormal 3q26 pattern on fluorescence in situ hybridization (FISH) in MOLM1 sorted by cell size. The break-apart hybridization pattern 1F1G1O (one fusion and two separated signals, one green and one orange) indicates the break and split of the *EVI1* locus. The abnormal pattern was observed in cells with large nuclei. At least 100 nuclei/cells were analyzed (n=2 biological replicates). Scale bar: 20 µm.
I. Expression of EVI1 in MOLM1 sorted based on cell size. Large cells express EVI1 compared to small cells.

J. Effects of HDACis and chemotherapy treatment on viability in MOLM1 EVI1^{High} and MOLM1 EVI1^{Low} after 72 hr of drug exposure.

K. Effect of AR-42, belinostat, entinostat, ara-C, vincristine, methotrexate, and daunorubicin on EVI1^{High} (MOLM1, UCSD/AML1, HNT34, TF1, and MUTZ-3) and EVI1^{Low} (NOMO1, MOLM13, OCI/AML1, OCI/AML2, GDM1, SKM1, and IMS-M2) AML cell lines calculated using the area under the curve (AUC) model of the log-transformed dose-response data. A lower AUC corresponds to greater sensitivity.

Statistical significance among groups was determined by two-way (C) ANOVA using Tukey's correction for multiple comparison testing or two-tailed non-parametric t-test (Mann-Whitney) (J). Data are presented as mean ± SD in C (n=14), D (n=2), G (n=2), J (n=2), K (EVI1^{High} n=5, EVI1^{Low} n=7).

Figure 7: Genomic, genetic, and clinical characteristics of 3q26 AML cases enrolled in this study.

A. Representative abnormal 3q26 pattern on fluorescence in situ hybridization (FISH) in PR#001-005 and PR#007-009. The break-apart hybridization pattern 1F1G1O (one fusion and two separated signals, one green and one orange) indicates the break and split of the *EVI1* locus. The abnormal pattern was observed in 100% of blasts analyzed for PR#001, 95% for PR#003 and PR#004, 90% for PR#009, 89% for PR#002, 80% for PR#008, 73% for PR#005, and 30% for PR#006 and PR#007, and 97% for PR#023, 80% for PR#024 (n=100 nuclei/patients were analyzed). FISH representative images were not available for PR#006, PR#023 and for PR#024. Scale bar: 100 μm.

B. Oncoprint plot showing somatic mutations in recurrent mutated genes (n=30) in AML. Left, AML cases carrying 3q26 abnormalities (n=11, PR#001-009 and PR#023-024); right, other AML subtypes (n=28, PR#010-022 and PR#025-039). Single nucleotide variations (SNVs, in red) or insertions/deletions (INDELs, in yellow) of sequenced genes are listed on the left of the plots. Histograms show the event frequency of SNVs or INDELs detected in each sample (on the top) or for each gene in the cohort (right, percentage of mutation is also indicated).

No mutations were detected for *BRAF, CALR*, *CSFR3R*, *HRAS*, and *MPL* genes in our cohort. NGS data were not available for PR#011 and PR#016.

Figure 8: Effect of HDACis in primary AML cells.

A. H&E histological sections of PR#003 bone marrow cells grown in collagen type I scaffolds with vehicle (DMSO) or HDACis (AR-42, belinostat, and entinostat) for 72 hr. Scale bar: 40 μm.
B. Percentage of cell viability of primary 3q26 AML grown in collagen type I scaffolds and treated with HDACis. Scale bar: 100 μm. Drug concentration (IC_{50}) used in (A) and (B) were established following a dose-response titration assay presented in C**.**
C. Effect of AR-42, belinostat, and entinostat on cell viability after 72 hr of treatment in available 3q26 AML cells, as assessed by an ATP-based luminescence viability assay. Error bars denote ± standard deviation (SD) of two replicates.
D. AUC effect of HDACis and chemotherapy agents in $EVI1^{High}$ (samples PR#002-008, and PR#023-024) and $EVI1^{Low}$ (samples PR#010-022, and PR#025-039) AML blasts.
E. EVI1, ΔEVI1, and cleaved caspase 3 protein expression of primary 3q26 AML samples after 24 hr of treatment with the indicated concentrations of HDACis.
F. Representative images of IF staining of primary 3q26 $EVI1^{High}$ AML cell showing EVI1 nuclear content (in red) following 24 hr of treatment with DMSO or HDACis at the indicated concentrations. Nuclei in blue (DAPI), scale bar: 100 μm.
G. Quantitative IF analysis of nuclear EVI1 content in 3q26 $EVI1^{High}$ primary AML cells after 24 hr of treatment with indicated compounds.
H. Western blot analysis showing EVI1, ΔEVI1, and cleaved caspase 3 expression in PR#004 after 24 hr of treatment with the indicated concentrations of HDACis and ara-C. HNT34 cells were loaded as a positive control.

Statistical significance was determined by a two-tailed non-parametric t-test (Mann-Whitney) (D) or one-way ANOVA with Tukey's correction for multiple comparison testing (B, G). Data are presented as mean ± SD in B (PR#003 n=3, PR#004 n=2), D ($EVI1^{High}$ n=9, $EVI1^{Low}$ n=28), G (PR#002 n=318, PR#003 n=573).

Figure 9: Effect of HDACis in 3q26 AML patients and in 3q26 AML PDLX.

A. Extra-hematologic toxicity of HDACi-based therapy in patients with 3q26 AML. Mean concentrations of aspartate aminotransferase (GOT), bilirubin, alanine aminotransferase (GPT), lactate dehydrogenase (LDH), gamma-glutamyl transferase (GGT), alkaline phosphatase (ALP), and creatinine in PR#002 during four cycles of azacitidine at 50 mg/m^2 and entinostat at 4 mg/m^2.
B. Cell blood count of PR#001 receiving azacitidine 50 mg/m^2 every (day 1-10) and entinostat 4 mg/m^2 on days 3 and 10 every 28 days. The timeline at the top indicates cycles of therapy (blue triangle), transfusion units of red blood cells ([RBCs] red boxes), and platelets ([PLTs] yellow boxes) over time. Cell blood count of white blood cells (WBCs) and polymorphonuclear leukocytes (PMNs) in the middle. The bottom panel shows the blood concentration of PLT and hemoglobin (Hb).
C. Effect of entinostat (left) or ara-C (right) on EVI1 nuclear localization (in red) following 6 hr of treatment in PR#003 or PR#004, respectively. The nuclei were stained with DAPI (blue). Scale bar: 100 µm. IF quantification of EVI1 nuclear content is presented at the bottom.
D. Effect of entinostat (10 mg/kg) on EVI1 nuclear localization (in red) following 6 hr of treatment in PDLX_PR#003 (n=3 biological replicates) and PDLX_PR#009 (n=3 biological replicates). The nuclei were stained with DAPI (blue). Scale bar: 100 µm. Histograms indicate the quantitative immunofluorescence analysis of EVI1 nuclear content before and after therapy. Scatter dot plots indicate the mean ± SD of fluorescence intensity for each nucleus analyzed and expressed as arbitrary units. Statistical significance was determined by a two-sided non-parametric t-test (Mann-Whitney).
E. EVI1 expression (brownish) in bone marrow leukemia cells at diagnosis and following two cycles of azacitidine and entinostat (PR#002, left) or three cycles of ara-C and daunorubicin (3+7) (PR#004, right). Top, formalin-fixed, paraffin-embedded (FFPE) tissue sections were stained with anti-EVI1 antibody revealed by immunoperoxidase. Scale bar: 100 µm.

   Statistical significance was determined by a two-tailed non-parametric t-test (Mann-Whitney) (C, E) or a two-sided non-parametric t-test (Mann-Whitney) (D)

or one-way (A), ANOVA using Tukey's correction for multiple comparison testing. Data are presented as mean ± SD in A (n=41 GOT, n=41 GPT, n=37 GGT, n=29 ALP, n=38 bilirubin, n=33 LDH, n=37 creatinine), C (PR#003 n=235, PR#004 n=214), D (n=103 PDLX_PR#003, n=128 PDLX_PR#009) and E (n=10 fields per condition).

Figure 10: HDAC-mediated suppression of EVI1 modulates Myc signaling.

A. Volcano plot of RNASeq expression following 16 hr of 0.5 µM AR-42, 2 µM entinostat in UCSD/AML1 or 0.8 µM AR-42, and 4 µM entinostat in MOLM1. DEGs are depicted in blue if repressed ($\log_2$ fold change $\leq$ - 2, *Adj.P* $\leq$ 0.05) or in red if upregulated ($\log_2$ fold change $\geq$ + 2, *Adj.P* $\leq$ 0.05).
B. Heatmap showing ssGSEA enrichment of MSigDB of gene signature in MOLM1 and UCSD/AML1 HDACi-treated cells. Hot or cold colors indicate correlation or anticorrelation of the top enriched gene sets from each functional group ($P \leq$ 0.05 in bold, calculated according to [143]) among cell lines and treatments (bottom).
C. Heatmap showing ssGSEA enrichment of Elsevier, KEGG and BioPlanet of gene signature in MOLM1 and UCSD/AML1 HDACi-treated cells. Hot or cold colors indicate correlation or anticorrelation of the top enriched gene sets from each functional group (in bold, $P \leq 0.05$) among cell lines and treatments (bottom).
D. Uniform manifold approximation and projection (UMAP) plot of clustering results of PR#002 bone marrow cells before and after therapy. Colors indicate the cell populations on the basis of the reference mapping approach.
E. UMAP plot of PR#002 scRNASeq data, colored according to therapy status.
F. UMAP plot of clustering results of PR#002 bone marrow cells before (left) and after (right) therapy, colored according to the UCell score of leukemic markers.
G. Dot plot illustrating gene expression (log of averaged counts) across the 17 cell clusters in the PR#002 scRNASeq data set. Genes defining the leukemia immunophenotype at diagnosis are included. The size of the dots represents the proportion of gene-expressing cells, and the color intensity represents the average level of gene expression.

H. GSEA running score plot of the top enriched *MYC targets V1 pathway* in HSC, LMPP, and LP (*Adj.P* = 0.0011) cell populations of PR#002. Each graph indicates the running enrichment score (ES) of the pathway (top), the location of single genes of the gene set in the ranking (central), and the distribution of the ranking metric (bottom).

I. Dot plots of GSEA results illustrating Molecular Signatures Database (MsigDB) biological processes associated with EVI1 downregulation in HSC, LMPP, and LP in PR#002. Gene count refers to the number of genes associated with each (MsigDB) biological process. On the basis of co-expressed genes, the figures show the significant top positively and negatively enriched (MsigDB) terms. Gene ratio (x axis) is the percentage of genes significantly correlated with EVI1 downregulation from the total number of genes associated with that process. Terms are ranked in the figure by decreasing gene ratio. Dot size is proportional to the number of matched genes within each pathway, while the color indicates the *Adj.P* for each pathway. GSEA enrichment score significance was based on a weighted Kolmogorov Smirnov (WKS) test corrected for multiple hypotheses testing: Benjamini & Hochberg (BH or FDR) [191].

J. MYC expression (brownish) in bone marrow leukemia cells of PR#002 at diagnosis and following two cycles of azacitidine and entinostat (left). Scale bar: 100 μm. Right, the scatter dot blot indicates the mean ± SD of the percentage of the MYC-positive cells in FFPE tissue sections (n=10 fields per condition).

K. EVI1, ΔEVI1, and MYC expression in EVI1^{High} AML cell lines, 6 days after shRNA transduction. NT = non-targeting, sh#87 = shRNA directed against *EVI1* (n=3 biological replicates).

L. MYC expression following 24 hr of HDACis treatment in PR#006 bone marrow cells with the indicated concentrations of HDACis and ara-C.

M. MYC expression following 24 hr of HDACis treatment in the 3q26 AML cell lines (n=2 biological replicates).

N. On the left tracks showing EVI1 binding and H3K27ac enrichment across the *MYC* locus in HNT34 cells treated with DMSO, AR-42 and entinostat. The bottom bar represents the genes (hg19), and the y-axis represents normalized read density scaled to 1 million. On the right real-time PCR after ChIP performed in HNT34 cells treated with DMSO, AR-42 and entinostat at the indicated doses

using an anti-EVI1 and H3K27Ac antibody and primers targeting the *MYC* promoter. Results are expressed as fold enrichment of *EVI1* and *H3K27Ac* compared to a non-specific IgG antibody. Statistical significance) was determined by ordinary one-way ANOVA using Tukey's correction for multiple comparison testing. Data are presented as mean ± SD (n=3).

Statistical significance was determined by a two-tailed non-parametric t-test (Mann-Whitney) (J). GSEA enrichment score significance was based on a weighted Kolmogorov Smirnov (WKS) test corrected for multiple hypotheses testing: Benjamini & Hochberg (BH or FDR) (H). Data are presented as mean ± SD in J (n=10 fields per condition).

Figure 11: EVI1 modulates MYC in 3q26 AML preclinical model.

A. *In vivo* antileukemic effect of entinostat and azacitidine. Mice (PDLX_PR#008) were treated with vehicle (DMSO), azacitidine (1mg/kg) for 5 days, entinostat (10mg/kg) (5 days/week) or the combination of both for 3 weeks. Histograms show the percentage $hCD45^{+}$ in bone marrow (top) and the percentage of *EVI1* mRNA relative to the control gene *RPL13A* (ΔΔCT) in CD45+ cells (bottom) at the end of treatment.
B. UMAP plot of clustering results of PDLX_PR#008 bone marrow LP before (i) and after entinostat (ii), azacytidine (iii) or the combination of both (iv), colored according to the UCell score of leukemic markers.
C. GSEA running score plot of the top enriched *MYC targets V1 pathway* in PDLX_PR#008 LP after the treatment with azacitidine/entinostat (*Adj.P* = 3.40×10^{-8}) or entinostat as single agent (*Adj.P* = 2.17×10^{-12}). Each graph indicates the running enrichment score (ES) of the pathway (top), the location of single genes of the gene set in the ranking (central), and the distribution of the ranking metric (bottom).
D. Dot plot illustrating gene expression (log of averaged counts) across the 17 cell clusters in the PDLX_PR#003 scRNASeq data set. Genes defining the leukemia immunophenotype at diagnosis are included. The size of the dots represents the proportion of gene-expressing cells, and the color intensity represents the average level of gene expression.

E. Dot plot of GSEA results illustrating Molecular Signatures Database (MsigDB) biological processes associated with the indicated treatments compared to the vehicle in PDLX_PR#008 LP. Set size refers to the number of genes associated with each (MsigDB) biological process. Dot color indicates the range of *Adj.P* for each pathway.

F. EVI1, MYC, and Ki67 expression (brownish) in bone marrow leukemia cells (PDLX_PR#008) following three weeks treatment of azacitidine and entinostat as described in panel G. FFPE tissue were stained with anti-EVI1, anti-MYC and anti-Ki67 antibodies revealed by immunoperoxidase. Scale bar: 100 µm.

G. Histograms display the mean ±SD of the percentage of the EVI1, MYC or Ki67-positive cells in FFPE tissue sections.

Statistical significance was determined by one-way ANOVA with Tukey's correction for multiple comparison testing (A, G). GSEA enrichment score significance was based on a weighted Kolmogorov Smirnov (WKS) test corrected for multiple hypotheses testing: Benjamini & Hochberg (BH or FDR) (C, E). Data are presented as mean ± SD in A (vehicle n=7, treated n=5 per group; n=9 for the bottom panel), E (vehicle n=7, treated n=5 per group), G (n=10 fields per condition).

Figure 12: MYC overexpression does not sensitize cells to HDAC inhibition in 3q26 AML models.

A. EVI1, ΔEVI1, MYC and MYCN expression level in a panel of $EVI1^{High}$ (left) and $EVI1^{Low}$ (right) AML cell lines. β-Actin was used as loading control (n=3 biological replicates).

B. Effect of AR-42, belinostat and entinostat on MYC^{High} (OCI/AML2, OCI/AML3, IMS-M2, GDM1, NOMO1 and TF1) and MYC^{Low} (SKM1, MOLM13, MOLM1, UCSD/AML1, HNT34 and MUTZ-3) AML cell lines. The AUC model of the log-transformed dose-response data is depicted.

C. EVI1, ΔEVI1 and MYC expression level HNT34, U937T (clone E10) +/- tetracycline and *MYC* overexpressing U937T cells. β -Actin was used as loading control (n=3 biological replicates).

D. Effects of AR-42, belinostat, and entinostat on viability in U937T +/- tetracycline and *MYC* overexpressing U937T cell lines following 72h of drug treatment at the indicated concentrations.
E. Effect of JQ-1 on $EVI1^{High}$ (MOLM1, UCSD/AML1, HNT34, TF1 and MUTZ-3) and $EVI1^{Low}$ (NOMO1, MOLM13, OCI/AML2, OCI/AML3, GDM1, SKM1 and IMS-M2) AML cell lines calculated using the area under the curve (AUC) model of the log-transformed dose-response data.
F. Effect of JQ-1 on MYC^{High} (OCI/AML2, OCI/AML3 IMS-M2, GDM1, NOMO1 and TF1) and MYC^{Low} (SKM1, MOLM13, MOLM1, UCSD/AML1, HNT34 and MUTZ-3) AML cell lines. The AUC model of the log-transformed dose-response data is depicted.

Statistical significance among groups was determined by a two-sided non-parametric t-test (Mann-Whitney) (B, E, F). Data are presented as mean ± SD in B (MYC^{High} =6, MYC^{Low}=6), D (n=2), E ($EVI1^{High}$=5, $EVI1^{Low}$=7), F (MYC^{High}=6, MYC^{Low}=6).

Figure 13: Identification of PA2G4 as a mediator of Evi1/Myc signaling in 3q26 AML.

A. Circle plot showing chromatin-associated proteins immunoprecipitated with an anti-EVI1 antibody by RIME. The bar length indicates the mean of mass spectrometry spectral count (SPEC) of uniquely identified proteins of two biological replicates per condition. Bar colors indicate protein ontology of the EVI1 interactors.
B. Abnormal 3q26 pattern on fluorescence in situ hybridization (FISH) in PR#003 cells grown subcutaneously in NSG mice. The break-apart hybridization pattern 1F1G1O (one fusion and two separated signals, one green and one orange) indicates the break and the split of the *MECOM* locus. Scale bar: 10 µm.
C. Expression of EVI1 (brownish) in PR#003 and PDLX_PR#003. Formalin-fixed, paraffin-embedded (FFPE) tissue sections (top = bone marrow; bottom = subcutaneous xenotransplant) were stained with an anti-EVI1 antibody revealed by immunoperoxidase. Scale bar: 100 µm.

D. Venn diagram showing the number of chromatin-associated proteins immunoprecipitated with an anti-EVI1 antibody by RIME HNT34 (n = 156), UCSD/AML1 (n = 108), and PR#003 (n = 118). Sixty-nine proteins were common to all samples.

E. Bubble plot showing the intersection of ssGSEA enrichment of the Molecular Signatures Database (MSigDB), Elsevier, Kyoto Encyclopedia of Genes and Genomes (KEGG), and BioPlanet and RIME of 3q26 AML cells. The x axis represents the area under the curve (AUC) and the y axis the normalized mutual information ([NMI] y axis), calculated on the basis of ssGSEA. An NMI = 1 indicates an *EVI1* "*On*" status, and NMI = -1 indicates an *EVI1* "*Off*" status. The bubble size indicates the number of genes in each pathway per dataset, and the color scale indicates the level of statistical significance (t-*P*). The inner red dots show EVI1 interactors, identified by RIME, that are common in the genes contained in each pathway. Their size represents the number of EVI1-interacting proteins.

F. Volcano plot displaying the enrichment of proteins in 3q26 AML samples (n=6) compared con control samples (n=6) identified by label free quantitation (LFQ). Statistical significance was performed with a two-sample t-test and with a permutation-based correction controlled with an FDR threshold of 0.05. Significant hits with a fold change > 4 and a $P < 0.01$ are depicted in yellow. In the left panel, blue-labeled proteins are MYC-pathway related proteins derived from the intersection of RIME and ssGSEA analysis as detailed in the manuscript. In the right panel, red-labeled proteins are EVI1 interactors previously identified using isotope labeling based MS.

G. Histograms show the normalized gene expression levels of *SERBP1*, *RPL14*, *RPL18*, *RPS2*, *PA2G4*, *RPS10*, *FBL*, *PABPC1*, *RACK1*, *RSL1D1*, and *DDX21* following 16 hr of 0.5 μM AR-42, 2 μM entinostat in UCSD/AML1, or 0.8 μM AR-42 and 4 μM entinostat in MOLM1 compared to vehicle. Statistical significance was determined using DESeq2. Whiskers show median values (central black lines) and 25th and 75th percentiles (bottom and top bounds) respectively. The bars represent values that exceed 1.5 times the interquartile range (IQR) from the edge of each box: (vehicle n=6, treated n=12).

H. Tracks showing EVI1 binding and H3K27ac enrichment across the *DDX21, FBL, and PA2G4* locus in HNT34 cells treated with vehicle (DMSO), AR-42 and entinostat. The bottom bar represents the genes (hg19), and the y-axis represents normalized read density scaled to 1 million.

Figure 14: PA2G4 mediates the effect of HDACis on EVI1 and MYC.

A. PA2G4 and EVI1 nuclear co-localization in 3q26 AML cell lines. Orthogonal views of x/y, x/z, and y/z planes from a representative z-stack image of HNT34 cells. EVI1 is labeled in red and PA2G4 in green; the cell nucleus was stained with DAPI (blue). Scale bars correspond to 20 μm. The dot plots on the right indicate the mean ± SD of the coefficient indexes of Pearson derived from the co-localization signal in HNT34, UCSD/AML1, and MOLM1 (n=5 nuclei/cell line).
B. Co-immunoprecipitation of EVI1 and PA2G4 in HNT34 (top) and HEK-293T (bottom). HEK-293T were co-transfected with expression plasmid for *EVI1* and *PA2G4* (n=3 biological replicates).
C. Percentage of *PA2G4* mRNA relative to the control gene *RPL13A* (ΔΔCT) in MOLM1 and UCSD/AML1 following HDACis treatment.
D. Heat map showing the Spearman correlation coefficient of the pairwise comparison between genes in the indicated datasets, calculated on the basis of mas5 normalized data (GSE14468) or FPKM (GSE134589) of each gene.
E. Chromatin immunoprecipitation assay on HNT34 treated with vehicle (DMSO) or 2 μM WS6 for 24 hr using an anti-EVI1, MYC, and H3K27Ac antibody. Real-time PCR primers target the E-Box DNA binding sites in the *PA2G4* gene promoter, 500 bp upstream of the transcription starting site region. Results are expressed as fold enrichment of *EVI1*, *MYC*, or *H3K27Ac* compared to a non-specific IgG antibody.
F. PA2G4, EVI1, ∆EVI1, and MYC expression in TF1, HNT34, and UCSD/AML1 cells 6 days after shRNA transduction (n=3 biological replicates).
G. Effect of *PA2G4* loss in UCSD/AML1 cells at three, six, or nine days after shRNA selection. NT = non-targeting, sh#65-68 = shRNAs directed against *PA2G4*.

H. Effect of *PA2G4* loss in the ability of UCSD/AML1 to form colonies in methylcellulose. shRNAs directed against *PA2G4* inhibited colony formation compared to control (NT = non-targeting). Scale bar: 1000 μm. The histogram on the right shows the mean number of colonies per field 20 days after replating cells. Experiments were performed in n=2 biological replicates and plated in technical duplicates.

I. Effect of *PA2G4* overexpression on HNT34 cells treated with HDACis. Western blot analysis showing PA2G4, EVI1, ΔEVI1, and MYC in wild-type or *PA2G4*-overexpressing HNT34 cells after 24 hr of treatment with HDACis at the indicated doses (n=2 biological replicates).

J. Histogram indicates the percentage of viable (white), dead (black), or rescued (red) HNT34 cells by the overexpression of *PA2G4* on the basis of positivity for annexin V/PI staining after 72 hr of HDACis treatment (n=2 biological replicates). Statistical significance among wild-type or *PA2G4*-overexpressing HNT34 cells was determined by two-sided Fisher's exact test ($n \geq 20.000$).

K. Percentage of *PA2G4*, *EVI1*, and *MYC* mRNA relative to the control gene *ACTB* (ΔΔCT) in HNT34 and UCSD/AML1 cells 6 days after shRNA transduction. Data are presented as mean ± SD (n=3). Statistical significance was determined by a two-tailed unpaired, parametric t-test.

L. Proteasome inhibition rescues WS6-induced EVI1 and MYC protein degradation. EVI1, ΔEVI1, MYC expression, and PA2G4 in HNT34 and UCSD/AML1 cell lines after treatment with DMSO and WS6 (24 hr) or MG132 (4 hr) at the indicated concentrations (n=2 biological replicates).

Statistical significance among groups was determined by one (C, H) or two-way ANOVA (E, G) using Tukey's correction for multiple comparison testing respectively. Data are presented as mean ± SD C (n=3), G (n=5) in H (n=40 measurements for each condition), in E (n=3).

NT = non-targeting, sh#65 = shRNA directed against *PA2G4,* sh#66 = shRNA directed against *PA2G4*, sh#68 = shRNA directed against *PA2G4* in F-H, K.

Figure 15: Chemical inhibition of PA2G4 abrogates the Evi1/Myc signaling axis *in vitro.*

A. Effects of WS6 treatment on viability in primary 3q26 AML samples following 72 hr of drug treatment.
B. Effect of WS6 in EVI1^{High} (samples PR#002 - 006, PR#008 and PR#023 - 024) and EVI1^{Low} (samples PR#025-039) primary AML samples. The AUC model of the log-transformed dose-response data is depicted.
C. Effects of WS6 treatment compared to control (DMSO) on viability in primary 3q26 AML samples following 72 hr of drug treatment. Left: H&E of PR#005 bone marrow cells in 3D cell culture after 72 hr of treatment with vehicle (DMSO) or WS6 at 1/2 IC_{50} and IC_{50} concentrations. Scale bar: 40 µm. Right: histograms indicate the fraction of viable cells expressed as a percentage relative to control.
D. Effects of WS6 treatment on viability in 3q26 AML cell lines following 72 hr drug treatment. Data are presented as mean ± SD (n=2).
E. BRAID index analysis [124] for the combinations of WS6 with HDACis (AR-42, belinostat and entinostat) in n=2 EVI1^{High} (samples PR#024 and PDLX#PR008) and n=3 EVI1^{Low} (samples PR#034, PR#031 and PR#039) primary AML samples treated for 72h. A color scale bar represents the level of drug antagonism or synergism. K index is indicated. A positive K index indicates a synergistic effect.
F. Acetylated tubulin (Ac-Tubulin) and H3K27Ac expression in 3q26 EVI1^{High} AML cell lines after 24 hr of treatment with the indicated concentrations of HDACis and WS6 (n=2 biological replicates).
G. PA2G4, EVI1, ∆EVI1, and MYC and cleaved caspase 3 protein expression in primary 3q26 AML samples following 24 hr of treatment with the vehicle (DMSO) or WS6 at the indicated concentrations.
H. PA2G4, EVI1, ∆EVI1, MYC, and cleaved caspase 3 expression in 3q26 EVI1^{High} AML cell lines after 24 hr of treatment with DMSO or WS6 (n=2 biological replicates).

Statistical significance was determined by a two-tailed non-parametric t-test (Mann-Whitney) (B,). Data are presented as mean ± SD in A (n=2), B (EVI1^{High} n=8, EVI1^{Low} n=15), C (n=2).

Figure 16: Ws6 alters 3q26 AML proliferation *in vivo*.

A. Effect of WS6 (50 mg/kg) on EVI1 nuclear localization (in red) following 6 hr of treatment in PDLX_PR#009 (n=3 biological replicates). Nuclei in blue (DAPI). Scale bar: 100 μm. Histograms indicate the fluorescence intensity of EVI1 nuclear content before and after treatment.
B. *In vivo* antileukemic effect of WS6. On the top the draft of the experiments. Mice were treated with vehicle (DMSO) or 25 mg/Kg WS6 for 5 days/week for 15 days. On the bottom-left dot plot showing the number of hCD45+ cells expressed as the percentage difference of BM leukemic cells at T1 (endpoint-day 15) vs. T0 (pre-treatment-day 0) normalized for T0 in control (n=7) and WS6-treated PDLX_PR#003 (n=6). On the bottom-right the dot plot shows the percentage of hCD45+ cells in the bone marrow between vehicle (n=4) or WS6 treated PDLX_PR#008 (n=5) at the endpoint. Events ≥ 20.000.
C. Representative May Grünwald Giemsa staining of bone marrow blood cells collected from PDLX_PR#008 mice treated with DMSO (on the top) or 25 mg/Kg WS6 for 5 days/week for a total of 15 days (on the bottom). Representative n=2 mice per group are shown. Scale bar: 20 μm.
D. UMAP plot of clustering results of PDLX_PR#003 hCD45 bone marrow–positive cells before (left panel) and after (right panel) 15 days of WS6 treatment (25 mg/kg/IP/5 days a week), color-coded according to the UCell score of leukemic markers (MECOM, MYC, CD45, CD34, KIT, CD33, ANPEP, CD38, CD2, TFRC, HLA-DRA, HLA-DRB1, and HLA-DRB5).
E. Dot plot illustrating gene expression (log of averaged counts) in the n=17 cell clusters derived from scRNASeq of BM $CD45^{+}$-sorted AML cells (PDLX_PR#003). Genes defying the leukemia immunophenotype at diagnosis were included. The size of the dots represents the proportion of gene-expressing cells, and the color intensity of the dots represents the average level of gene expression.
F. WS6 depletes EVI1 and MYC proteins *in vivo*. EVI1, ΔEVI1, and MYC protein expression in PDLX_PR#008 mice treated with vehicle (DMSO) or 25 mg/Kg WS6 5 days/week for a total of 15 days. Representative n=3 mice per group are shown. Ponceau staining was used as loading control.

G. EVI1, MYC, and Ki67 expression in PDLX_PR#003 after 15 days of WS6 treatment (25 mg/kg/IP/5 days a week) or vehicle (DMSO). Scale bar: 100 µm. Histograms to the right indicate the mean ± SD of the percentage of the EVI1, MYC, or Ki67-positive cells in FFPE tissue sections.

Statistical significance was determined by a two-tailed non-parametric t-test (Mann-Whitney) (A, B, G). Data are presented as mean ± SD in H (vehicle n=7, treated n=6; n=10 fields per condition).

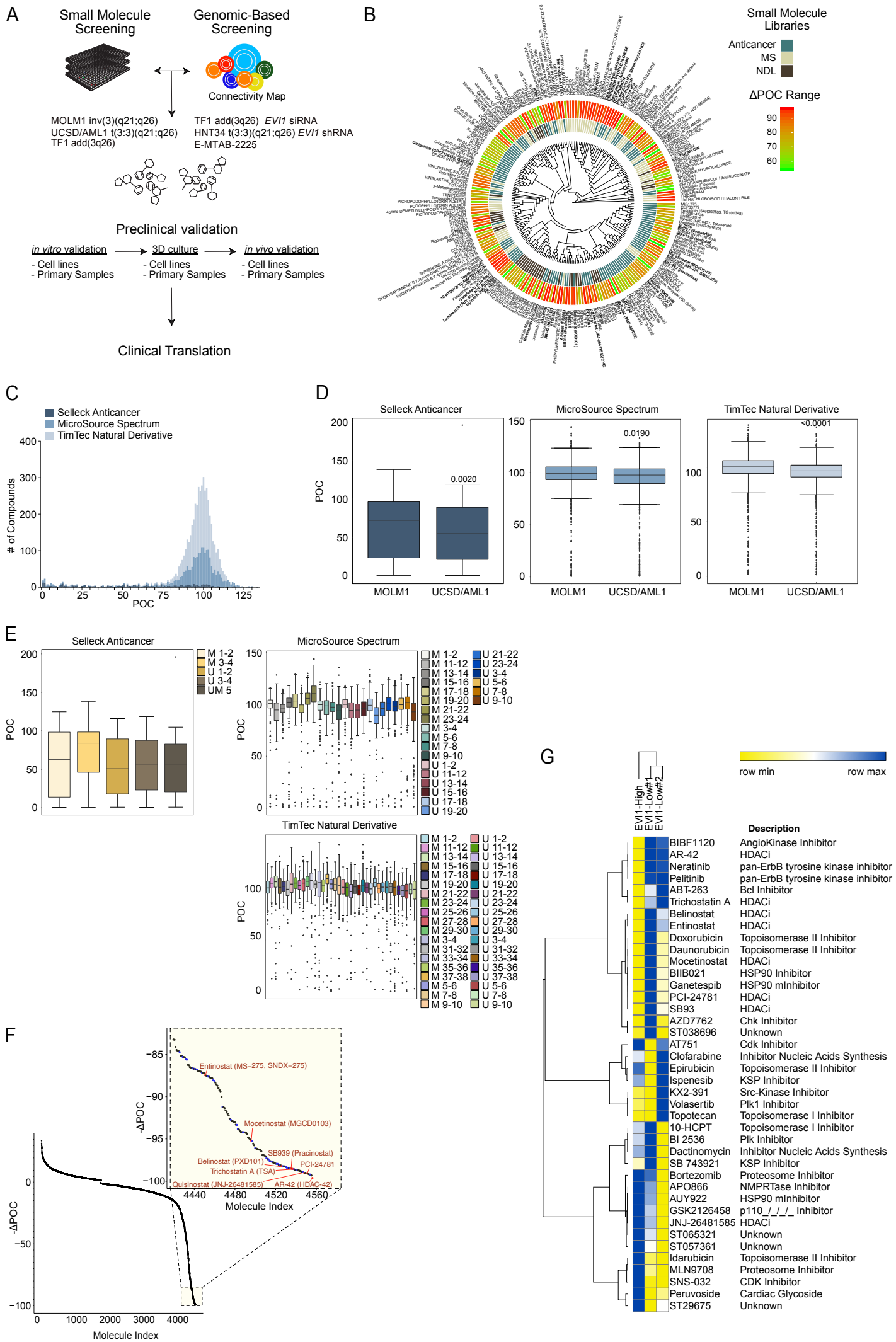
A
Small Molecule Screening
Genomic-Based Screening
Connectivity Map
MOLM1 inv(3)(q21;q26)
UCSD/AML1 t(3:3)(q21;q26)
TF1 add(3q26)
TF1 add(3q26) EVI1 siRNA
HNT34 t(3:3)(q21;q26) EVI1 shRNA
E-MTAB-2225
Preclinical validation
in vitro validation
- Cell lines
- Primary Samples
3D culture
- Cell lines
- Primary Samples
in vivo validation
- Cell lines
- Primary Samples
Clinical Translation
B
Small Molecule Libraries
Anticancer
MS
NDL
ΔPOC Range
90
80
70
60
C
Selleck Anticancer
MicroSource Spectrum
TimTec Natural Derivative
# of Compounds
POC
D
Selleck Anticancer
MicroSource Spectrum
TimTec Natural Derivative
POC
0.0020
0.0190
<0.0001
MOLM1
UCSD/AML1
E
Selleck Anticancer
MicroSource Spectrum
TimTec Natural Derivative
POC
M 1-2
M 3-4
U 1-2
U 3-4
UM 5
F
Entinostat (MS−275, SNDX−275)
Mocetinostat (MGCD0103)
SB939 (Pracinostat)
PCI-24781
Belinostat (PXD101)
Trichostatin A (TSA)
Quisinostat (JNJ-26481585)
AR-42 (HDAC-42)
-ΔPOC
Molecule Index
G
EVI1-High
EVI1-Low#1
EVI1-Low#2
row min
row max
Description
BIBF1120 AngioKinase Inhibitor
AR-42 HDACi
Neratinib pan-ErbB tyrosine kinase inhibitor
Pelitinib pan-ErbB tyrosine kinase inhibitor
ABT-263 Bcl Inhibitor
Trichostatin A HDACi
Belinostat HDACi
Entinostat HDACi
Doxorubicin Topoisomerase II Inhibitor
Daunorubicin Topoisomerase II Inhibitor
Mocetinostat HDACi
BIIB021 HSP90 Inhibitor
Ganetespib HSP90 mInhibitor
PCI-24781 HDACi
SB93 HDACi
AZD7762 Chk Inhibitor
ST038696 Unknown
AT751 Cdk Inhibitor
Clofarabine Inhibitor Nucleic Acids Synthesis
Epirubicin Topoisomerase II Inhibitor
Ispenesib KSP Inhibitor
KX2-391 Src-Kinase Inhibitor
Volasertib Plk1 Inhibitor
Topotecan Topoisomerase I Inhibitor
10-HCPT Topoisomerase I Inhibitor
BI 2536 Plk Inhibitor
Dactinomycin Inhibitor Nucleic Acids Synthesis
SB 743921 KSP Inhibitor
Bortezomib Proteosome Inhibitor
APO866 NMPRTase Inhibitor
AUY922 HSP90 mInhibitor
GSK2126458 p110_/_/_/_ Inhibitor
JNJ-26481585 HDACi
ST065321 Unknown
ST057361 Unknown
Idarubicin Topoisomerase II Inhibitor
MLN9708 Proteosome Inhibitor
SNS-032 CDK Inhibitor
Peruvoside Cardiac Glycoside
ST29675 Unknown

Figure 1

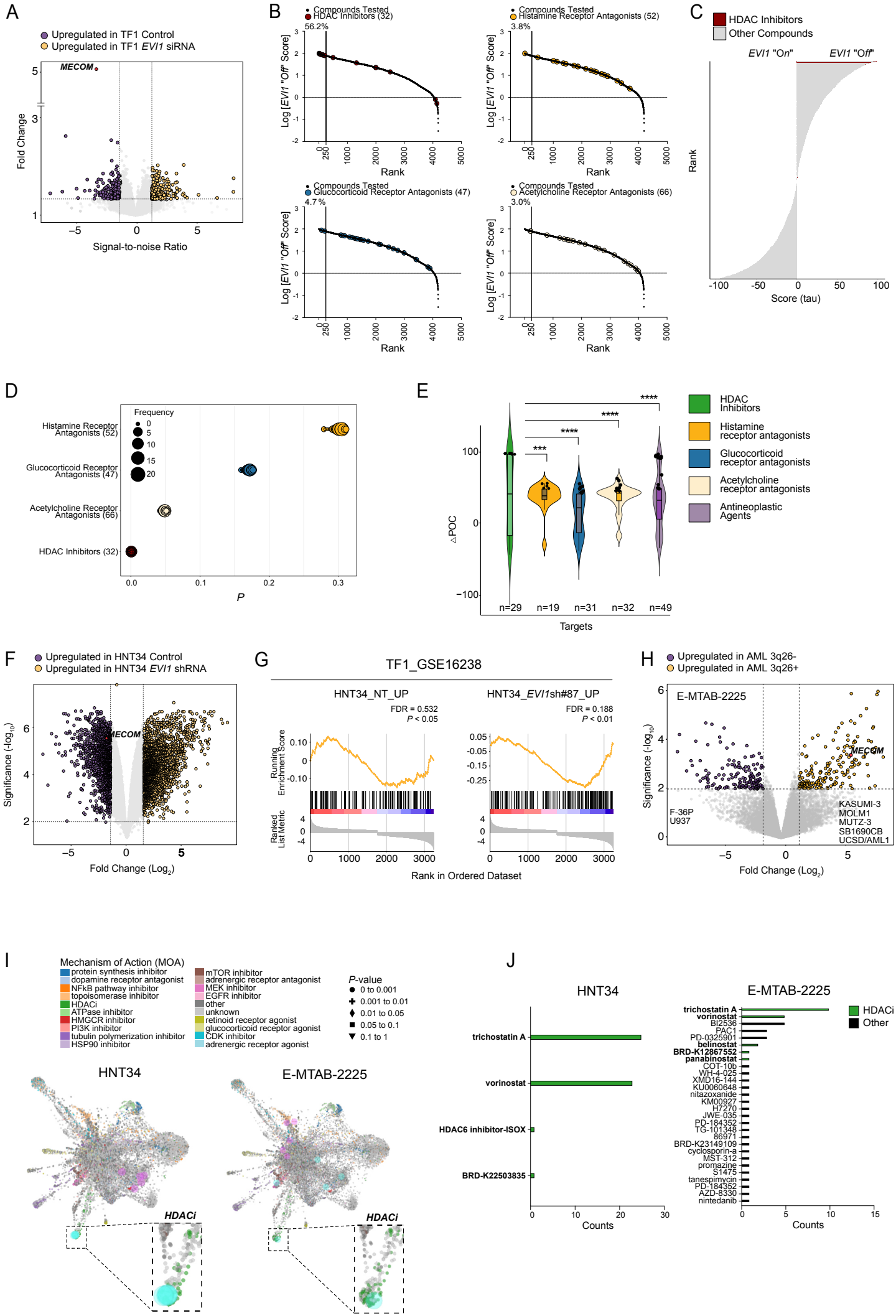
A
Upregulated in TF1 Control
Upregulated in TF1 EVI1 siRNA
MECOM
Fold Change
Signal-to-noise Ratio
B
Compounds Tested
HDAC Inhibitors (32)
56.2%
Histamine Receptor Antagonists (52)
3.8%
Glucocorticoid Receptor Antagonists (47)
4.7%
Acetylcholine Receptor Antagonists (66)
3.0%
Log [EVI1 "Off" Score]
Rank
C
HDAC Inhibitors
Other Compounds
EVI1 "On"
EVI1 "Off"
Rank
Score (tau)
D
Frequency
Histamine Receptor Antagonists (52)
Glucocorticoid Receptor Antagonists (47)
Acetylcholine Receptor Antagonists (66)
HDAC Inhibitors (32)
P
E
△POC
n=29
n=19
n=31
n=32
n=49
Targets
HDAC Inhibitors
Histamine receptor antagonists
Glucocorticoid receptor antagonists
Acetylcholine receptor antagonists
Antineoplastic Agents
F
Upregulated in HNT34 Control
Upregulated in HNT34 EVI1 shRNA
MECOM
Significance (-log10)
Fold Change (Log2)
G
TF1_GSE16238
HNT34_NT_UP
FDR = 0.532
P < 0.05
HNT34_EVI1sh#87_UP
FDR = 0.188
P < 0.01
Running Enrichment Score
Ranked List Metric
Rank in Ordered Dataset
H
Upregulated in AML 3q26-
Upregulated in AML 3q26+
E-MTAB-2225
MECOM
F-36P
U937
KASUMI-3
MOLM1
MUTZ-3
SB1690CB
UCSD/AML1
Significance (-log10)
Fold Change (Log2)
I
Mechanism of Action (MOA)
protein synthesis inhibitor
dopamine receptor antagonist
NFkB pathway inhibitor
topoisomerase inhibitor
HDACi
ATPase inhibitor
HMGCR inhibitor
PI3K inhibitor
tubulin polymerization inhibitor
HSP90 inhibitor
mTOR inhibitor
adrenergic receptor antagonist
MEK inhibitor
EGFR inhibitor
other
unknown
retinoid receptor agonist
glucocorticoid receptor agonist
CDK inhibitor
adrenergic receptor agonist
P-value
0 to 0.001
0.001 to 0.01
0.01 to 0.05
0.05 to 0.1
0.1 to 1
HNT34
E-MTAB-2225
HDACi
HDACi
J
HNT34
trichostatin A
vorinostat
HDAC6 inhibitor-ISOX
BRD-K22503835
Counts
E-MTAB-2225
trichostatin A
vorinostat
BI2536
PAC1
PD-0325901
belinostat
BRD-K12867552
panabinostat
COT-10b
WH-4-025
XMD16-144
KU0060648
nitazoxanide
KM00927
H7270
JWE-035
PD-184352
TG-101348
86971
BRD-K23149109
cyclosporin-a
MST-312
promazine
S1475
tanespimycin
PD-184352
AZD-8330
nintedanib
HDACi
Other
Counts

Figure 2

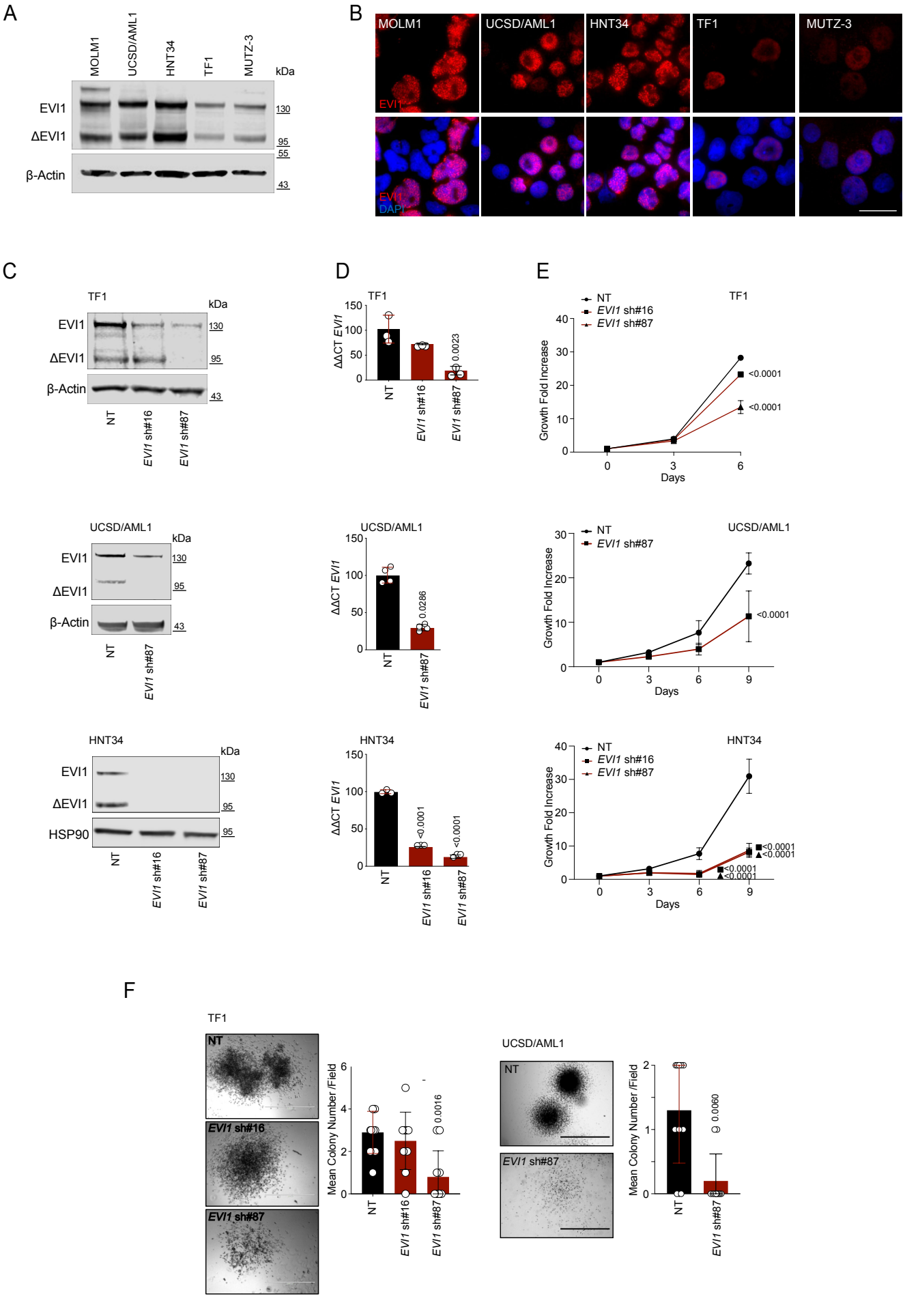
A
MOLM1
UCSD/AML1
HNT34
TF1
MUTZ-3
kDa
EVI1
ΔEVI1
β-Actin
130
95
55
43
B
MOLM1
UCSD/AML1
HNT34
TF1
MUTZ-3
EVI1
EVI1
DAPI
C
TF1
kDa
EVI1
ΔEVI1
β-Actin
130
95
43
NT
EVI1 sh#16
EVI1 sh#87
UCSD/AML1
kDa
EVI1
ΔEVI1
β-Actin
130
95
43
NT
EVI1 sh#87
HNT34
kDa
EVI1
ΔEVI1
HSP90
130
95
95
NT
EVI1 sh#16
EVI1 sh#87
D
TF1
ΔΔCT EVI1
150
100
50
0
0.0023
NT
EVI1 sh#16
EVI1 sh#87
UCSD/AML1
ΔΔCT EVI1
150
100
50
0
0.0286
NT
EVI1 sh#87
HNT34
ΔΔCT EVI1
150
100
50
0
<0.0001
<0.0001
NT
EVI1 sh#16
EVI1 sh#87
E
TF1
NT
EVI1 sh#16
EVI1 sh#87
Growth Fold Increase
40
30
20
10
0
<0.0001
<0.0001
0
3
6
Days
UCSD/AML1
NT
EVI1 sh#87
Growth Fold Increase
30
20
10
0
<0.0001
0
3
6
9
Days
HNT34
NT
EVI1 sh#16
EVI1 sh#87
Growth Fold Increase
40
30
20
10
0
<0.0001
<0.0001
<0.0001
<0.0001
0
3
6
9
Days
F
TF1
NT
EVI1 sh#16
EVI1 sh#87
Mean Colony Number /Field
6
4
2
0
0.0016
NT
EVI1 sh#16
EVI1 sh#87
UCSD/AML1
NT
EVI1 sh#87
Mean Colony Number /Field
2
1
0
0.0060
NT
EVI1 sh#87

Figure 3

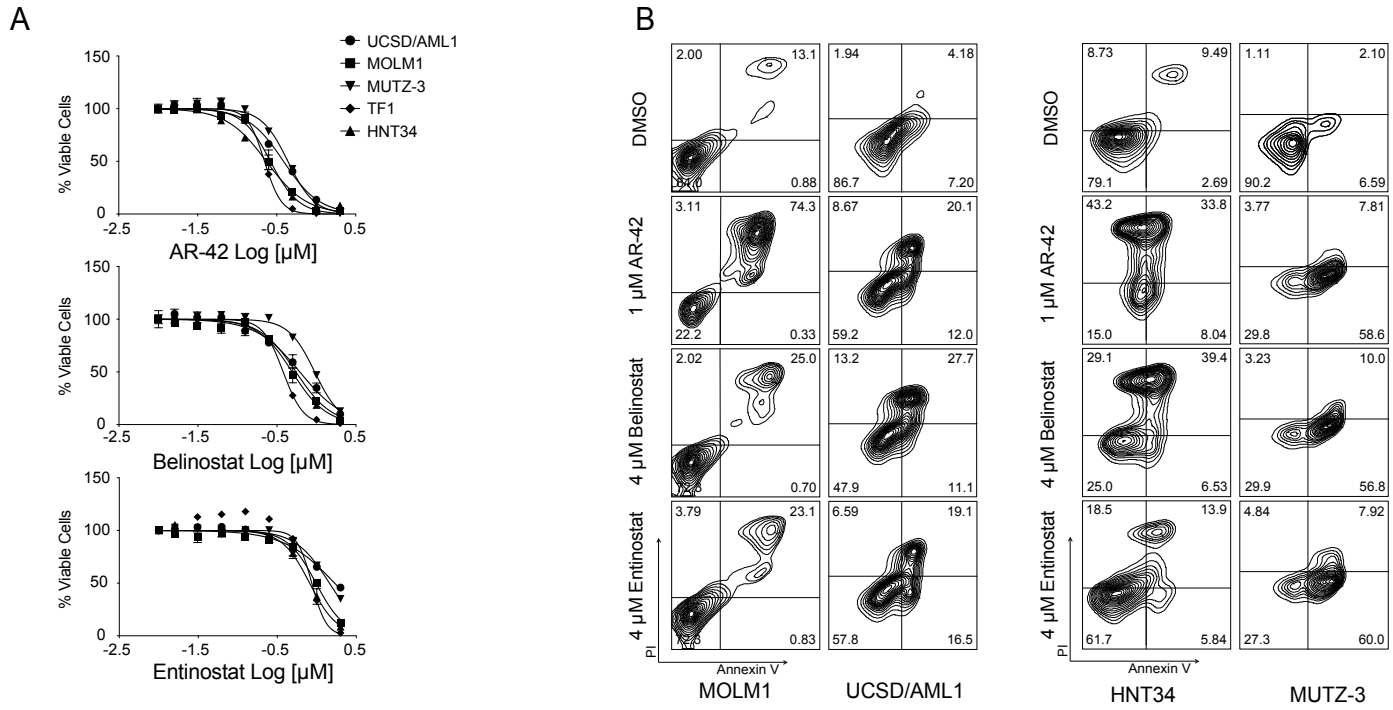
A
UCSD/AML1
MOLM1
MUTZ-3
TF1
HNT34
% Viable Cells
AR-42 Log [μM]
Belinostat Log [μM]
Entinostat Log [μM]
B
DMSO
1 μM AR-42
4 μM Belinostat
4 μM Entinostat
PI
Annexin V
MOLM1
UCSD/AML1
HNT34
MUTZ-3

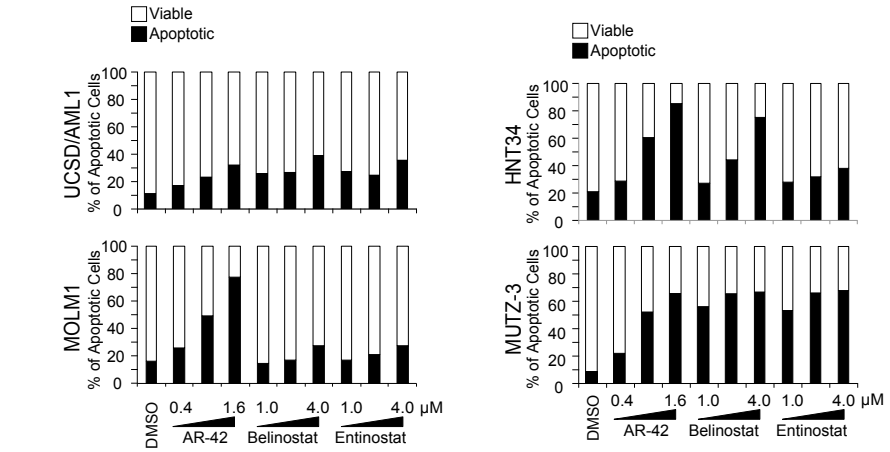
C
Viable
Apoptotic
UCSD/AML1
MOLM1
HNT34
MUTZ-3
% of Apoptotic Cells
DMSO
AR-42
Belinostat
Entinostat
μM

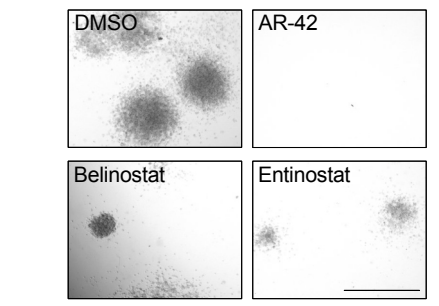
D
DMSO
AR-42
Belinostat
Entinostat

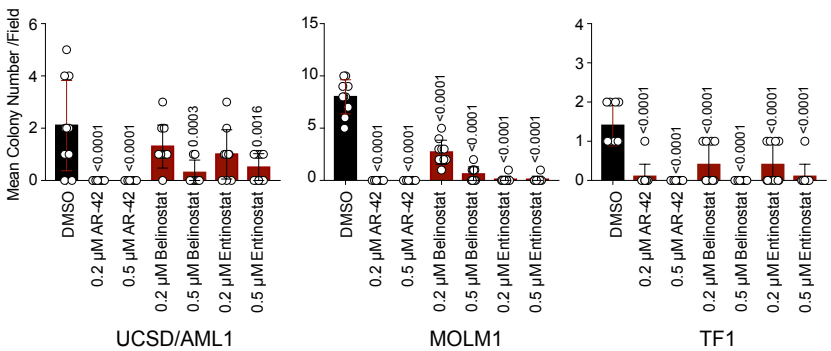
E
Mean Colony Number /Field
UCSD/AML1
MOLM1
TF1

Figure 4

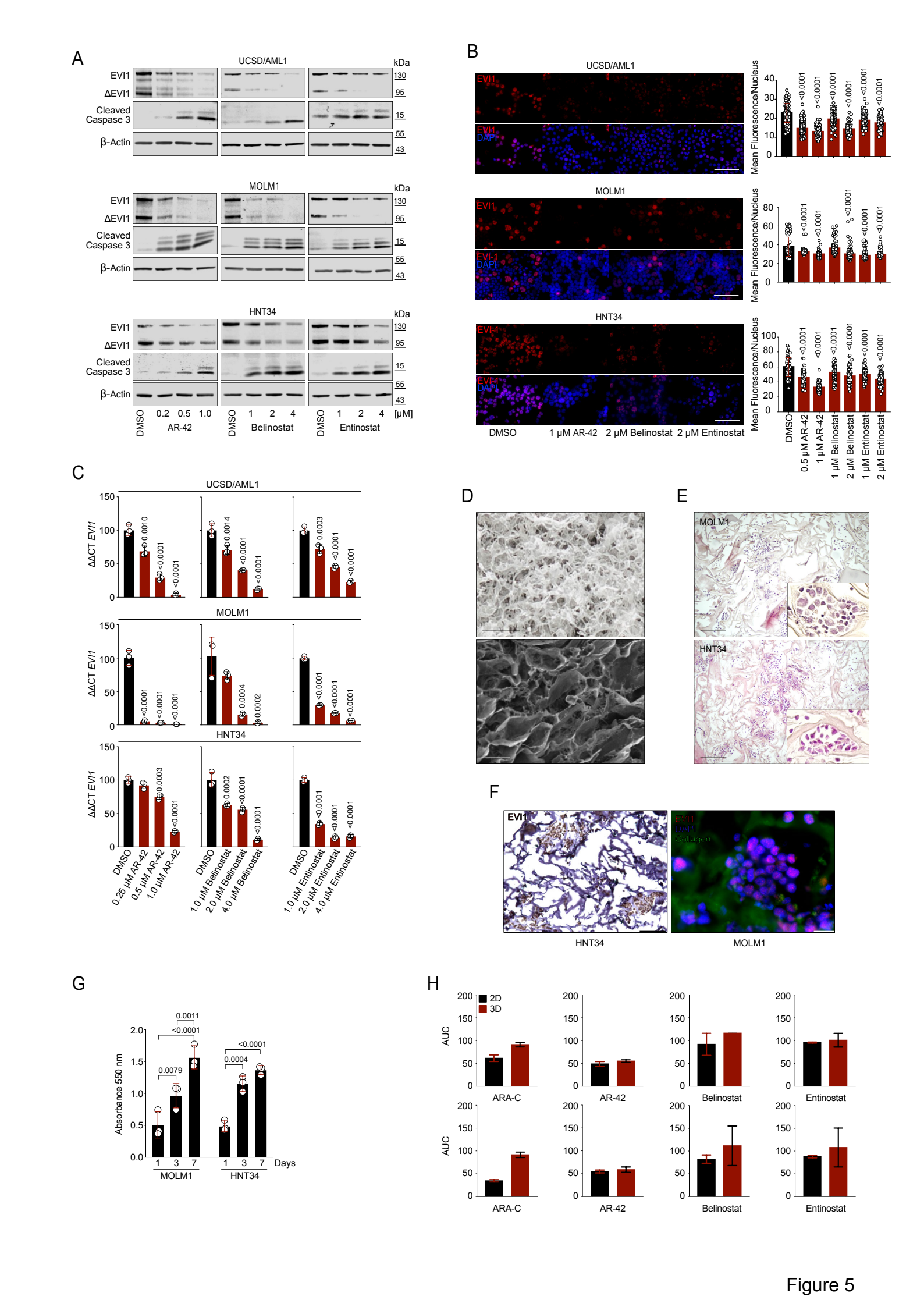
A
UCSD/AML1
MOLM1
HNT34
EVI1
ΔEVI1
Cleaved Caspase 3
β-Actin
kDa
130
95
15
55
43
DMSO
0.2
0.5
1.0
AR-42
1
2
4
Belinostat
Entinostat
[μM]
B
UCSD/AML1
MOLM1
HNT34
EVI1
EVI1 DAPI
Mean Fluorescence/Nucleus
DMSO
1 μM AR-42
2 μM Belinostat
2 μM Entinostat
0.5 μM AR-42
1 μM AR-42
1 μM Belinostat
2 μM Belinostat
1 μM Entinostat
2 μM Entinostat
C
UCSD/AML1
MOLM1
HNT34
ΔΔCT EVI1
0.0010
<0.0001
0.0014
0.0003
0.0004
0.0002
DMSO
0.25 μM AR-42
0.5 μM AR-42
1.0 μM AR-42
1.0 μM Belinostat
2.0 μM Belinostat
4.0 μM Belinostat
1.0 μM Entinostat
2.0 μM Entinostat
4.0 μM Entinostat
D
E
MOLM1
HNT34
F
EVI1
EVI1 DAPI Collagen
HNT34
MOLM1
G
Absorbance 550 nm
0.0011
<0.0001
0.0079
0.0004
Days
MOLM1
HNT34
H
2D
3D
AUC
ARA-C
AR-42
Belinostat
Entinostat

Figure 5

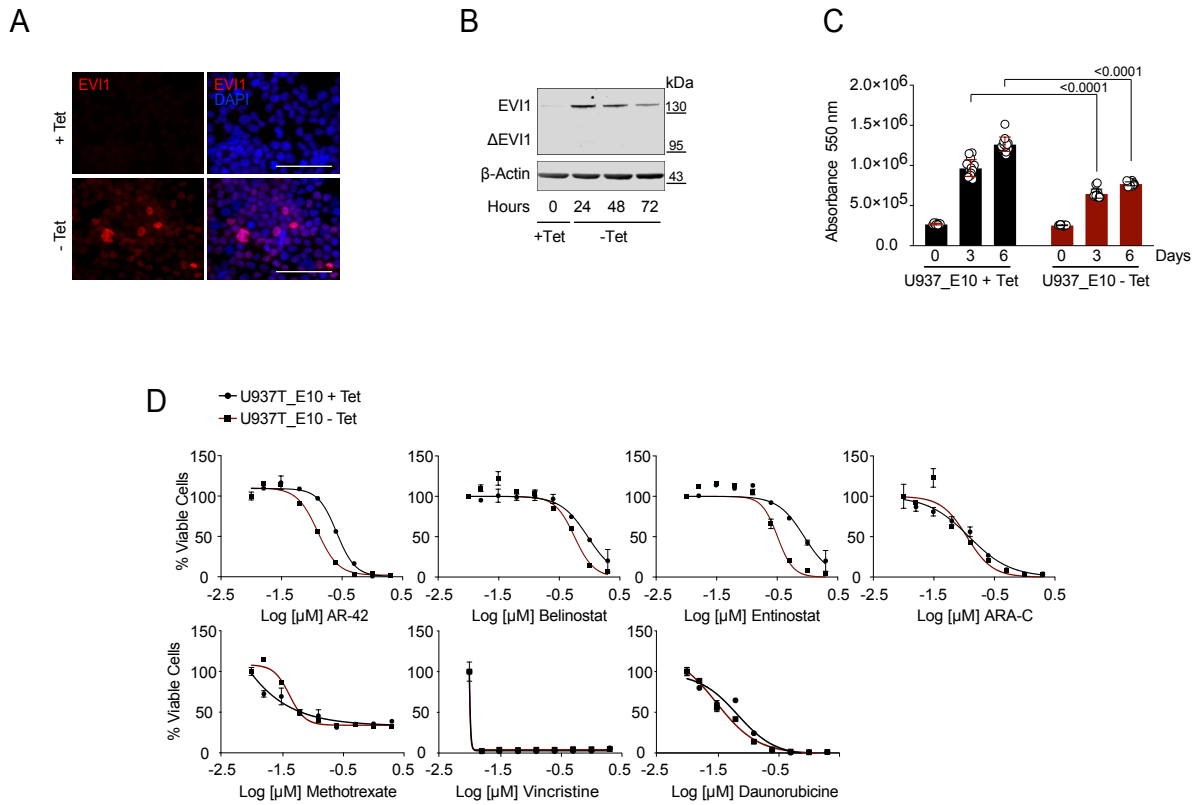
A
EVI1
EVI1 DAPI
+ Tet
- Tet
B
kDa
EVI1
ΔEVI1
β-Actin
130
95
43
Hours 0 24 48 72
+Tet -Tet
C
Absorbance 550 nm
2.0×10^6
1.5×10^6
1.0×10^6
5.0×10^5
0.0
<0.0001
<0.0001
0 3 6 0 3 6 Days
U937_E10 + Tet
U937_E10 - Tet
D
U937T_E10 + Tet
U937T_E10 - Tet
% Viable Cells
Log [μM] AR-42
Log [μM] Belinostat
Log [μM] Entinostat
Log [μM] ARA-C
Log [μM] Methotrexate
Log [μM] Vincristine
Log [μM] Daunorubicine
E
Empty Vector
EVI1 cDNA-ORF
EVI1
EVI1 DAPI
F
HNT34
Empty Vector
EVI1 cDNA-ORF
kDa
EVI1
ΔEVI1
HSP90
130
95
HL-60
G
Empty Vector
EVI1 cDNA-ORF
% Viable Cells
Log [μM] AR-42
Log [μM] Belinostat
Log [μM] Entinostat
Log [μM] ARA-C
H
2F Normal Pattern
EVI1Low
EVI1High
1F2G2O Abnormal Pattern
I
kDa
EVI1
ΔEVI1
HSP90
130
95
95
EVI1Low
EVI1High
J
EVI1Low
EVI1High
Fraction of Cells Alive
0.125 μM AR-42
0.250 μM AR-42
0.125 μM Belinostat
0.250 μM Belinostat
0.5 μM Entinostat
1.0 μM Entinostat
0.032 μM ARA-C
0.125 μM ARA-C
0.063 μM Vincristine
0.125 μM Vincristine
0.016 μM Daunorubicine
0.063 μM Daunorubicine
2.0 μM Methotrexate
4.0 μM Methotrexate
K
EVI1Low
EVI1High
AUC
0.0101
0.0025
0.0480
AR-42
Belinostat
Entinostat
ARA-C
Vincristine
Methotrexate
Daunorubicine

Figure 6

A

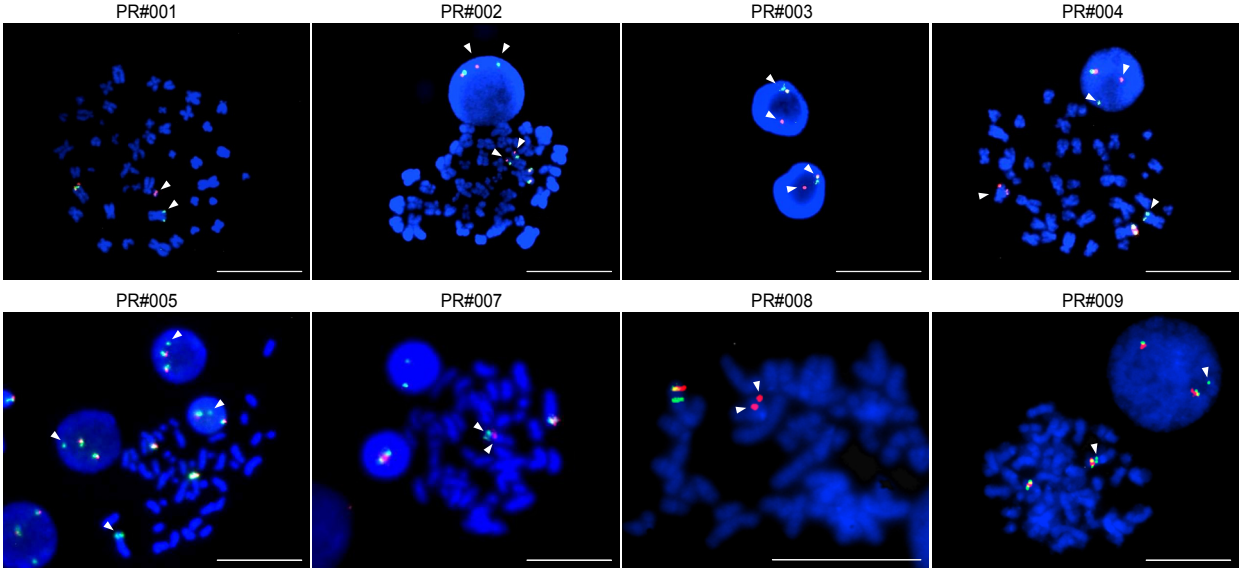
PR#001
PR#002
PR#003
PR#004
PR#005
PR#007
PR#008
PR#009

B

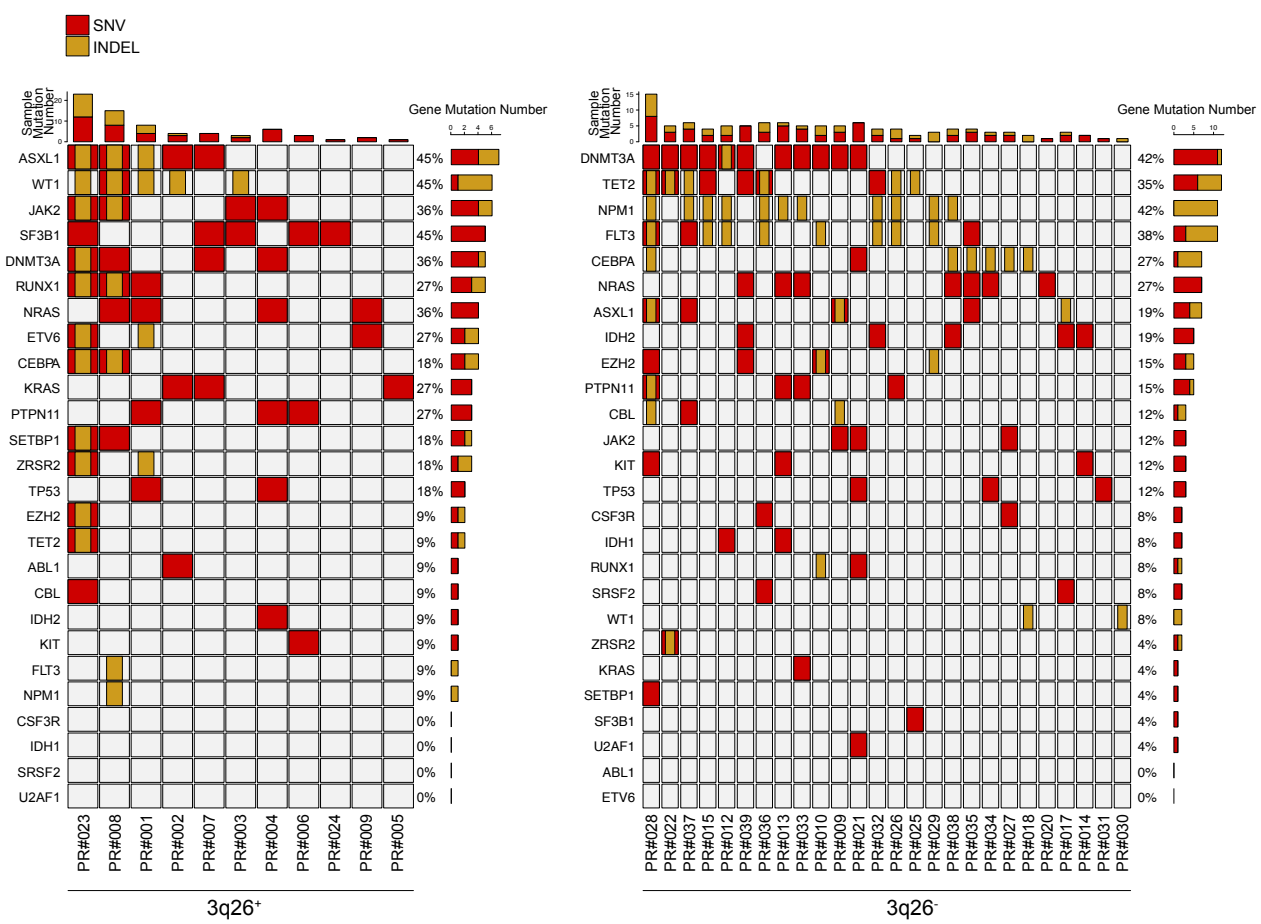
SNV
INDEL
Sample Mutation Number
Gene Mutation Number
ASXL1 45%
WT1 45%
JAK2 36%
SF3B1 45%
DNMT3A 36%
RUNX1 27%
NRAS 36%
ETV6 27%
CEBPA 18%
KRAS 27%
PTPN11 27%
SETBP1 18%
ZRSR2 18%
TP53 18%
EZH2 9%
TET2 9%
ABL1 9%
CBL 9%
IDH2 9%
KIT 9%
FLT3 9%
NPM1 9%
CSF3R 0%
IDH1 0%
SRSF2 0%
U2AF1 0%
PR#023 PR#008 PR#001 PR#002 PR#007 PR#003 PR#004 PR#006 PR#024 PR#009 PR#005
3q26+
DNMT3A 42%
TET2 35%
NPM1 42%
FLT3 38%
CEBPA 27%
NRAS 27%
ASXL1 19%
IDH2 19%
EZH2 15%
PTPN11 15%
CBL 12%
JAK2 12%
KIT 12%
TP53 12%
CSF3R 8%
IDH1 8%
RUNX1 8%
SRSF2 8%
WT1 8%
ZRSR2 4%
KRAS 4%
SETBP1 4%
SF3B1 4%
U2AF1 4%
ABL1 0%
ETV6 0%
PR#028 PR#022 PR#037 PR#015 PR#012 PR#039 PR#036 PR#013 PR#033 PR#010 PR#009 PR#021 PR#032 PR#026 PR#025 PR#029 PR#038 PR#035 PR#034 PR#027 PR#018 PR#020 PR#017 PR#014 PR#031 PR#030
3q26-

Figure 7

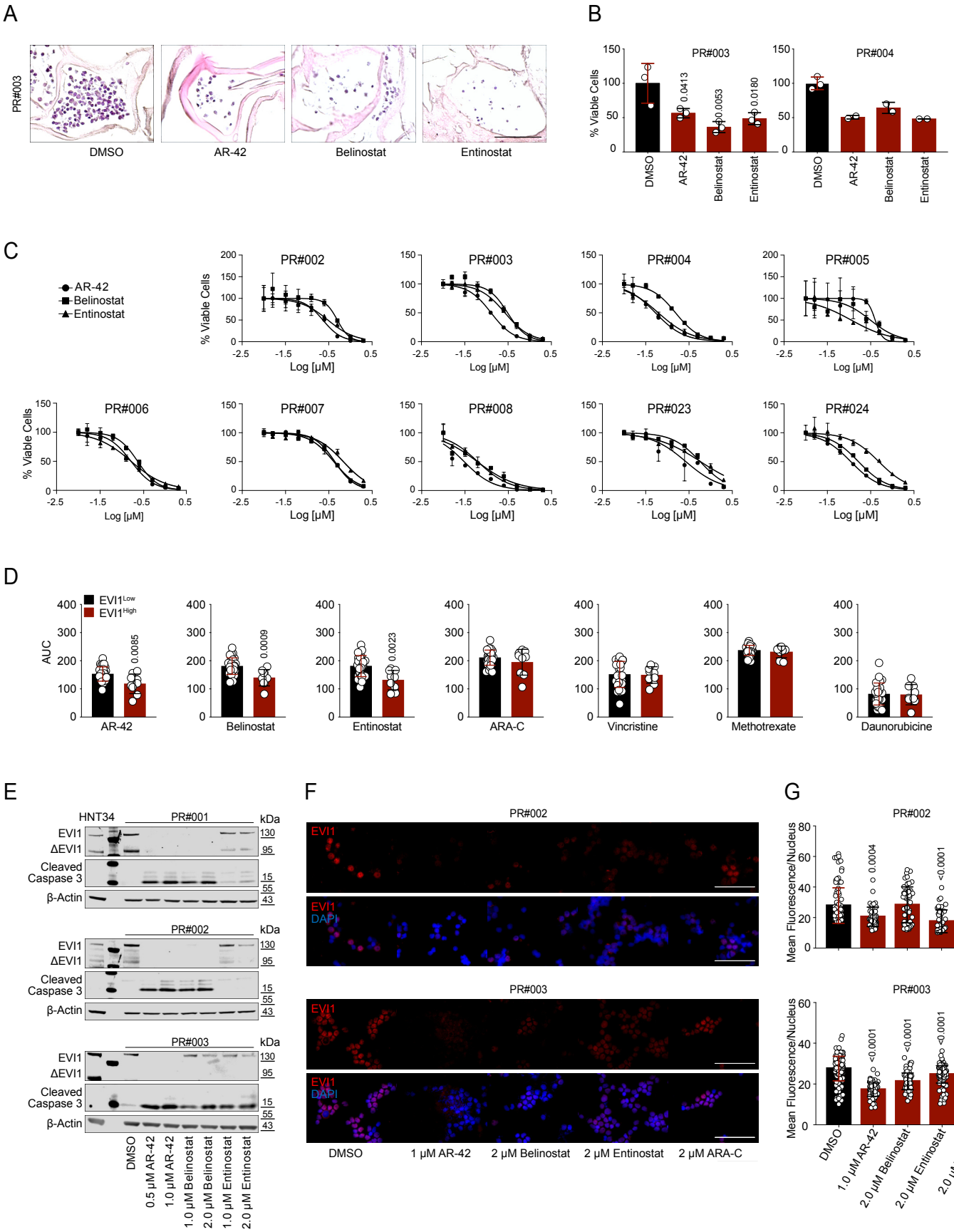
A
PR#003
DMSO
AR-42
Belinostat
Entinostat
B
PR#003
PR#004
% Viable Cells
0.0413
0.0053
0.0180
DMSO
AR-42
Belinostat
Entinostat
C
AR-42
Belinostat
Entinostat
PR#002
PR#003
PR#004
PR#005
PR#006
PR#007
PR#008
PR#023
PR#024
% Viable Cells
Log [μM]
D
EVI1Low
EVI1High
AUC
0.0085
0.0009
0.0023
AR-42
Belinostat
Entinostat
ARA-C
Vincristine
Methotrexate
Daunorubicine
E
HNT34
PR#001
PR#002
PR#003
kDa
EVI1
ΔEVI1
Cleaved Caspase 3
β-Actin
130
95
15
55
43
DMSO
0.5 μM AR-42
1.0 μM AR-42
1.0 μM Belinostat
2.0 μM Belinostat
1.0 μM Entinostat
2.0 μM Entinostat
F
PR#002
PR#003
EVI1
EVI1 DAPI
DMSO
1 μM AR-42
2 μM Belinostat
2 μM Entinostat
2 μM ARA-C
G
PR#002
PR#003
Mean Fluorescence/Nucleus
0.0004
<0.0001
<0.0001
<0.0001
<0.0001
0.0068
DMSO
1.0 μM AR-42
2.0 μM Belinostat
2.0 μM Entinostat
2.0 μM ARA-C
H
HNT34
PR#004
kDa
EVI1
ΔEVI1
Cleaved Caspase 3
β-Actin
130
95
15
11
43
DMSO
0.5 μM AR-42
1.0 μM AR-42
1.0 μM Belinostat
2.0 μM Belinostat
1.0 μM Entinostat
2.0 μM Entinostat
1.0 μM ARA-C
2.0 μM ARA-C

Figure 8

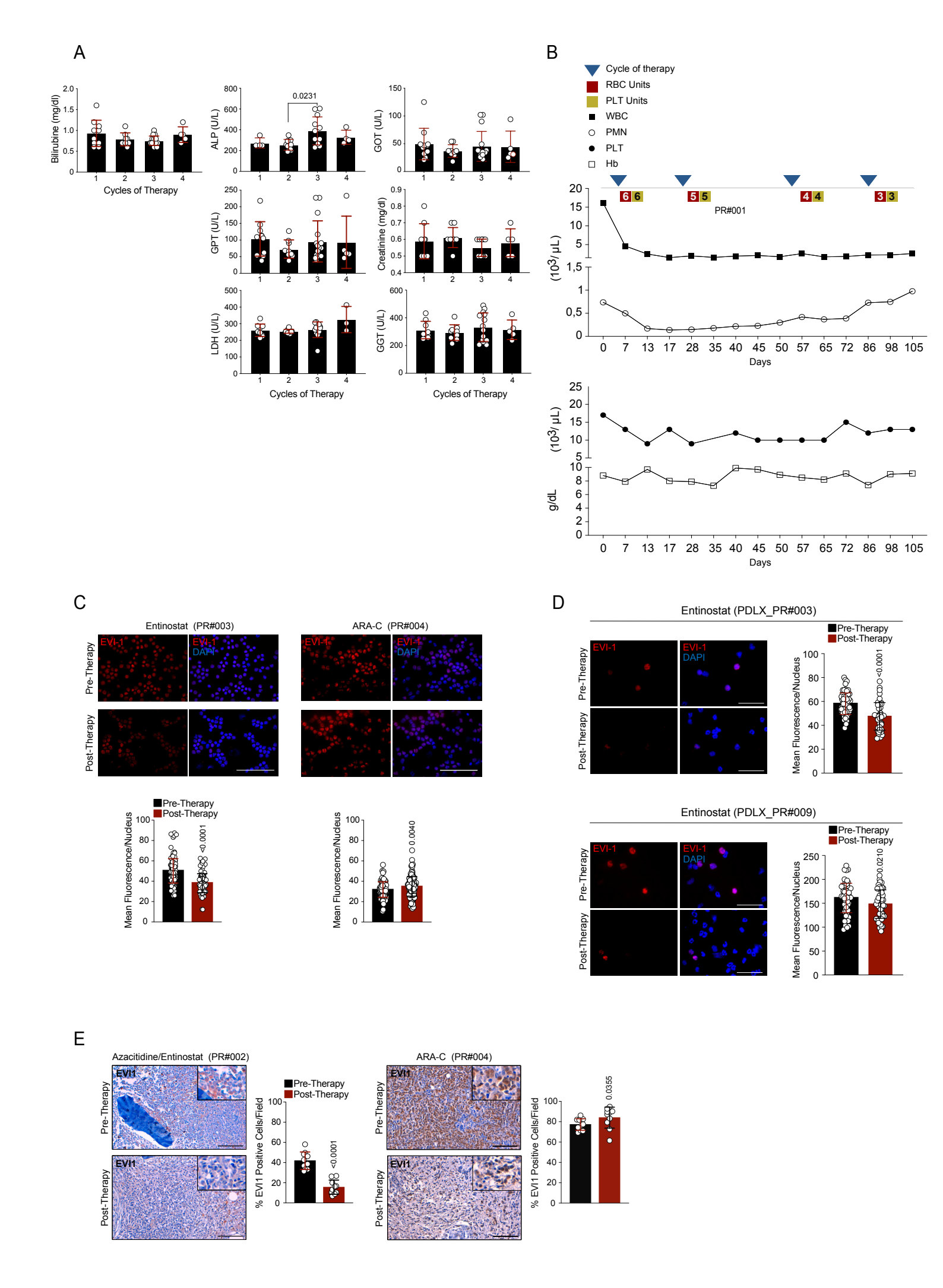
A
Bilirubine (mg/dl)
Cycles of Therapy
ALP (U/L)
0.0231
GOT (U/L)
GPT (U/L)
Creatinine (mg/dl)
LDH (U/L)
GGT (U/L)
Cycles of Therapy
Cycles of Therapy
B
Cycle of therapy
RBC Units
PLT Units
WBC
PMN
PLT
Hb
PR#001
(10³/µL)
Days
g/dL
Days
C
Entinostat (PR#003)
ARA-C (PR#004)
Pre-Therapy
Post-Therapy
EVI-1
EVI-1
DAPI
Pre-Therapy
Post-Therapy
Mean Fluorescence/Nucleus
<0.0001
Mean Fluorescence/Nucleus
0.0040
D
Entinostat (PDLX_PR#003)
Pre-Therapy
Post-Therapy
EVI-1
EVI-1
DAPI
Mean Fluorescence/Nucleus
<0.0001
Entinostat (PDLX_PR#009)
0.0210
E
Azacitidine/Entinostat (PR#002)
ARA-C (PR#004)
EVI1
Pre-Therapy
Post-Therapy
% EVI1 Positive Cells/Field
<0.0001
0.0355

Figure 9

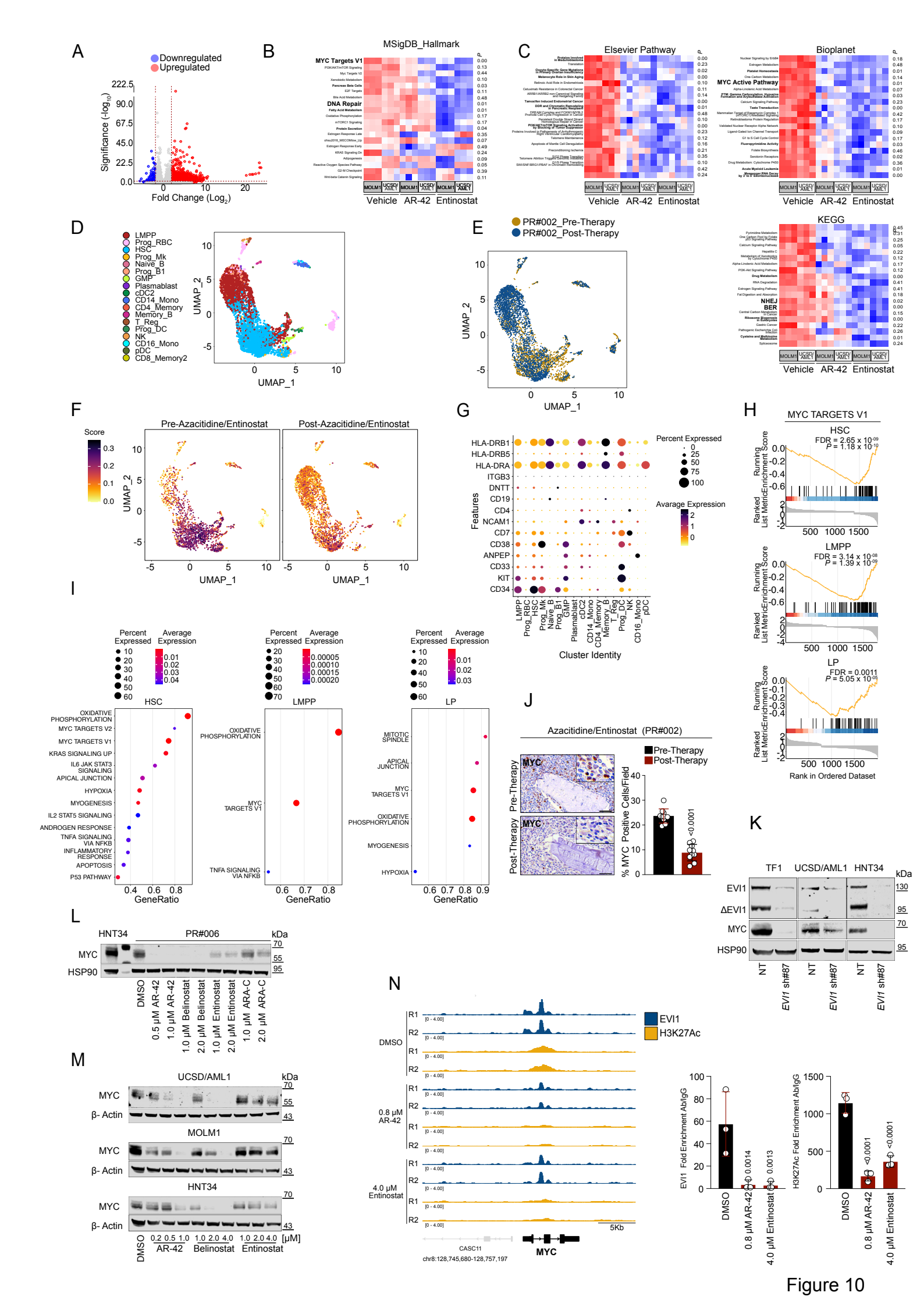
A
Downregulated
Upregulated
Significance (-log10)
Fold Change (Log2)
B
MSigDB_Hallmark
MYC Targets V1
DNA Repair
Vehicle
AR-42
Entinostat
C
Elsevier Pathway
Bioplanet
MYC Active Pathway
D
LMPP
Prog_RBC
HSC
Prog_Mk
Naive_B
Prog_B1
GMP
Plasmablast
cDC2
CD14_Mono
CD4_Memory
Memory_B
T_Reg
Prog_DC
NK
CD16_Mono
pDC
CD8_Memory2
UMAP_1
UMAP_2
E
PR#002_Pre-Therapy
PR#002_Post-Therapy
KEGG
NHEJ
BER
F
Score
Pre-Azacitidine/Entinostat
Post-Azacitidine/Entinostat
G
Percent Expressed
Avarage Expression
Features
Cluster Identity
H
MYC TARGETS V1
HSC
FDR = 2.65 x 10-09
P = 1.18 x 10-10
LMPP
FDR = 3.14 x 10-08
P = 1.39 x 10-09
LP
FDR = 0.0011
P = 5.05 x 10-05
Running Enrichment Score
Ranked List Metric
Rank in Ordered Dataset
I
HSC
LMPP
LP
GeneRatio
J
Azacitidine/Entinostat (PR#002)
Pre-Therapy
Post-Therapy
% MYC Positive Cells/Field
<0.0001
K
TF1
UCSD/AML1
HNT34
EVI1
ΔEVI1
MYC
HSP90
NT
EVI1 sh#87
L
HNT34
PR#006
kDa
DMSO
0.5 μM AR-42
1.0 μM AR-42
1.0 μM Belinostat
2.0 μM Belinostat
1.0 μM Entinostat
2.0 μM Entinostat
1.0 μM ARA-C
2.0 μM ARA-C
M
UCSD/AML1
MOLM1
HNT34
β- Actin
AR-42
Belinostat
Entinostat
[μM]
N
EVI1
H3K27Ac
DMSO
0.8 μM AR-42
4.0 μM Entinostat
5Kb
CASC11
MYC
chr8:128,745,680-128,757,197
EVI1 Fold Enrichment Ab/IgG
H3K27Ac Fold Enrichment Ab/IgG
0.0014
0.0013
<0.0001
<0.0001

Figure 10

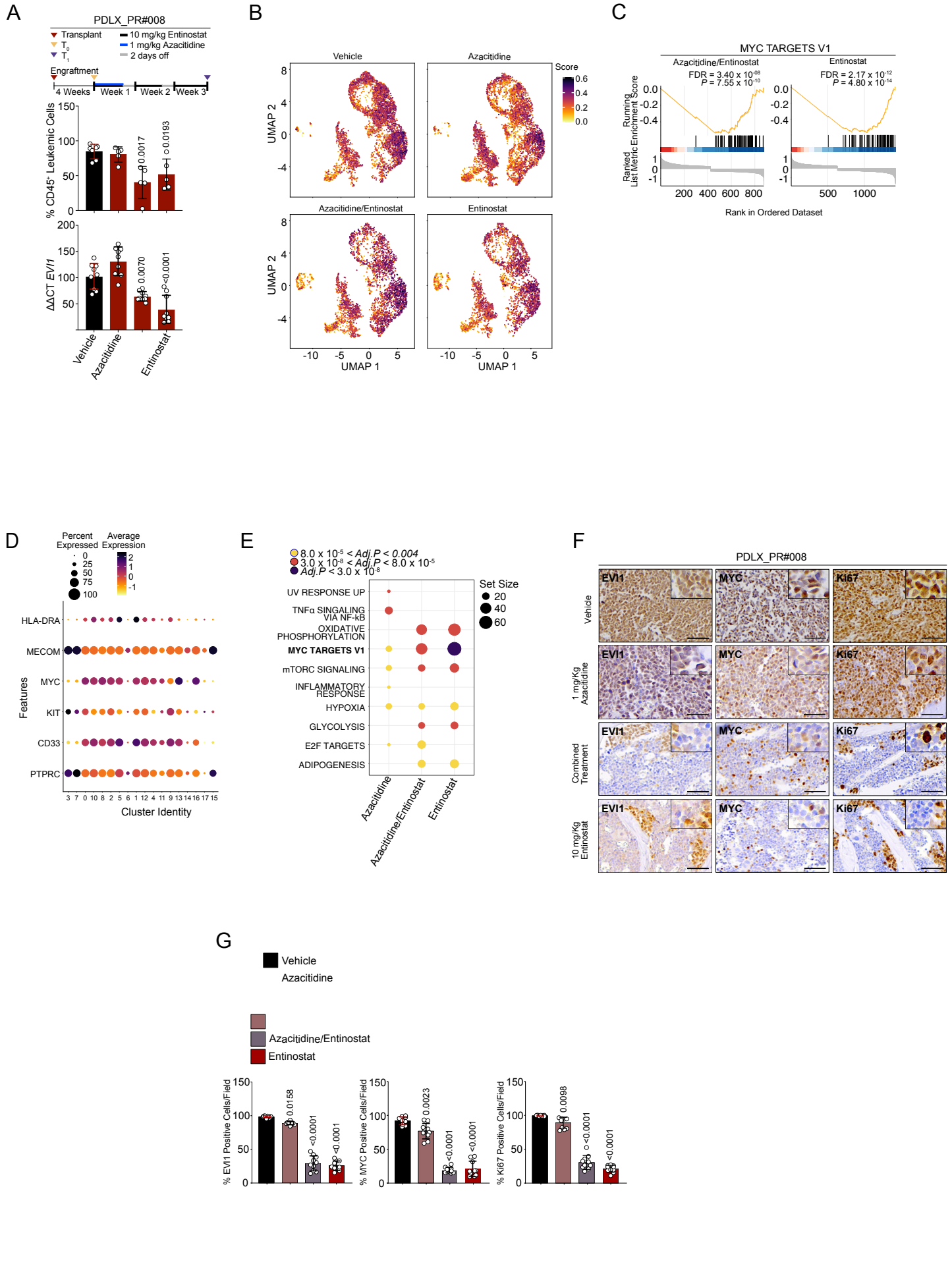
A
PDLX_PR#008
Transplant
T_0
T_1
10 mg/kg Entinostat
1 mg/kg Azacitidine
2 days off
Engraftment
4 Weeks
Week 1
Week 2
Week 3
% CD45+ Leukemic Cells
ΔΔCT EVI1
0.0017
0.0193
0.0070
<0.0001
Vehicle
Azacitidine
Entinostat
B
Vehicle
Azacitidine
Azacitidine/Entinostat
Entinostat
Score
UMAP 1
UMAP 2
C
MYC TARGETS V1
Azacitidine/Entinostat
Entinostat
FDR = 3.40 x 10-08
P = 7.55 x 10-10
FDR = 2.17 x 10-12
P = 4.80 x 10-14
Running Enrichment Score
Ranked List Metric
Rank in Ordered Dataset
D
Percent Expressed
Average Expression
HLA-DRA
MECOM
MYC
KIT
CD33
PTPRC
Features
Cluster Identity
E
8.0 x 10-5 < Adj.P < 0.004
3.0 x 10-8 < Adj.P < 8.0 x 10-5
Adj.P < 3.0 x 10-8
Set Size
UV RESPONSE UP
TNFα SINGALING VIA NF-kB
OXIDATIVE PHOSPHORYLATION
MYC TARGETS V1
mTORC SIGNALING
INFLAMMATORY RESPONSE
HYPOXIA
GLYCOLYSIS
E2F TARGETS
ADIPOGENESIS
Azacitidine
Azacitidine/Entinostat
Entinostat
F
PDLX_PR#008
EVI1
MYC
Ki67
Vehicle
1 mg/Kg Azacitidine
Combined Treatment
10 mg/Kg Entinostat
G
Vehicle
Azacitidine
Azacitidine/Entinostat
Entinostat
% EVI1 Positive Cells/Field
% MYC Positive Cells/Field
% Ki67 Positive Cells/Field
0.0158
<0.0001
<0.0001
0.0023
<0.0001
<0.0001
0.0098
<0.0001
<0.0001

Figure 11

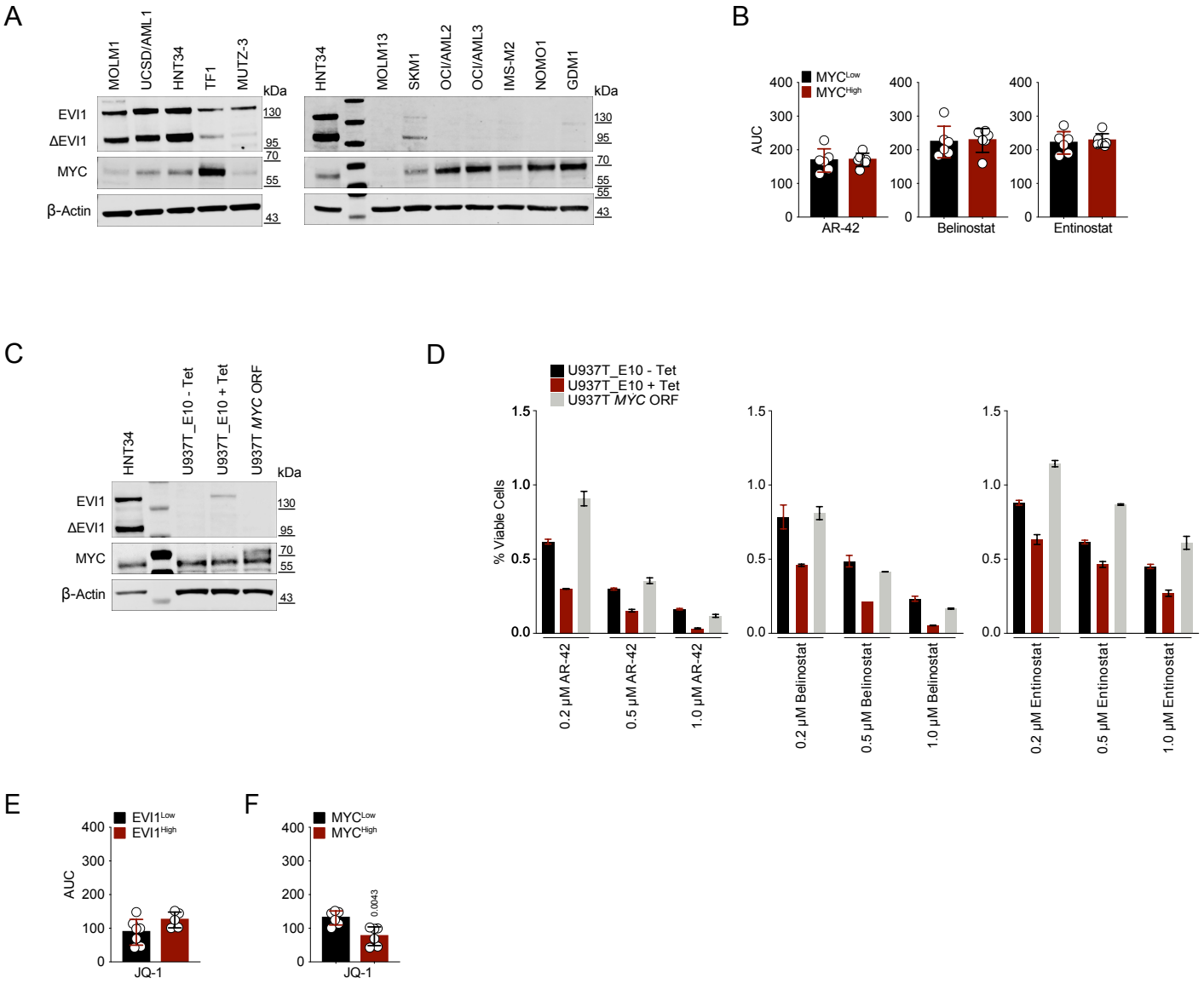
A
MOLM1
UCSD/AML1
HNT34
TF1
MUTZ-3
kDa
EVI1
ΔEVI1
MYC
β-Actin
130
95
70
55
43
HNT34
MOLM13
SKM1
OCI/AML2
OCI/AML3
IMS-M2
NOMO1
GDM1
kDa
130
95
70
55
55
43
B
MYCLow
MYCHigh
AUC
400
300
200
100
0
AR-42
Belinostat
Entinostat
C
HNT34
U937T_E10 - Tet
U937T_E10 + Tet
U937T MYC ORF
kDa
EVI1
ΔEVI1
MYC
β-Actin
130
95
70
55
43
D
U937T_E10 - Tet
U937T_E10 + Tet
U937T MYC ORF
% Viable Cells
1.5
1.0
0.5
0.0
0.2 µM AR-42
0.5 µM AR-42
1.0 µM AR-42
0.2 µM Belinostat
0.5 µM Belinostat
1.0 µM Belinostat
0.2 µM Entinostat
0.5 µM Entinostat
1.0 µM Entinostat
E
EVI1Low
EVI1High
AUC
400
300
200
100
0
JQ-1
F
MYCLow
MYCHigh
0.0043
400
300
200
100
0
JQ-1

Figure 12

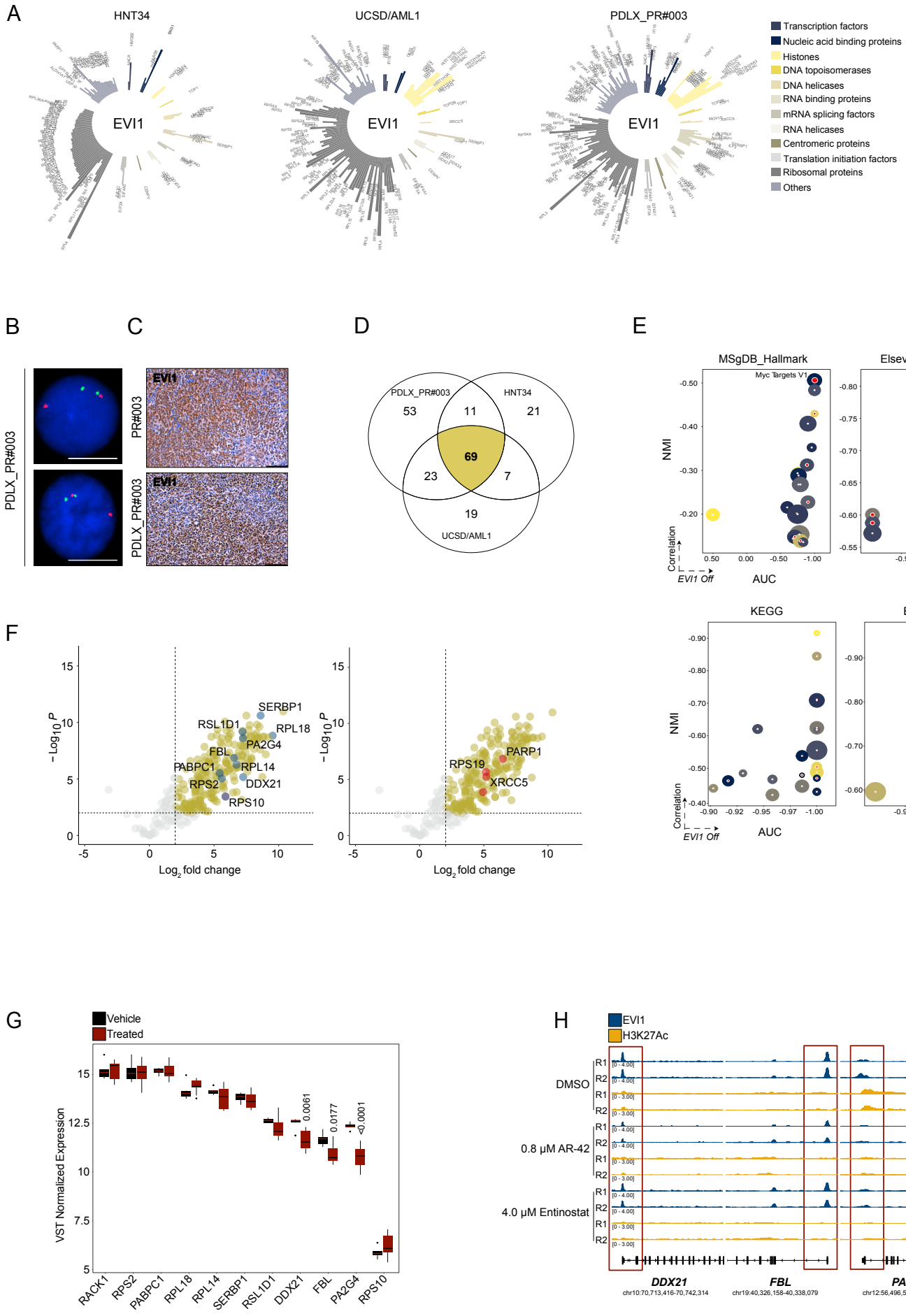
A
HNT34
UCSD/AML1
PDLX_PR#003
EVI1
Transcription factors
Nucleic acid binding proteins
Histones
DNA topoisomerases
DNA helicases
RNA binding proteins
mRNA splicing factors
RNA helicases
Centromeric proteins
Translation initiation factors
Ribosomal proteins
Others
B
PDLX_PR#003
C
PR#003
PDLX_PR#003
EVI1
D
PDLX_PR#003
HNT34
UCSD/AML1
53
11
21
69
23
7
19
E
MSgDB_Hallmark
Elsevier_Pathway
KEGG
Bioplanet
NMI
AUC
Correlation
EVI1 Off
Myc Targets V1
F
SERBP1
RSL1D1
RPL18
PA2G4
FBL
PABPC1
RPL14
RPS2
DDX21
RPS10
PARP1
RPS19
XRCC5
Log2 fold change
G
Vehicle
Treated
VST Normalized Expression
0.0061
0.0177
<0.0001
RACK1
RPS2
PABPC1
RPL18
RPL14
SERBP1
RSL1D1
DDX21
FBL
PA2G4
RPS10
H
EVI1
H3K27Ac
DMSO
0.8 μM AR-42
4.0 μM Entinostat
R1
R2
DDX21
chr10:70,713,416-70,742,314
FBL
chr19:40,326,158-40,338,079
PA2G4
chr12:56,496,538-56,505,889

Figure 13

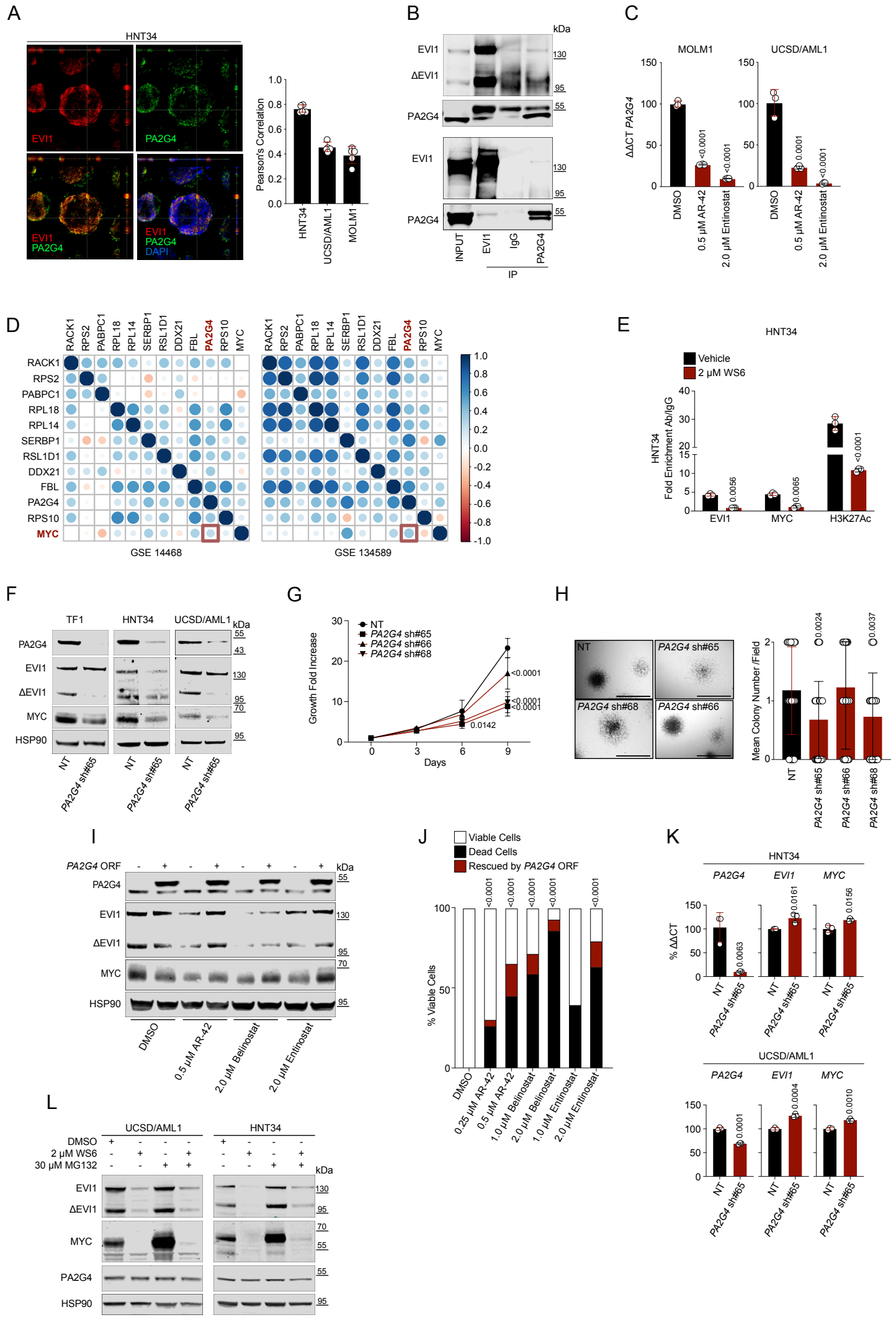
A
HNT34
EVI1
PA2G4
EVI1
PA2G4
EVI1
PA2G4
DAPI
Pearson's Correlation
HNT34
UCSD/AML1
MOLM1
B
kDa
EVI1
ΔEVI1
PA2G4
EVI1
PA2G4
INPUT
EVI1
IgG
PA2G4
IP
C
MOLM1
UCSD/AML1
ΔΔCT PA2G4
DMSO
0.5 μM AR-42
2.0 μM Entinostat
D
RACK1
RPS2
PABPC1
RPL18
RPL14
SERBP1
RSL1D1
DDX21
FBL
PA2G4
RPS10
MYC
GSE 14468
GSE 134589
E
HNT34
Vehicle
2 μM WS6
HNT34
Fold Enrichment Ab/IgG
EVI1
MYC
H3K27Ac
F
TF1
HNT34
UCSD/AML1
kDa
PA2G4
EVI1
ΔEVI1
MYC
HSP90
NT
PA2G4 sh#65
G
NT
PA2G4 sh#65
PA2G4 sh#66
PA2G4 sh#68
Growth Fold Increase
Days
H
NT
PA2G4 sh#65
PA2G4 sh#68
PA2G4 sh#66
Mean Colony Number /Field
I
PA2G4 ORF
kDa
PA2G4
EVI1
ΔEVI1
MYC
HSP90
DMSO
0.5 μM AR-42
2.0 μM Belinostat
2.0 μM Entinostat
J
Viable Cells
Dead Cells
Rescued by PA2G4 ORF
% Viable Cells
DMSO
0.25 μM AR-42
0.5 μM AR-42
1.0 μM Belinostat
2.0 μM Belinostat
1.0 μM Entinostat
2.0 μM Entinostat
K
HNT34
PA2G4
EVI1
MYC
% ΔΔCT
UCSD/AML1
L
UCSD/AML1
HNT34
DMSO
2 μM WS6
30 μM MG132
kDa
EVI1
ΔEVI1
MYC
PA2G4
HSP90

Figure 14

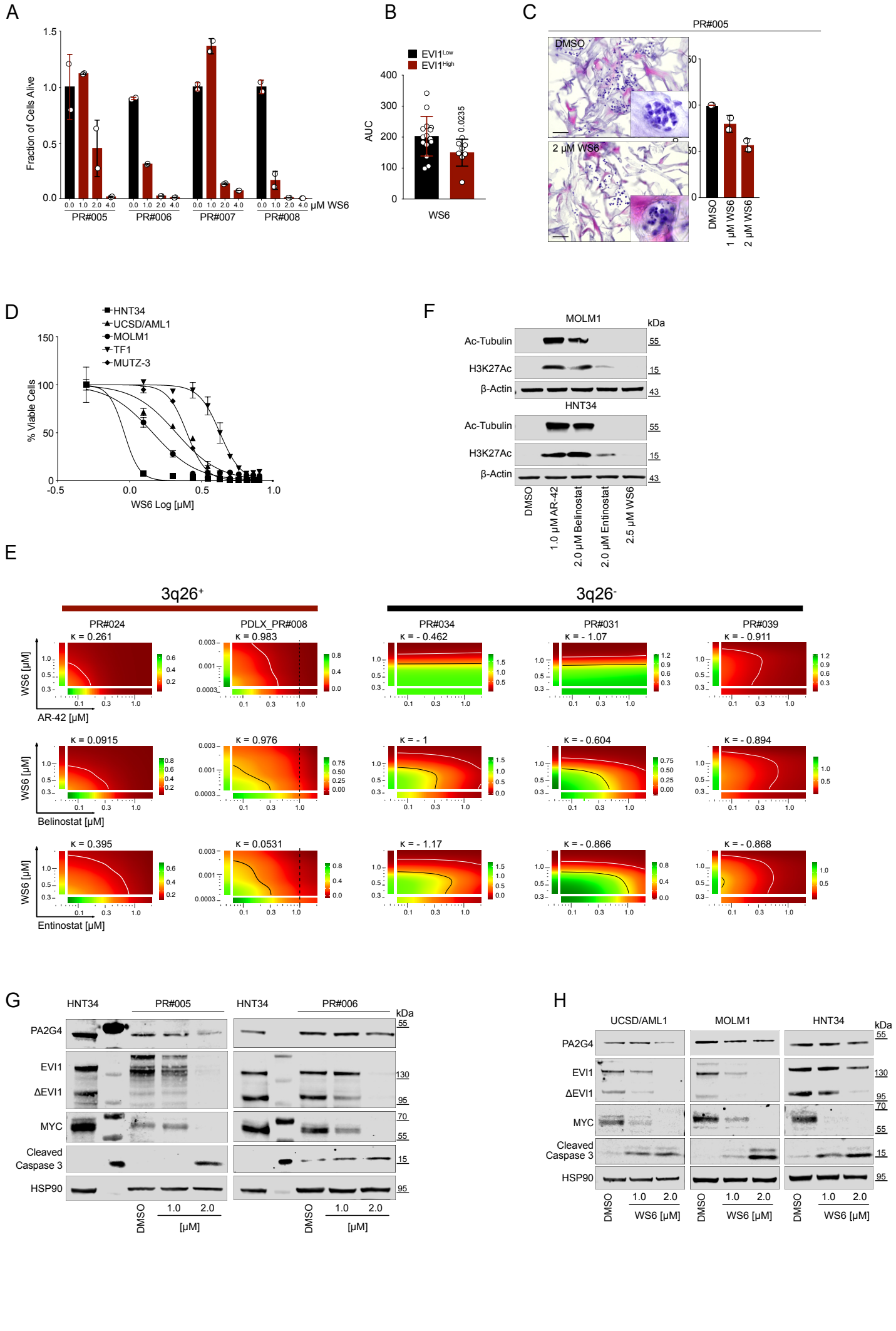
A
Fraction of Cells Alive
PR#005
PR#006
PR#007
PR#008
μM WS6
B
EVI1Low
EVI1High
AUC
0.0235
WS6
C
PR#005
DMSO
2 μM WS6
DMSO
1 μM WS6
2 μM WS6
D
HNT34
UCSD/AML1
MOLM1
TF1
MUTZ-3
% Viable Cells
WS6 Log [μM]
F
MOLM1
kDa
Ac-Tubulin
H3K27Ac
β-Actin
HNT34
DMSO
1.0 μM AR-42
2.0 μM Belinostat
2.0 μM Entinostat
2.5 μM WS6
E
3q26+
3q26-
PR#024
PDLX_PR#008
PR#034
PR#031
PR#039
WS6 [μM]
AR-42 [μM]
Belinostat [μM]
Entinostat [μM]
G
HNT34
PR#005
HNT34
PR#006
kDa
PA2G4
EVI1
ΔEVI1
MYC
Cleaved Caspase 3
HSP90
DMSO
[μM]
H
UCSD/AML1
MOLM1
HNT34
kDa
PA2G4
EVI1
ΔEVI1
MYC
Cleaved Caspase 3
HSP90
DMSO
WS6 [μM]

Figure 15

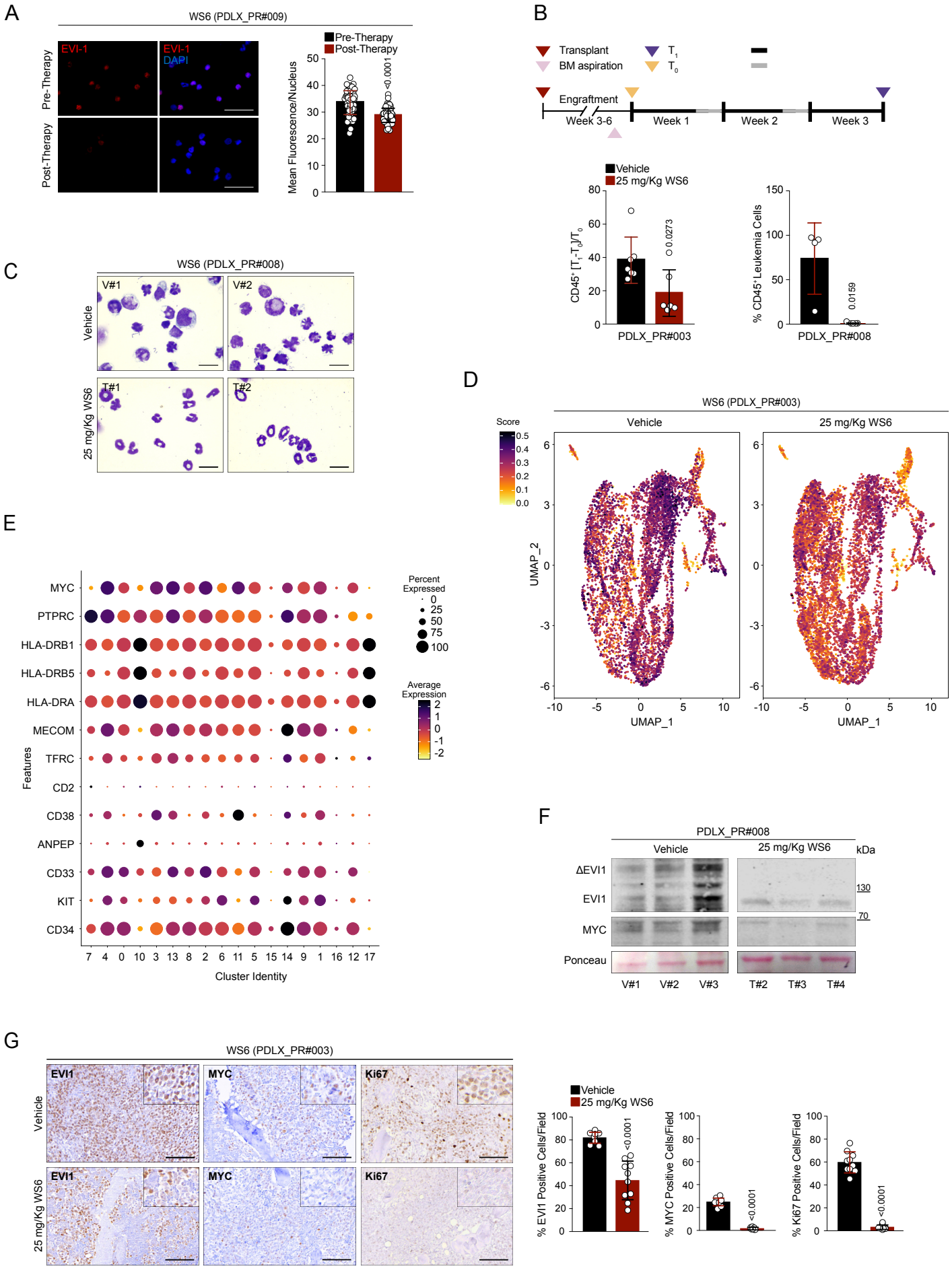
A
WS6 (PDLX_PR#009)
EVI-1
EVI-1
DAPI
Pre-Therapy
Post-Therapy
Pre-Therapy
Post-Therapy
Mean Fluorescence/Nucleus
<0.0001
B
Transplant
BM aspiration
T1
T0
Engraftment
Week 3-6
Week 1
Week 2
Week 3
Vehicle
25 mg/Kg WS6
CD45+ [T1-T0]/T0
0.0273
PDLX_PR#003
% CD45+Leukemia Cells
0.0159
PDLX_PR#008
C
WS6 (PDLX_PR#008)
V#1
V#2
T#1
T#2
Vehicle
25 mg/Kg WS6
D
WS6 (PDLX_PR#003)
Score
Vehicle
25 mg/Kg WS6
UMAP_2
UMAP_1
E
MYC
PTPRC
HLA-DRB1
HLA-DRB5
HLA-DRA
MECOM
TFRC
CD2
CD38
ANPEP
CD33
KIT
CD34
Features
7 4 0 10 3 13 8 2 6 11 5 15 14 9 1 16 12 17
Cluster Identity
Percent Expressed
Average Expression
F
PDLX_PR#008
Vehicle
25 mg/Kg WS6
kDa
ΔEVI1
EVI1
MYC
Ponceau
130
70
V#1 V#2 V#3 T#2 T#3 T#4
G
WS6 (PDLX_PR#003)
EVI1
MYC
Ki67
Vehicle
25 mg/Kg WS6
Vehicle
25 mg/Kg WS6
% EVI1 Positive Cells/Field
<0.0001
% MYC Positive Cells/Field
<0.0001
% Ki67 Positive Cells/Field
<0.0001

Figure 16